Title

Keratin: Structure, mechanical properties, occurrence in biological organisms, and efforts at bioinspiration

Authors

Wang, Bin
Yang, Wen
McKittrick, Joanna
et al.

Publication Date

2016-03-01

DOI

10.1016/j.pmatsci.2015.06.001

Progress in Materials Science 76 (2016) 229–318

Contents lists available at ScienceDirect

Progress in Materials Science

journal homepage: www.elsevier.com/locate/pmatsci

Keratin: Structure, mechanical properties, occurrence in biological organisms, and efforts at bioinspiration

Bin Wang, Wen Yang, Joanna McKittrick, Marc André Meyers *

University of California, San Diego, La Jolla, CA 92093-0418, United States

ARTICLE INFO

Article history:
Received 9 February 2015
Received in revised form 8 May 2015
Accepted 13 May 2015
Available online 4 July 2015

Keywords:
Keratins and keratinous materials
Bioinspiration
Biochemistry
Filament-matrix structure
Mechanical property

ABSTRACT

A ubiquitous biological material, keratin represents a group of insoluble, usually high-sulfur content and filament-forming proteins, constituting the bulk of epidermal appendages such as hair, nails, claws, turtle scutes, horns, whale baleen, beaks, and feathers. These keratinous materials are formed by cells filled with keratin and are considered 'dead tissues'. Nevertheless, they are among the toughest biological materials, serving as a wide variety of interesting functions, e.g. scales to armor body, horns to combat aggressors, hagfish slime as defense against predators, nails and claws to increase prehension, hair and fur to protect against the environment. The vivid inspiring examples can offer useful solutions to design new structural and functional materials.

Keratins can be classified as α- and β-types. Both show a characteristic filament-matrix structure: 7 nm diameter intermediate filaments for α-keratin, and 3 nm diameter filaments for β-keratin. Both are embedded in an amorphous keratin matrix. The molecular unit of intermediate filaments is a coiled-coil heterodimer and that of β-keratin filament is a pleated sheet. The mechanical response of α-keratin has been extensively studied and shows linear Hookean, yield and post-yield regions, and in some cases, a high reversible elastic deformation. Thus, they can be also be considered 'biopolymers'. On the other hand, β-keratin has not been investigated as comprehensively. Keratinous materials are strain-rate sensitive, and the effect of hydration is significant.

Keratinous materials exhibit a complex hierarchical structure: polypeptide chains and filament-matrix structures at the nanoscale,

* Corresponding author.
E-mail address: mameyers@eng.ucsd.edu (M.A. Meyers).

http://dx.doi.org/10.1016/j.pmatsci.2015.06.001

organization of keratinized cells into lamellar, tubular–intertubular, fiber or layered structures at the microscale, and solid, compact sheaths over porous core, sandwich or threads at the macroscale. These produce a wide range of mechanical properties: the Young's modulus ranges from 10 MPa in stratum corneum to about 2.5 GPa in feathers, and the tensile strength varies from 2 MPa in stratum corneum to 530 MPa in dry hagfish slime threads. Therefore, they are able to serve various functions including diffusion barrier, buffering external attack, energy-absorption, impact-resistance, piercing opponents, withstanding repeated stress and aerodynamic forces, and resisting buckling and penetration.

A fascinating part of the new frontier of materials study is the development of bioinspired materials and designs. A comprehensive understanding of the biochemistry, structure and mechanical properties of keratins and keratinous materials is of great importance for keratin-based bioinspired materials and designs. Current bioinspired efforts including the manufacturing of quill-inspired aluminum composites, animal horn-inspired SiC composites, and feather-inspired interlayered composites are presented and novel avenues for research are discussed. The first inroads into molecular-based biomimicry are being currently made, and it is hoped that this approach will yield novel biopolymers through recombinant DNA and self-assembly. We also identify areas of research where knowledge development is still needed to elucidate structures and deformation/failure mechanisms.

Contents

1. Introduction

Nature presents a plethora of unique materials that have evolved for billions of years and have become a continuing source of inspiration for engineers. Biomimetics, the science of imitating nature, is thus an exciting field where the evolutionary refinements are investigated and the biological solutions are applied to develop new materials. The study of biological materials, Biological Materials Science, indispensably paves the way for inventing novel materials by providing principles and mechanisms obtained from natural designs [1–8]. The more traditional approach is being complemented by molecular biomimetics, which shows a bright potential [9].

Many biological materials are composites based on biopolymers and some minerals. This combination yields materials with outstanding properties and functionalities, considering the mainly weak constituents (primarily C, O, N, H, Ca, P and S). Others process nanoscale fibrils with high tensile strength. Wood may have a strength per unit weight comparable to that of the strongest steels; spider silk has a higher specific strength and modulus than steels; shell, bone, and antler have a toughness an order of magnitude greater than their mineral constituents (e.g. calcite, hydroxyapatite) [10]. The secret for achieving this is usually the hierarchically organized structure incorporating biopolymers and minerals.

Keratin represents the most abundant structural proteins in epithelial cells [11], and together with collagen, is the most important biopolymer in animals [12]. According to the Ashby map [13], shown in Fig. 1, keratin is among the toughest biological materials, possessing both high toughness and high modulus, although it is solely composed of polymeric constituents, and seldom contains minerals [14]. Keratinous materials, formed by specifically organized keratinized cells filled with mainly fibrous proteins (keratins), are natural polymeric composites that exhibit a complex hierarchical structure ranging from nanoscale to centimeter scale: polypeptide chain structure, filament-matrix structure, lamellar structure, sandwich structure. They compose the hard integuments of animals, e.g. epidermis, wool, quills, horns of mammals, as well as feathers, claws and beaks of birds and reptiles, and effectively serve a variety of functions, such as for protection and defense, predation and as armor. Therefore, a thorough understanding of the relationships between the units that make up a functional keratinous material would expectantly provide useful knowledge in designing new materials.

Keratinous materials have started to trigger great interest in recent years, and the nascent research area of bioinspiration is gaining increasing attention. However, there have only been very few reports on keratin in terms of biological and structural features, e.g. the classic books including Mercer [15] and Fraser et al. [16] on keratins and Feughelman [17] on α-keratin, and two review papers covering their structure, mechanical properties [12] and phase transition-induced elasticity of α-helical bioe-

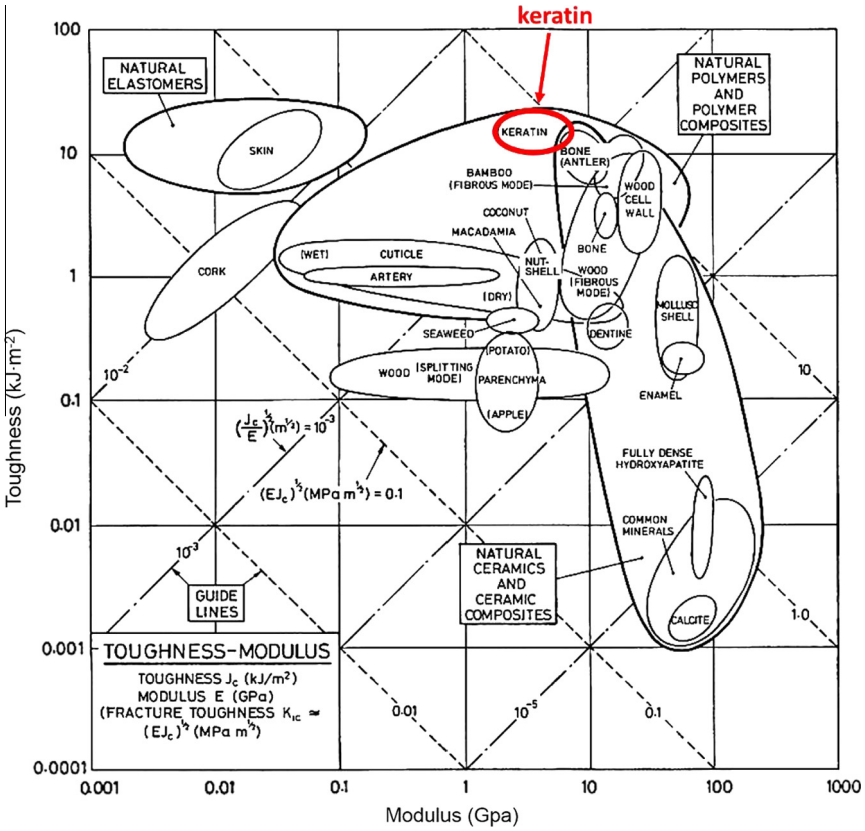

Fig. 1. Materials property chart for biological materials: toughness versus Young's modulus [13].

lastomers [18]. Here, our aim is to provide a present-day comprehensive review of keratins and keratinous materials, incorporating biological and materials science perspectives to illustrate the structural designs and functional properties in order to stimulate the development of novel bioinspired keratin-based designs.

2. Structure, biochemistry and properties of α- and β-keratins

Keratins refer to a group of insoluble and filament-forming proteins produced in certain epithelial cells of vertebrates; they belong to the superfamily of intermediate filament proteins [19], and form the bulk of the horny layer of the epidermis and the epidermal appendages such as hair, nails, horns, and feathers. These keratinous materials, having a high content of cysteine that distinguishes them from other proteins, are typically durable, tough and unreactive to the natural environment; they are assumed to provide mechanical support and diverse protective functions in the adaptation of vertebrates to the external environment [16,20].

2.1. Classification of keratin

Keratins and keratinous materials are often discussed in terms of α- and β-keratins [21]. Based on X-ray diffraction, keratins can be classified into α-pattern, β-pattern, feather-pattern and amorphous pattern [16,22–25]. The feather pattern has been considered as β-pattern since both show the same

characteristic reflections, which has been well-accepted [26]. The amorphous pattern represents the component of the amorphous matrix (detailed in Section 2.2.1) in α-keratinous tissues [27]. Because the ordered structures (α- or β-patterns) dominate the X-ray diffraction, keratinous materials are conveniently distinguished by these ordered components. Additionally, the two regular secondary structures, α-helices and β-sheets, are the two major internal supportive structures in proteins [28]; thus, they are usually used to classify keratins.

Fig. 2 shows the wide-angle X-ray diffraction patterns of these two types of keratins: the α-keratin gives a pattern with an equatorial reflection of spacing 0.98 nm (this corresponds to the distance between α-helical axes) and a meridional reflection of spacing 0.515 nm (relates to the α-helix pitch projection). The β-keratin has a prominent axial repeat of 0.31 nm reflection (the distance between residues along the chain in a β-sheet), the ~0.47 nm equatorial arc (the distance between chains in a β-sheet) and the broad equatorial reflection at 0.97 nm (corresponds to intersheet distance) [16,24,29,30]. α-keratin is found in mammals (there is one mammal, the pangolin, that is reported to have both α and β), and it is the primary constituent of wool, hair, nails, hooves, horns and the stratum corneum (outermost layer of skin). The β-form is the major component of hard avian and reptilian tissues, such as feathers, claws and beaks of birds, and scales and claws of reptiles [31], listed in Table 1. Wool, as a representative α-keratin material, has been extensively studied, as well as feathers as a typical β-keratin material. Wool and feathers will be discussed as representatives of α-keratin and β-keratin, respectively, in Section 2.3.2.

In addition, there are other classifications being used in the literature. In terms of modes of biosynthesis [32] and the amount of sulfur cross links [15], keratins can be classified as soft keratins (e.g. stratum corneum) usually weakly consolidated and with a lower amount of sulfur and lipids, and hard keratins found in hair, nails, claws, beaks, quills, which have a more coherent structure and a higher amount of sulfur [16]. Keratins are also discussed in terms of mammalian keratin, reptilian keratin and avian keratin. Besides, studies on keratinization in vertebrates and the evolution of epidermal proteins have considered keratins as true keratin (α-keratin) and corneous beta-proteins (β-keratins) [33,34].

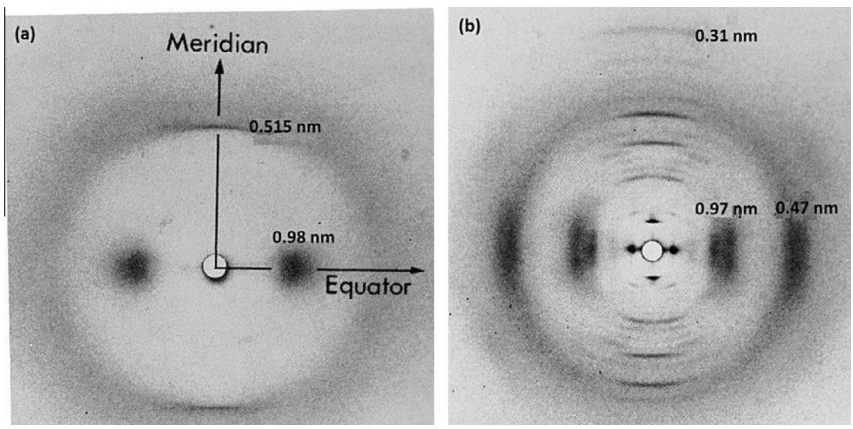

Fig. 2. X-ray diffraction patterns of (a) α-keratin and (b) β-keratin [16].

Table 1
Distribution of α- and β-keratin.

α-Keratin	**Wool**, hair, quills, fingernails, horns, hooves; stratum corneum
β-Keratin	**Feathers**, avian beaks and claws, reptilian claws and scales
α- and β-Keratin	Reptilian epidermis, pangolin scales

2.2. Basic structural characteristics of α- and β-keratins

2.2.1. Filament-matrix structure at nanoscale

Both α- and β-keratinous materials show a fine filament-matrix structure at the nanoscale. Here the 'filament', for α-keratins, denotes the 'intermediate filament (IF)' which represents the structural feature seen by transmission electron microscopy and shows an intermediate size (7–10 nm in diameter) between two other major classes of filamentous structures: microfilaments (actin, 7 nm) and microtubules (24 nm) [35]. For β-keratins, the 'filament' is called 'beta-keratin filament' and has a diameter of 3–4 nm [26,27]. Fig. 3 presents transmission electron micrographs of the filament-matrix structure for typical α-keratinous (IFs in hair, Fig. 3a) and β-keratinous materials (beta-keratin filaments in feather rachis, Fig. 3b). Table 2 compares the major structural characteristics of α- and β-keratins. The filaments are ordered components composed by tightly bonded polypeptide chains and are considered as crystalline portions [29]. The α-keratin IF and the beta-keratin filament show different sizes and generate distinct X-ray diffraction patterns (seen in Fig. 2 and Table 2). In addition, the α-keratin has specialized constituent proteins: several kinds of low-sulfur proteins compose the IFs [36] while the matrix consists of high-sulfur and high-glycine–tyrosine proteins [16]. For β-keratin, there are no different types of proteins [16]; the filament and matrix are incorporated into one single protein [26]. Finally, the molecular mass of α-keratin ranges from 40 to 68 kDa, which is much larger than that of β-keratin, 10–22 kDa [37].

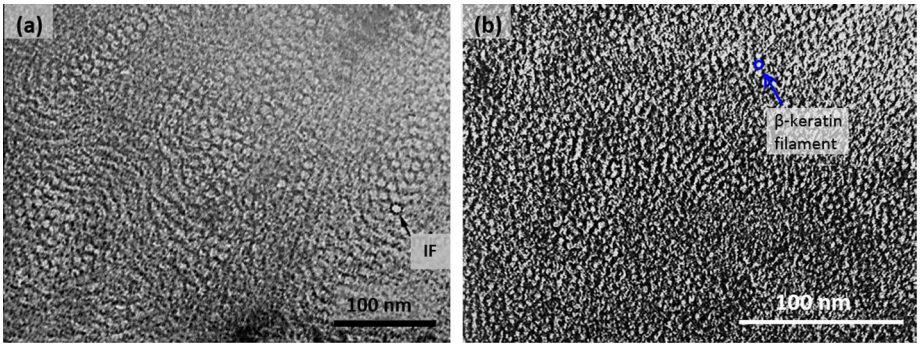

Fig. 3. Transmission electron micrographs of typical keratinous materials with clear filament-matrix structure: (a) cross section of a human hair (α-keratin), stained with osmium tetroxide, showing 7 nm diameter intermediate filaments embedded in a darker matrix; (b) cross section of a seagull feather rachis (β-keratin), stained with potassium permanganate, showing the 3.5 nm diameter β-keratin filaments differentiated by the densely stained matrix [16].

Table 2
Basic structures of α- and β-keratins.

	α-Keratin	β-Keratin
Similarity: structural feature	Filament-matrix structure: IFs and beta-keratin filaments embedded in an amorphous matrix IFs and beta-keratin filaments generate characteristic X-ray diffraction patterns	
Diameters of the filaments (nm)	IFs: ~7	Beta-keratin filaments: 3–4
X-ray diffraction patterns [16,29]	Equatorial reflection with spacing 0.98 nm and a meridional reflection with spacing 0.515 nm	Axial repeat of 0.31 nm reflection and the equatorial reflection ~0.47 nm
Constituting proteins	The IFs consist of several kinds of low-sulfur proteins [36], while the matrix consists of high-sulfur and high-glycine–tyrosine proteins [16]	Do not have two different types of proteins [16]; the filament and matrix are incorporated into one single protein [26]
Characteristic structure	Based on α-helical structure	Based on β-pleated sheet structure
Molecular mass [37]	40–68 kDa	10–22 kDa

2.2.2. Molecular structure and formation of the filaments

The differences of molecular structure and formation of the filaments are the most important features that distinguish α- and β-keratins [28,38–40], shown in Figs. 4 and 5. The α-keratin proteins are organized as coiled coils. The α-helix conformation for the polypeptide chains was first postulated independently by Pauling and Crick [41,42], shortly after Pauling, Corey, and Branson [43] identified the structure as consisting of two helically wound chains of polypeptides. Naturally occurring

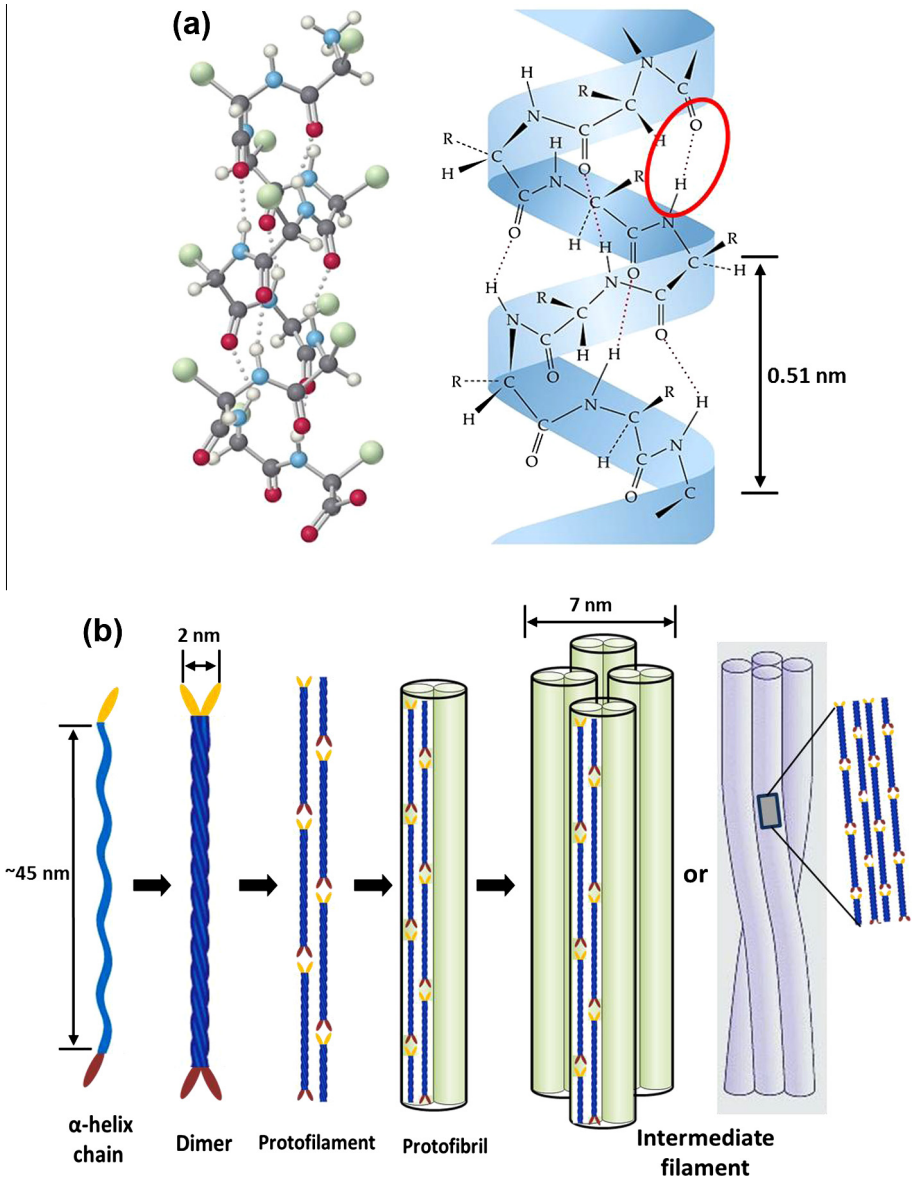

Fig. 4. Intermediate filament structure of α-keratin: (a) ball-and-stick model of the polypeptide chain, and α-helix showing the location of the hydrogen bonds (red ellipse) and the 0.51 nm pitch of the helix [44]; (b) schematic drawing of the intermediate filament formation (reproduced based on [28,45]): α-helix chains twist to form the dimers, which assemble to form the protofilament. Four protofilaments organize into the intermediate filament.

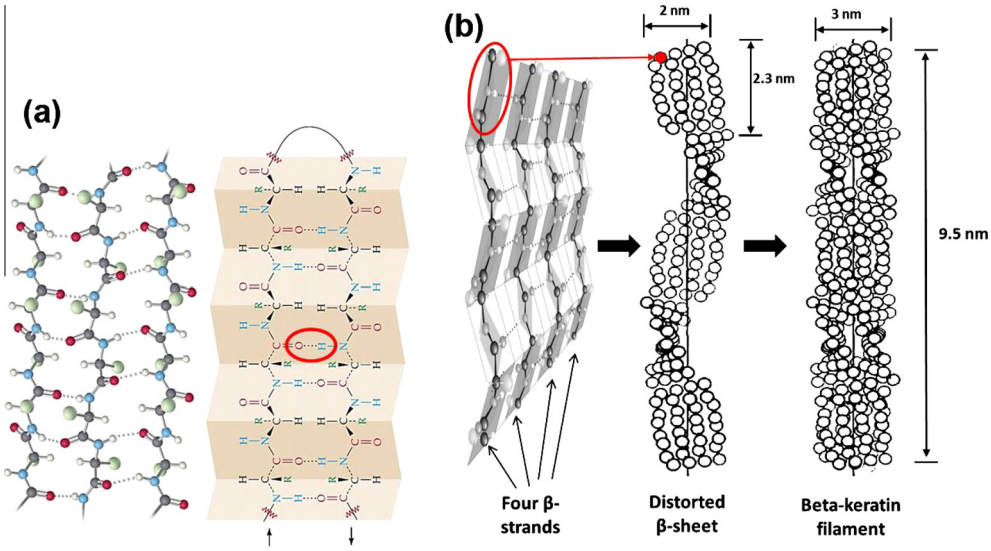

Fig. 5. Structure of the beta-keratin filaments: (a) ball-and-stick model of the polypeptide chain, and illustration of the pleated beta-sheet [44]); (b) schematic drawing of the formation of beta-keratin filament (adapted from [16]): one polypeptide chain folds to form four β-strands which twist to form the distorted β-sheet. Two sheets assemble to form a beta-keratin filament.

α-helices found in proteins are all right-handed. The helical structure is stabilized by the hydrogen bonds (red circled line in Fig. 4a, [44]) inside the helix chain, causing the chain to twist and exhibit a helical shape. Fig. 4b shows the IF formation process [28,45]: two isolated right-handed α-helix chains form a left-handed coiled-coil, the dimer (45 nm long), by disulfide cross links; then dimers aggregate end-to-end and stagger side-by-side via disulfide bonds [46] to form a protofilament (about 2 nm diameter); two protofilaments laterally associate into a protofibril; four protofibrils combine into a circular or helical IF with a diameter of 7 nm. It is clear that the IF is based on coiled-coil structure. Then, the IFs pack into a supercoiled conformation, and link with the matrix proteins. The sulfur-rich amorphous keratin matrix consists of protein chains that have a high amount of cysteine residues or high amounts of glycine, tyrosine and phenylalanine residues [47].

The molecular structure and assembly mechanisms of IF proteins, which α-keratins belong to, can be found in the literature [19]. Although there has not been a high-resolution characterization of keratin IFs, recent studies have reported the crystal structure within the heterodimeric coiled-coil region [48]. Keratins are expected to share structural homology with vimentin, an IF protein, and the crystal structure of vimentin in the literature [49,50] can provide useful information to the understanding of keratin structure. In addition to keratin, fibrin and myosin also form IFs.

For β-keratin, the pleated-sheet (Fig. 5a, [44]) consists of laterally packed β-strands which can be parallel or antiparallel (more stable), and the chains are held together by intermolecular hydrogen bonds (red circled line in Fig. 5a). The pleated sheet structure is stabilized by two factors: the hydrogen bonds between beta strands contribute to forming a sheet and the planarity of the peptide bond forces a β-sheet to be pleated [28]. The formation of beta-keratin filament involves (Fig. 5b): the central region of one polypeptide chain folds to form four lateral beta-strands which then link through hydrogen bonding, resulting in a pleated sheet; then, the sheet distorts to lie in a left-handed helical ruled surface; each residue (marked by red circle in Fig. 5b) is represented by a sphere in the model (red dot in Fig. 5b); two pleated sheets are related by a horizontal diad, superpose and run in opposite directions, forming the filament with a diameter of 4 nm (a pitch length of 9.5 nm and four turns per unit). The terminal parts (not shown in Fig. 5b) of the peptide chains wind around the β-keratin filaments and form the matrix [26]. Therefore, keratins can be considered as a polymer/polymer composite of crystalline filaments embedded in an amorphous matrix.

2.3. Biochemistry of α- and β-keratins

2.3.1. Biochemical and molecular analysis

The systematic protein biochemical analyses of human cells and tissues revealed the diversity of human keratin polypeptides [51–53]; these proteins were separated into type I (acidic) and type II (basic to neutral) keratins. A new consensus nomenclature for mammalian keratin genes and proteins to accommodate functional genes and pseudogenes was developed, and it classifies the 54 functional keratin genes as epithelial and hair keratins (28 type I keratin genes with 17 epithelial and 11 hair keratins, and 26 type II keratin genes with 20 epithelial and 6 hair keratins) [20].

α-keratin can only constitute its filamentous state through the coiled coil assembly and, heteropolymeric pair formation of type I and type II (1:1) protein molecules [19,54]. This gives the name, heterodimer (same as the dimer in Fig. 4b), which is the monomeric unit of the keratin IF (shown in Fig. 6a, [11,38]); it consists of two chains. Each one contains a central alpha-helical rod (about 46 nm in length) with non-helical C- and N-terminal regions [55,56]. The central rod region contains non-helical links at L1, L12, L2 and a stutter. The C- and N-terminal domains are involved in bonding with other IF molecules and matrix.

For β-keratin, the unit molecule of the filaments also consists of three domains: the central domain with residues forming β-sheet and the N- and C-terminal domains (seen in Fig. 6b, the lower schematic) with different lengths and compositions depending on specific keratinous tissues [16,26,57]. The central domain has been the focus in the literature for the molecular structure of β-keratin filament. It is the central part of one polypeptide chain folding several times that forms a pleated sheet structure, the region within two dotted lines shown in Fig. 6b. The other two parts of the chain form the N- and C-terminal domains [26].

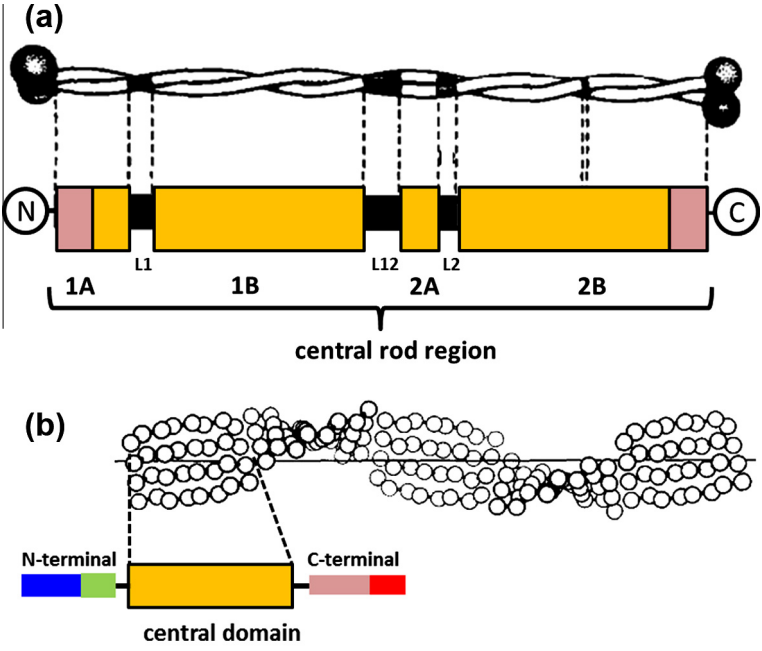

Fig. 6. Detailed structure of: (a) molecular unit of α intermediate filament: the heterodimer. The non-helical N- and C-terminal domains bond with other intermediate filaments and matrix; the central region (about 46 nm in length) has the α-helical coiled coil segments (1A, 1B, 2A, 2B). There are short links (L1, L12 and L2) and a 'stutter' in middle segment (adapted from [11,38]); (b) molecular unit of β-keratin filament: the upper illustrates the distorted sheet and the lower is a schematic representation of a molecule with central domain and N- and C-terminal domains. The central domain (about 34 residues in length) consists of β-forming residues; the N- and C-terminal domains vary among species (adapted from [16,26]).

The molecular units, dimensions and keratin assemblies are summarized in Table 3. For α- and β-keratins, the unit molecules, heterodimer and one distorted pleated sheet, respectively, contain a central domain and two terminal domains. The central helical region of the α-keratin molecular unit contains about 33–35 residues and the non-helical N- and C-terminal domains contain about 136 residues [58]. The length of the central region is about 45 nm [59] and the diameter about 2 nm [35]. For the β-keratin, the length of central region is about 2.3 nm and the diameter about 2 nm [16]. The keratin assembly for α-keratin involves the organization of dimers into IFs, the terminal domains link with other molecules and matrix proteins, and the terminal domains and matrix proteins wind around IFs to form keratin [26,60]. While for β-keratin, the pleated sheets arrange into filaments, C- and N-terminal domains compose the matrix and wind central domain, forming the keratin [26].

2.3.2. Solubility and amino acid compositions

Keratins are naturally insoluble due to intermolecular disulfide linkages [16], intramolecular disulfide linkages [61], and interchain peptide linkages [62,63]. Table 4 lists the purification procedures developed to obtain keratin derivatives. For α-keratinous materials, reduction, oxidation and sulfitolysis methods have been used to generate satisfactory amounts of the derivatives [16,64–67]; while for β-keratinous materials, which have not been as extensively investigated as α-keratin, alkaline thioglycollate and a combination of a disulfide bond-breaking reagent and a protein denaturant were described in literature [68,69]. There are also reports discussing degraded keratins produced by partial hydrolysis (with acid, alkali or enzymes) of wool, hair and feathers. The keratin fragments from hydrolysis are used in the manufacture of cosmetics, artificial leather and filaments [70]. For amino acid analysis, the acid hydrolysis of proteins and automated ion-exchange chromatography are used routinely [71]. The residue percent of wool (representing α-keratin) and feathers (representing β-keratin) are summarized in Table 5 [16,72,73]. It is clear that both show high content of half cystine (cysteine plus half cystine), which provides the disulfide bonds and distinguishes keratin as high-sulfur protein from other biopolymers. Whole wool shows a higher residue percent of half cystine and glutamic acid than whole feather rachis. The higher contents of glycine, proline and serine

Table 3
Comparison of α- and β-keratin: molecular unit (MU), dimension and keratin assembly.

	α-Keratin	β-Keratin
Molecular unit	Dimer	Distorted pleated sheet
Residue number of MU	Helical: 33–35 Non-helical: about 136 [58]	Pleated sheet forming: 34 Non-sheet forming: 59–168 [26,57]
Length of central MU	About 45 nm [59]	2.3 nm [16]
Diameter of MU	Around 2 nm [35]	2 nm [16]
Keratin assembly	Dimers organize into IFs; C-, N-terminal domains link with other molecules and matrix proteins, and these wind around IFs to form keratin [16,60]	Pleated sheets arrange into IFs; C- and N-terminal domains compose matrix, link with other molecules and wind central domain to form keratin [26]

Table 4
Solubility of α- and β-keratin.

α-Keratin	β-Keratin
• Reduction: by potassium thioglycollate in urea to obtain 80–97% keratin from horn, hoof, hair, and further by starch-gel electrophoresis into high-sulfur and low-sulfur fractions [16,64,65]	• Alkaline thioglycollate [68]: by sodium thioglycollate in the absence of oxygen at PH 11 to obtain 80–90% feather keratin [69]
• Oxidation: By treating wool with peracetic acid and dilute alkali [66] Sulfitolysis: By sodium bisulfite with urea and an oxidizing agent [67]	• Combination of a disulfide bond-breaking reagent and a protein denaturant

Table 5
Amino acid composition (residues per 100 residues) of representative α- and β-keratin materials.

Whole wool (representing α-keratin)		Whole feather rachis (representing β-keratin)	
Alanine	5.5	Alanine	8.7
Arginine	6.6	Arginine	3.8
Aspartic acid[a]	6.5	Aspartic acid[a]	5.6
Half cystine[b]	11.4	Half cystine[b]	7.8
Glutamic acid[c]	11.3	Glutamic acid[c]	6.9
Glycine	8.8	Glycine	13.7
Histidine	0.8	Histidine	0.2
Isoleucine	3.4	Isoleucine	3.2
Leucine	7.8	Leucine	8.3
Lysine	3.0	Lysine	0.6
Methionine	0.5	Methionine	0.1
Phenylalanine	2.5	Phenylalanine	3.1
Proline	6.0	Proline	9.8
Serine	9.6	Serine	14.1
Threonine	6.1	Threonine	4.1
Tyrosine	4.1	Tyrosine	1.4
Valine	5.9 [16,72]	Valine	7.8
		Tryptophan	0.7 [69]

[a] Including asparagine.
[b] Content of cysteine plus half cystine in original keratin.
[c] Including glutamine.

in feather rachis may be correlated with the lack of helical secondary structure. Both exhibit very low content of histidine and methionine. It was also reported that the derivatives from reduced wool could be precipitated into high-sulfur and low-sulfur components [16]; while for feather rachis, only minor differences were found between the compositions of the various fractions and no evidence for high- or low-sulfur components was obtained [73].

2.3.3. Biosynthesis of keratins

Present knowledge suggests that differentiation from the germ cells into a particular cell type (here keratinocytes) involves the programmed sequential restriction and activation of different sets of genes; a detailed discussion of the gene-controlling mechanism of gene expression can be found in the literature [74–76].

Keratins are synthesized and regulated by messenger ribonucleic acid (mRNA) inside keratinocytes. A general scheme for the cytodifferentiation of keratinocytes is shown in Fig. 7 [16]. After the cell undergoes a critical mitosis, one or both daughter cells are switched to keratin production. Synthesis of stable keratin mRNA begins, followed by the synthesis of the keratin proteins. As the keratinocyte approaches maturity, the production of RNA and other cellular proteins stops and the nucleus starts degradation. The cell begins keratin stabilization and finally dies, filled with keratin.

It has been suggested [77] that keratin synthesis (red rectangle in Fig. 7) occurs at the surface of the fibrils (bundles of filaments) inside the cell. The newly synthesized proteins from the m-RNA–polysome complex aggregate with the preexisting filaments while still attached to the polyribosome. The polyribosomes are held in close proximity to the fibril until the chain is completed and released. During this period other chains grow on the polyribosome, thus providing further sites of aggregation with the fibril and so the process continues. In addition, there is also post-synthetic chemical modification of keratins, which is keratin stabilization by the formation of disulfide linkages [16].

It is of interest to consider how the newly-synthesized protein chains organize into the final filament-matrix structure. In α-keratinous materials, evidence suggests that the IF is formed by the orderly aggregation of low-sulfur proteins. The high-sulfur proteins forming the matrix do not appear to be important for the formation of IFs, and their synthesis reaches a maximum at a later stage in the maturation of the keratinocyte [15,16]. The syntheses of α- and β-keratins appear to follow different courses, which are related to the different structural organizations. Table 6 compares the differences between keratin syntheses of representative materials. Wool and hair (α-keratin) contain two distinct

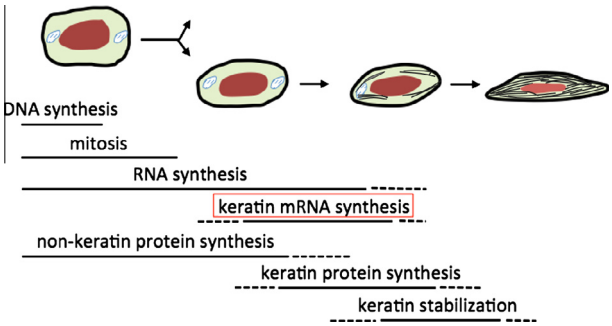

Fig. 7. Schematic illustration of the biosynthesis of keratin. Cells undergo DNA synthesis and mitosis and later RNA synthesis; then synthesis of keratin mRNA and of keratin proteins proceeds. Finally, as cells mature, keratin stabilization begins and cells die filled with keratin [16].

Table 6
Difference between syntheses of α- and β-keratins.

Wool and hair	*Feather*
At earlier stage, IFs (low-sulfur proteins) are synthesized; later as cells approach maturation, matrix proteins (high-sulfur content) are produced between the IFs and further synthesis takes place concurrently; finally the proteins are insolubilized [16,78]	There is no difference in the time course of synthesis of keratin proteins. The major keratins appear to increase in a coordinated fashion [79]; the aggregation mechanism is poorly known [37,80]

types of structural proteins (low-sulfur proteins for IFs and high-sulfur proteins for matrix) and there is a difference in the time course of synthesizing these two components. On the other hand, feathers (β-keratin) involve only one type of protein, and there are no distinct phases in the synthesis of the proteins. The proteins appear to increase in a coordinated fashion, and the detailed mechanism is poorly known [16,37,78–80].

2.3.4. Formation of keratinous materials

Keratinous materials are formed by intracellularly synthesized keratins [81] through epidermal cells which build up at the outermost layer of skin. Keratinization replaces the cytoplasmic content by filamentous proteins, and is part of the cellular differentiation that transforms living and functional cells into cornified, structurally stable dead cells [82,83]. The formation of keratinous materials involving keratin development and ultrastructural changes is illustrated here for stratum corneum in mammalian epidermis (representing α-keratin) and feathers (representing β-keratin). The reptilian epidermis is quite distinct, and the keratinization of turtle shell epidermis is also discussed.

The mammalian epidermis consists of four distinguishable layers of cells (shown in Fig. 8a and b): stratum basale, stratum spinosum, stratum granulosum and stratum corneum. Cells in the first three layers are differentiating keratinocytes while the outermost stratum corneum is composed of dead keratin-filled corneocytes [81]. The stratum basale is about one cell thick and rests on the basement membrane (BM in Fig. 8c), which separates the basal layer from the dermis and follows the contours of the finger-like process of the epidermal cells (seen in Fig. 8a and c). Fig. 8b shows a micrograph and schematic of the epidermal cells illustrating the keratin development and structural changes [81]. In the stratum basale, cells begin to proliferate and the cytoplasm of cells contains fine filaments (F in Fig. 8c), which measure about 5 nm in diameter and are of indeterminate length. These filaments frequently occur in bundles or fibrils [16]. Cells move outward and differentiate. In the stratum spinosum, keratin synthesis proceeds at a high rate. The cells are star-shape and there is a dramatic increase in the cytoplasmic content of fibrils [84], which were reported to be 7–8 nm in diameter [85]. The stratum granulosum layer indicates the border between differentiation and cornification

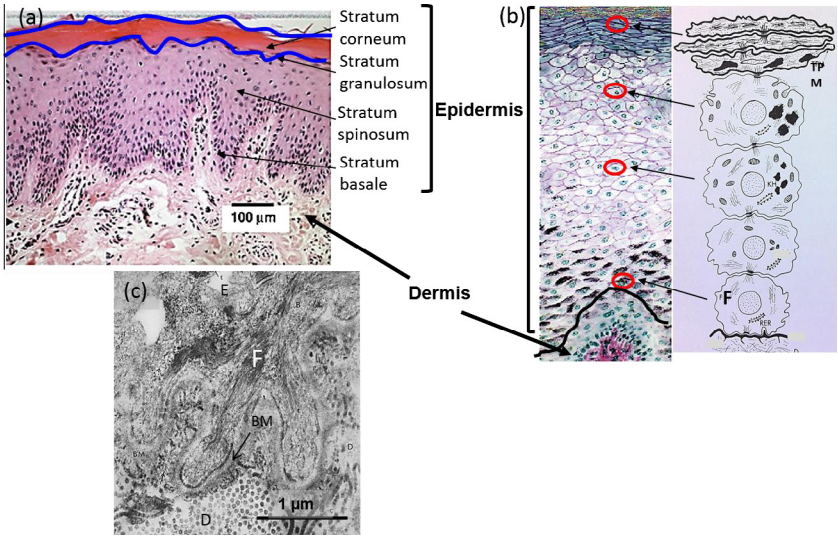

Fig. 8. (a) Diagram of cross section of stained bovine skin that shows the epidermal layers [81]. (b) Micrograph of a bovine hoof [81] and a schematic diagram of the epidermal cells showing the structural changes during keratinization. Bundles of filaments (F) have developed in the cytoplasm of basal cells. In stratum granulosum, aggregated keratohyalin granules are visible. In the last stage, the plasma membranes thicken (TPM) and the major cytoplasmic components disappear except for the fibrils [87]; (c) transmission electron micrograph of the border between the basal layer of the epidermal cells (E) and the dermis (D) that shows the basement membrane (BM) and the filaments as bundles (F) in the cytoplasm of basal cells [84].

processes, in which cells have undergone a change in shape so that their dimensions parallel to the skin surface are much greater than those in the direction of growth. The salient feature is the appearance and accumulation in the cytoplasm of keratohyalin granules (a protein structure involved in keratinization). It was reported that at high magnification, filaments (filaments of the final keratin in the stratum corneum) are observed to pass through keratohyalin granules [84,85]. As the cells proceed outward to the stratum corneum, an abrupt transition takes place involving complete filling of the cytoplasm with keratin and the removal of the nucleus, the keratohyalin granules and all of the cytoplasmic organelles [16]. The cells are flattened and dense with filament-amorphous matrix structure (the matrix was reported to be derived from keratohyalin [86], finalizing the keratinization process [16,87].

For the formation of feathers, it has been reported [88] that the events occurring along the time line include: (i) the initiation of a pin feather (the developing feather rising from epidermis, Fig. 9a), (ii) elongation of the pin feather, (iii) production, differentiation, and maturation of cells comprising calamus, rachis, barbs and barbules (feather components shown in Fig. 9), and (iv) regression of dermal core (proliferating part at the basal of feather) during final calamus maturation. Fig. 9a–c illustrates the developing process from a pinfeather to a down feather [89,90]. In the germinal layer (Germinal Collar in Fig. 9b) of the follicle, mitotic activity produces densely-packed, polygonal immature feather keratinocytes that contribute to a pin feather visible above skin. The pin feather of an embryonic chick shows longitudinal barb ridges (Fig. 9b) that consist of several kinds of cells that later develop into separated barbs with opposite branching barbules (forming the vanes). The continuing production of keratinocytes pushes previously formed differentiating and mature tissues to move outward. The sheath (formed by outermost epidermal cells encasing the growing feather), feather and dermal tissues are generated proximally. Along with the feather growing, the sheath and feather tissues differentiate, mature, die, and dehydrate as they move distally. Once a feather reaches length appropriate for a specific body location and/or species, proximal cell proliferation diminishes drastically, and the epidermal tissues no longer move distally but remain stationary and mature in situ. During these periods, different kinds of cells undergo the keratinization process in different time courses [16,90].

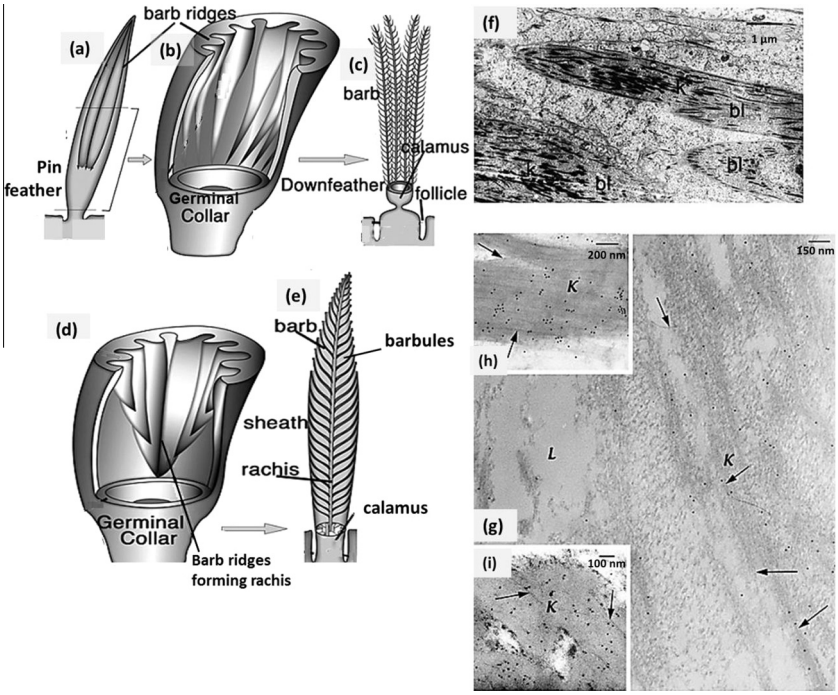

Fig. 9. Schematic illustrating the development from an immature feather (pin feather) to an adult feather with electron micrographs showing the keratin development. (a) A pin filament from an embryonic chick with longitudinal barb ridges that are at the earliest stages of the barbs and barbules; (b) separated barb ridges originating from the germinal collar; (c) barbs with barbules formed from barb ridges attached to the calamus; (d) a new germ is formed at the germinal collar (the base of calamus) for the second generation of the feather. At this time, the barb ridges develop into barbs and merge to form the rachis; (e) a feather showing the calamus, rachis and vanes (formed by barbs and barbules), and the follicle in the skin where the calamus resides; (f) elongated barbule cells (bl) in the chick after 13 days incubation. Keratin bundles (k) are assembled into long filaments [89]; (g) keratin bundles (K) among the cytoplasm and lipid material (L) of a differentiating cell of chick wing feathers. Arrows indicate 10 nm thick filaments; (h) detail of large keratin bundles (arrows point to 10 nm dense filaments); (i) mature cell showing filaments (arrows) among the electron-pale and amorphous matrix. [90].

Fig. 9d and e shows the regeneration of feather (developing feather during molt): at the base of the calamus (germinal collar) a new germ is formed for the second generation of feather; the barb ridges develop into barbs and merge to form rachis, and gradually a pennaceous feather grow from the follicle with calamus, rachis and barbs.

It has been reported that keratin fibrils about 3 nm in diameter appear in the cytoplasm and extend the length of the barb ridge cell from 13-day chick embryo [91]. Fig. 9f shows long and parallel keratin bundles (kl) in elongated barbule cells (bl) in the chick at about 13 days incubation [89]. As the embryo ages, the size of the filament bundles increases. Finally, the fibrils cease growing, coalesce and dehydrate while other cytoplasmic organelles are resorbed from the cell [16]. The cytoplasmic keratin bundles (K) and lipid material (L) from a differentiating cell in chick wing feather cortex are shown in Fig. 9g. Fig. 9j and k shows the detailed view of the keratin bundles and filament-matrix structure in a mature cell [90].

It is interesting to note that during the formation of feathers which are exclusively made of (β-) keratins [92,93], studies [94,95] indicated the presence of α-keratins in developing feather [96,97]: a small amount of α-keratins of intermediate filament type forms the early keratin clumps in barb and barbule cells. These initial nuclei are rapidly coated/degraded and replaced by large amounts of feather keratins, which turn the keratin bundles into corneous materials where no signs of α-intermediate filaments are seen [93].

The formation of hard epidermis on the carapace (dorsal shell) and plastron (ventral shell) of turtle embryos and juvenile turtles has been studied [98,99]. Fig. 10 schematically illustrates the epidermis development during this process interpreting the transition from α- to β-keratins, which takes place in the embryonic stage. Keratin development begins with differentiation of cells in the peridermis (a superficial layer of early developing epidermis) and the basal layer in middle embryonic stage, followed by the formation of embryonic epidermis consisting of 3–6 cell layers. In advanced embryos, the lower two layers of embryonic epidermis start depositing α-keratin bundles forming the α-layer. This precedes the formation of the β-layers from the basal epidermis of the shell. As α-layer and compact β-layer form toward the end of the embryonic stage, a splitting zone is formed beneath the α-layer. During hatching the embryonic epidermis including the α-layer sheds with only the β-layer remaining. The morphologies of developing keratinized layers during the formation of the shell is shown in Fig. 11 [98]. At a later embryonic stage, the epidermis layer (e in Fig. 65a) forms, beneath which β-keratin cells are developing (arrowheads in Fig. 11a). At the end of embryonic stage, the carapace shows a thick β-layer under both the embryonic epidermis layers and the darker α-layer; while the plastron (Fig. 11c) shows the layered structure (from outside to inside): embryonic layers (e), α-layer (arrow), β-layer (k), differentiating β-cells (arrowheads), and basal layer (b). The carapace shows the large-scale synthesis of β-keratin in the β-layer and the start of shedding of embryonic layer at the end of embryonic stage.

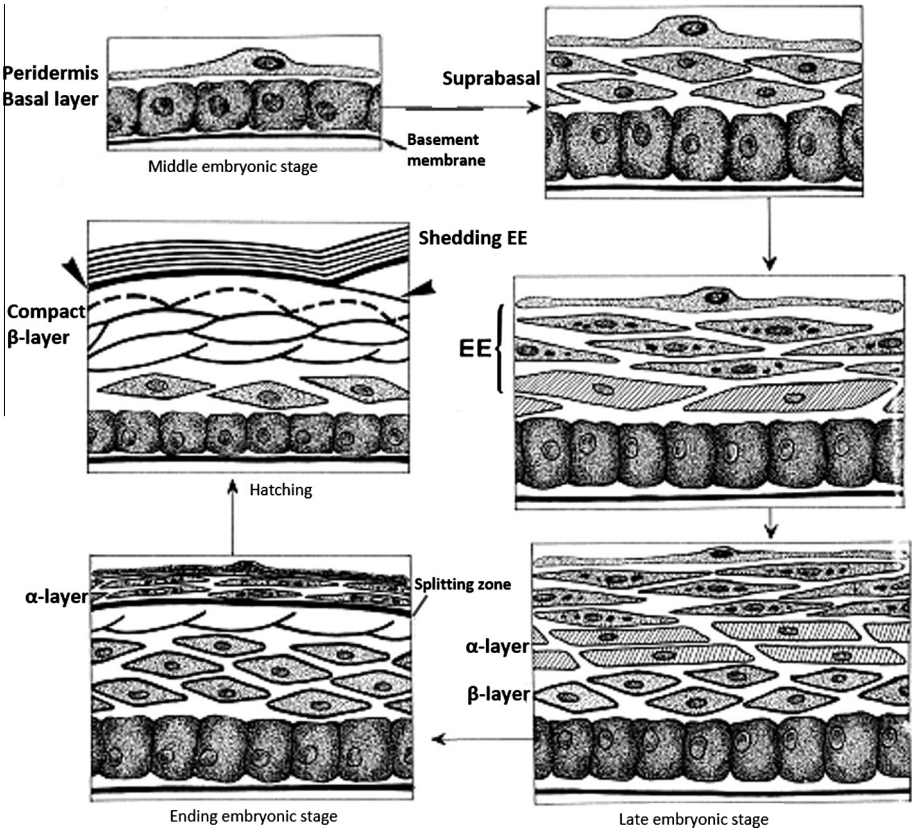

Fig. 10. Schematic of the keratinization process in the shell epidermis of embryonic turtle: in middle embryonic stage, peridermis and basal layer present and later suprabasal layer appears; in advanced embryos, embryonic epidermis (EE) forms which will disappear during hatching; in late embryonic stage, α-keratin layer forms from embryonic epidermis, and later β-keratin layer begins to form under α-layer; at the end of embryonic stage, α-keratin layer and compact β-keratinized layer form; during hatching, the embryonic epidermis sheds on β-keratinized layer. Arrowheads indicate the shedding line [98].

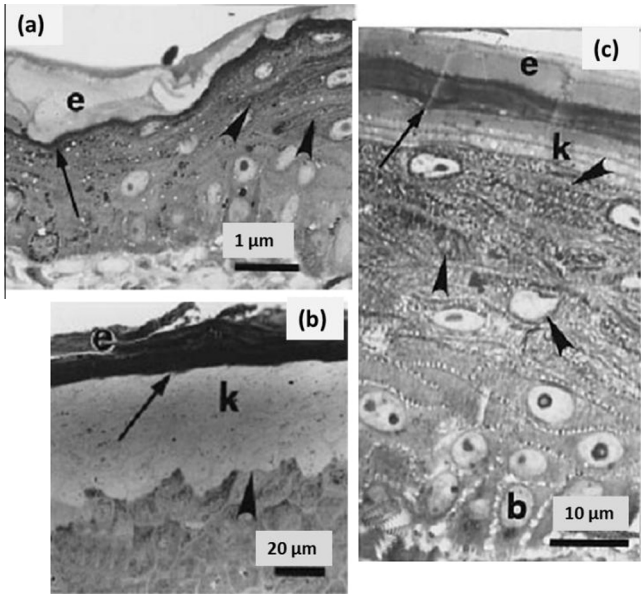

Fig. 11. Keratin layers of the developing carapace and plastron of a turtle (*Emydura macquarii*): (a) epidermis of the carapace showing a shedding layer (arrow) beneath the embryonic layers (e). The arrowheads show β-keratin cells. (b) At the end of embryonic stage for carapace, a thick β-layer (k) is observed. The arrow indicates the α-layer which sheds with embryonic layers. (c) The plastron at the end of embryonic stage. A β-keratinized layer (k) forms, beneath the epidermis. Arrowheads point to β-cells. b, basal layer [98].

2.4. Mechanical properties of α- and β-keratins

Keratinous materials exhibit exceptional mechanical functions depending on the host animals originated stemming from the complex hierarchical structures including the filament-matrix structure at the nanoscale and the diverse organizations of keratinized cells at micro and macroscales. It is of importance to first understand the mechanical behavior of α- and β-keratins at the nano and microscales, which is summarized in Table 7. The β-sheet has a higher stiffness than α-helix [100], and it has been long recognized that under tensile load the α-helices change the structure into β-pleated sheets [23,101–103]. In addition, mineralization with calcium and other salts can contribute to the hardening of keratins [104]. The alignment and volume fraction of filaments influence the mechanical properties of keratins, and humidity also plays an important role in the mechanical behavior of both α- and β-keratins.

2.4.1. Two-phase model for α-keratin

A two-phase composite model was first proposed by Feughelman [105] for wool fibers and has been widely used (this will be detailed in 3.1.2) in the literature. Models based on this two-phase

Table 7
Mechanical properties of α- and β-keratins.

Beta-keratin has a higher stiffness than alpha-keratin [100]	
Under tension the alpha-helices change the structure into beta-pleated sheets [101]	
Increasing humidity decreases strength and Young's modulus of α- and β-keratins	
Mineralization with calcium can contribute to the hardening of keratins [104]	
Orientation, packing and volume fractions of filaments for α- and β-keratins affects mechanical properties	
Two-phase model for α-keratin: crystalline IFs embedded into amorphous matrix; Matrix has been modeled as an elastomer, can interact with water, while IFs are water-resistant	No comprehensive studies found for β-keratin

structure correlating the IFs and matrix of α-keratin to the mechanical behavior have won different degrees of recognition [105–108]. The Chapman/Hearle model, assuming the IFs as ideal α-helical crystals and the matrix as a rather highly cross-linked swollen rubber, was considered fairly realistic [109]. The amorphous matrix has been modeled as an elastomer [110], and serves as a medium to transfer the applied load to the fibers, thus preventing crack propagation from a local imperfection or point of rupture [111]. However, there have not been similarly comprehensive studies found for β-keratin.

2.4.2. The α-helix to β-sheet transition

Fig. 12a and b [112] shows the changes of X-ray diffraction patterns of hagfish threads (bundles of IFs) under extension. The IFs bundles undergo the α → β transition at strains greater than 0.3; the unextended bundles exhibit the equatorial reflection of spacing of 0.98 nm and the meridional reflection of spacing of 0.515 nm, typical as α-keratin pattern; whereas the bundles extended to a strain of 1.0 yield a typical β-pattern with equatorial reflections of 0.97 nm and 0.47 nm. Fig. 12c shows schematically the α-helix to β-sheet transition in stretched α-keratin fibers (black arrows indicate tensile loading), in which the hydrogen bonds are reformed. X-ray diffraction patterns and spatial infrared microspectroscopy of horse hair [103,113] indicate that the process includes the progressive unraveling of the α-helical coiled coil domains, the refolding of the stretched α-helices into β-sheets, and the spatial expansion of the β-structured zones. The tensile stress–strain curve (Fig. 12d) exhibits three regions during this transition: a near linear Hookean region (up to 2–5% strain) where α-helices are stretched with bond arrangement altered but without substantial structural changes; a yield region between 2–5% and 30–50% strain, in which the α-helical coiled coils start unraveling and forming β-pleated sheets; a post-yield region with increasing slope where a majority of β-sheets are formed. The α-helix to β-sheet transition imparts a much enhanced energy-absorption capability to the structure because the area under the stress–strain curve is significantly increased. Upon unloading, part of the energy is recovered.

The mechanical properties of α-keratins at the molecular scale have been studied experimentally [114,115] and through atomic simulation [46] to understand the deformation and fracture behavior. Fig. 13 shows the simulated tensile force–displacement curves of a heterodimer and truncated tetramers (formed by two heterodimers) [46]. When pulling the heterodimer, in the first region (I), the force increases linearly with displacement until the rupture of the hydrogen bonds and uncoiling of α-helices. In (II), the pulling force fluctuates where α-helical domains of the dimer start unfolding, and in (III), the force increases rapidly with displacement due to stretching the covalent bonds of the polypeptide chain backbone. The heterodimer is stretched until all helical domains are fully extended. This agrees well with the experimentally observed stress–strain curves for α → β transition under tensile loading.

Fig. 13b and c shows the nanomechanics of disulfide cross-links in keratin proteins. Truncated tetramers without disulfide bonds (Fig. 13b) and with disulfide bonds (Fig. 13c) show similar region (I) as the heterodimer, where the pulling force increases with displacement until the rupture of hydrogen-bonds and uncoiling of α-helices. However, for tetramer without disulfide bonds the pulling force decreases in regions (II) and (III), which is analyzed as the failure of the tetramer by the sliding and cleavage of hydrogen-bonds. For truncated tetramer with disulfide bonds, the force increases to a peak value due to breaking the disulfide cross-links (two red arrows in Fig. 13c) between two dimers, indicating the strengthening effect of disulfide bonds. These molecular dynamic simulations provide good physical insights into the mechanisms of extension of segments of keratin (heterodimers, defined in Fig. 4). The α-helix ↔ β-sheet transition in the keratin-like proteins of oviparous gastropod eggs has also been studied in depth through a thermodynamic formalism, in which distinct variables (e.g. internal energy driven rather than entropy) are assessed [116]. Other coiled coil proteins, such as myosin II and possibly fibrin, also show this transition [18].

2.4.3. Viscoelasticity

It is widely accepted that elastic materials show identical paths when loaded and unloaded without energy dissipation, while viscous materials exhibit different loading and unloading paths. Viscosity represents a fluid's resistance to flow and is measured by the ratio of the shearing stress to the velocity

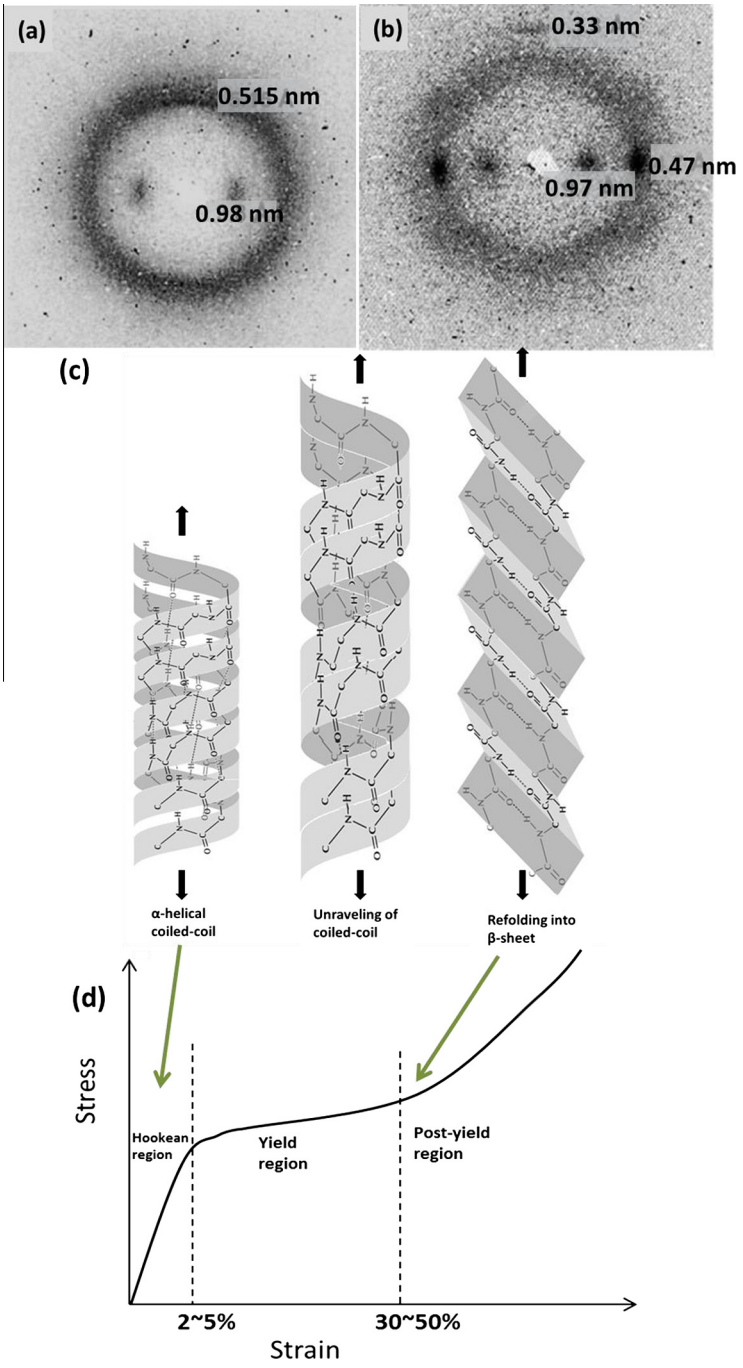

Fig. 12. The α-helices to β-sheet transition under tensile loading. X-ray diffraction patterns of keratin bundles from hagfish slime threads [112]: (a) unstrained threads (α-keratin) and (b) strained threads (β-pattern). Schematic diagrams showing: (c) the α to β transformation in (arrows indicate the direction of tensile loading) and (d) Hookean, yield and post-yield regions on the tensile stress–strain, during which the transformation proceeds in yield and post-yield regions.

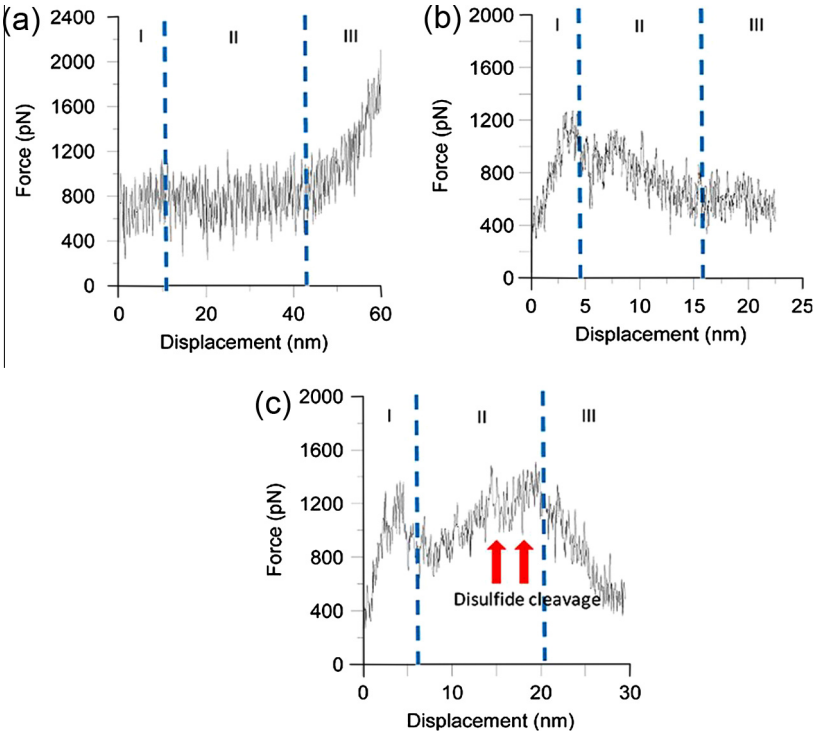

Fig. 13. Tensile force–displacement relationships from molecular dynamics simulation showing three regions: (a) the heterodimer: (I) as the displacement increases, the force increases until rupture of hydrogen bonds takes place and promotes uncoiling of the α-helices; (II) unfolding of the dimer results in a plateau of constant force; (III) finally, stretching of the C–C backbone results in a large increase of force with displacement; (b) the truncated tetramer model without disulfide cross-links: (I) linear relationship between force and displacement; (II) the force decreases with increasing displacement due to dimer sliding and cleavage of hydrogen bond between dimers; (III) failure; (c) the truncated tetramer model with disulfide cross-link: (I) linear relationship between force and displacement; (II) C–C backbone stretching causes a large increase in force which ultimately leads to breaking of the two disulfide cross-links (indicated by red arrows); (III) facile sliding of the dimers [46].

gradient. Most biological materials are neither purely elastic nor solely viscous; instead, they exhibit a combination of both and are hence termed viscoelastic [117]. The viscoelasticity is of primary importance for keratinous tissues not only to provide mechanical support and sustain impact but also to absorb energy and dampen load fluctuations. This power law decay of longitudinal and transverse waves is enhanced by the viscous component because the sliding of chains that are often connected by weaker bonds than the polymer backbone bonds, and by processes of chain reorganization under stress.

A viscoelastic solid will undergo creep (deformation as a function of time when the load is held constant) and stress relaxation (stress reduction as a function of time when the strain is held constant). The elastic and viscous components have been modeled as a combination of springs and dashpots (shock absorbers), respectively. The spring is characterized by the linear elastic equation:

$$\sigma = E\varepsilon \tag{1}$$

The dashpot is, for an ideal (Newtonian) viscous material:

$$\sigma = \eta \frac{d\varepsilon}{dt} \tag{2}$$

Fig. 14a–c [8] shows three configurations of springs and dashpots that are commonly used to describe viscoelastic behavior: the Maxwell model, a spring and a dashpot in series sharing the same

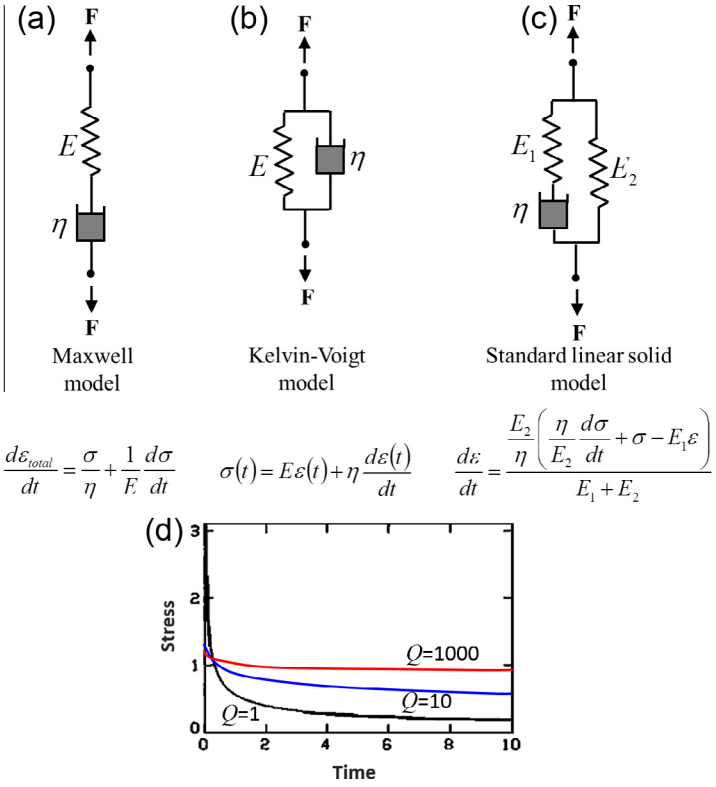

Fig. 14. Three common models to describe the viscoelastic behavior with equations in terms of stress and strain given [8]: (a) Maxwell model; (b) Kelvin–Voigt model; (c) standard linear solid or Zener model. (d) Effect of $Q^{-1} = \tan\delta$ on the attenuation of elastic longitudinal waves; stress and time are normalized (adimensional) values [119].

stress; the Kelvin–Voigt model, a spring and a dashpot in parallel sharing the same deformation; and the Standard linear solid or Zener model, a Maxwell model in parallel with a spring. Actual material behavior is often more complex, and thus additional springs and dashpots are required to be added to study the mechanical response.

One consequence of viscoelasticity is the material strain rate sensitivity, which is more practical in experimental study. This indicates the variation of mechanical properties as a function of strain rate, and a possible transition from ductile (or pseudoductile) to brittle fracture behavior with increasing strain rate [117]. Generally, as the strain rate increases, keratinous tissues become stiffer and stronger with decreasing breaking strain, whereas the toughness (the area under stress strain curve) may not follow the same trend but depend on the specific mechanical needs of the host animals. This will be discussed for particular keratinous materials in Section 3.

Viscoelasticity has a profound effect on the ability of hooves and horns to absorb energy before transmitting it to the skeletal frame of animals [118]. The impact on the hooves from the ground and on horns from fighting generates elastic waves propagating into the material. The analysis by Kjartansson [119] provides a valuable insight into the attenuation of elastic waves due to viscoelasticity. One defines a parameter Q:

$$\frac{1}{Q}=\tan\delta \tag{3}$$

δ is the phase angle between stress and strain and represents the ratio between the loss and storage moduli (E''/E'). For a perfectly elastic material, $\delta = 0$ and Q is infinite. Fig. 14d shows the attenuation for

three cases: $Q = 1$, 10 and 1000. Bonser and Purslow [120] measured the $\tan\delta$ for feather keratin and quoted a range of 0.03–0.07 at ambient temperature, increasing with temperature. Thus the value Q fluctuates around 10 and this has, as shown in Fig. 14d, a profound effect on decay of a stress pulse. Another contributory factor, which will be discussed in Section 3.1.5 (hooves and horns), are the cylindrical voids (tubules) that cause scattering of waves [121].

2.4.4. Hydration sensitivity

The mechanical properties of both α- and β-keratins are highly influenced by the water content. As the humidity increases, the stiffness and strength decrease whereas the breaking strain increases. X-ray diffraction and experimental studies [16,17,105,111,122] revealed that the matrix proteins could be considered as water-sensitive, whereas the IFs are crystalline and not mechanically affected. This can be applied to keratinous materials since IFs are identical in all mammalian hard keratins [16,123]. Different explanations accounting for how water molecules interact with the matrix proteins are schematically illustrated in Fig. 15:

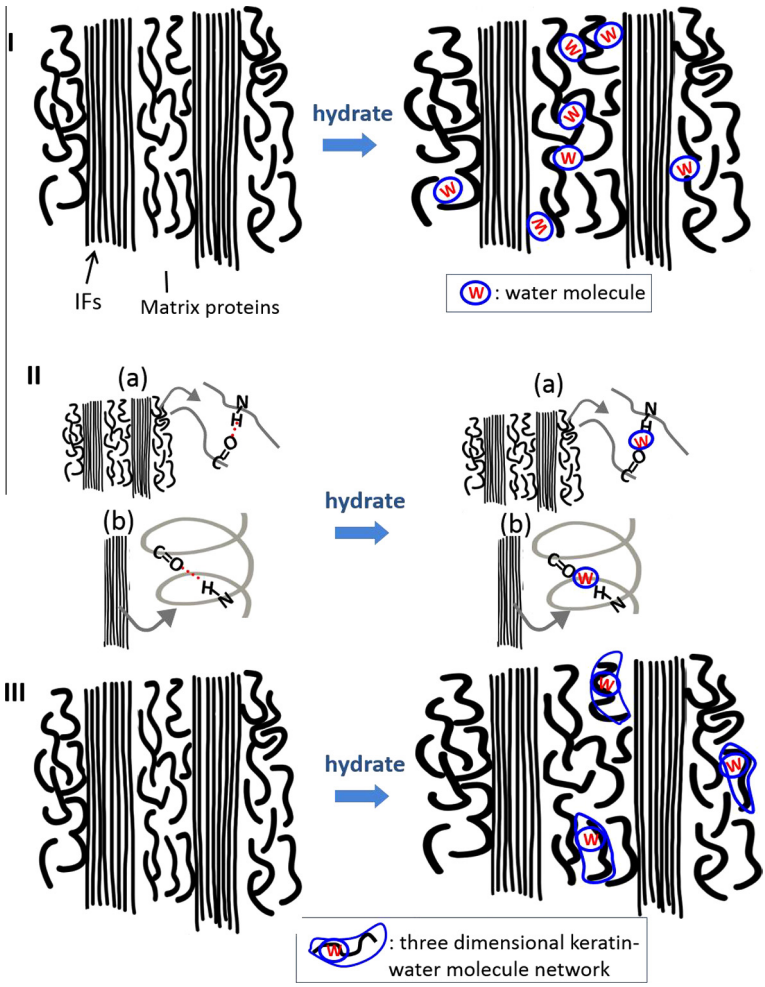

Fig. 15. Schematic diagrams of proposed water interaction with α-keratin: (I) water act as cross links and a swelling agent to increases the distance between matrix proteins, (II) water may replace the hydrogen bonds in the matrix protein chains and/or in the IFs, and (III) in the matrix, water may form a three dimensional keratin–water network.

- water may act as a cross link between chains and a swelling agent thereby reducing interchain interaction and increasing interchain space [122] (Fig. 15I);
- water may breakdown/replace the extensive secondary bonding, such as hydrogen bonding, between glycine/tyrosine-rich proteins in the matrix phase, thus increasing protein mobility [111,123] (Fig. 15II, a);
- water may form a three-dimensional keratin–water molecule network that works as a plasticizer, reducing the stiffness and increasing the segmental mobility of the molecular structure of the matrix [17,122] (Fig. 15III).

There are also studies on fibers composed of matrix-free IF bundles (hagfish slime threads) [115,124]. Interestingly, they reveal that in the absence of matrix proteins, the IF bundles show mechanical properties with more significant hydration sensitivity than α-keratinous materials with matrix proteins (detailed in Section 3.1.8). This implies that the water may also affect the structural bonds within IFs or the disordered region within the fibers [115,125] (Fig. 15II, b).

2.5. Keratin research history

The earliest use of keratins should come from a Chinese herbalist, Li Shi-Zhen in the 16th century for medicinal application [126]. The word "keratin" firstly appears in literature around 1850 for materials that make up hard tissues such as horns [127].

During the early twentieth century, the research focus had been to extract keratin from animals and human hair: a patent [128] described a process for extracting keratins from horns using lime; it was reported that keratins can be converted into proteins soluble in alkali or acid [68]. With the biological properties of keratin extracts known, their medical applications became hot topics, including keratin powders for cosmetics and coatings for drugs [129,130]. During 1920s, the focus changed from keratin products to the structure and properties of keratin proteins, recognizing that different keratin forms are present in keratin extracts [127].

During World War II and after that, the driving forces of keratin research were textile production as well as its medical, cosmetic and engineering applications. In 1940, in Australia, the Council for Scientific and Industrial Research established the Division of Protein Chemistry to better understand the structure and chemistry of fibers to expand the potential applications of wool and keratins, and produced the first complete diagram of a hair fiber (Fig. 20, [131]). There were more than 700 applications of keratin-based inventions submitted to the Japanese patent office in the thirty years after that [127]. In the 1950s and earlier, the University of Leeds and the Wool Industries Research Association in the UK showed that wool and other fibers consist of an outer cuticle with flat overlapping cells and a central cortex with elongated cells [132].

Since the 1970s, advances in the extraction and characterization of keratins have led to the exponentially growing knowledge of keratin and keratinous materials [16,111,133]. On the one hand, this enabled the increased production of keratin-based powders, films, gels, and coatings [134]. Keratin based biomaterials in medical applications show a good potential [135,136]. Wound healing, drug delivery, tissue engineering, cosmetics, and medical devices continued to be popular subjects for keratin-based research in the past decades [127]. On the other hand, the enhanced understanding of keratins has fueled the research area of biological keratinous materials with the aim to create bioinspired materials. Some keratinized materials with interesting properties, such as skin [137], quills [138,139], fingernails [140], horns [141,142], whelk egg capsules [116], and bird feathers [143,144], have been studied, with the hopes to obtain mechanisms and principles to design new functional materials, such as light-weight composites, and energy-absorbent materials [145]. This is a new and fascinating area, awaiting more and in-depth explorations.

3. Structure and mechanical properties of keratinous materials

Keratinous materials show the typical filament-matrix structure and exhibit a wide range of mechanical properties. Fig. 16 summarizes the transmission electron micrographs of keratinous mate-

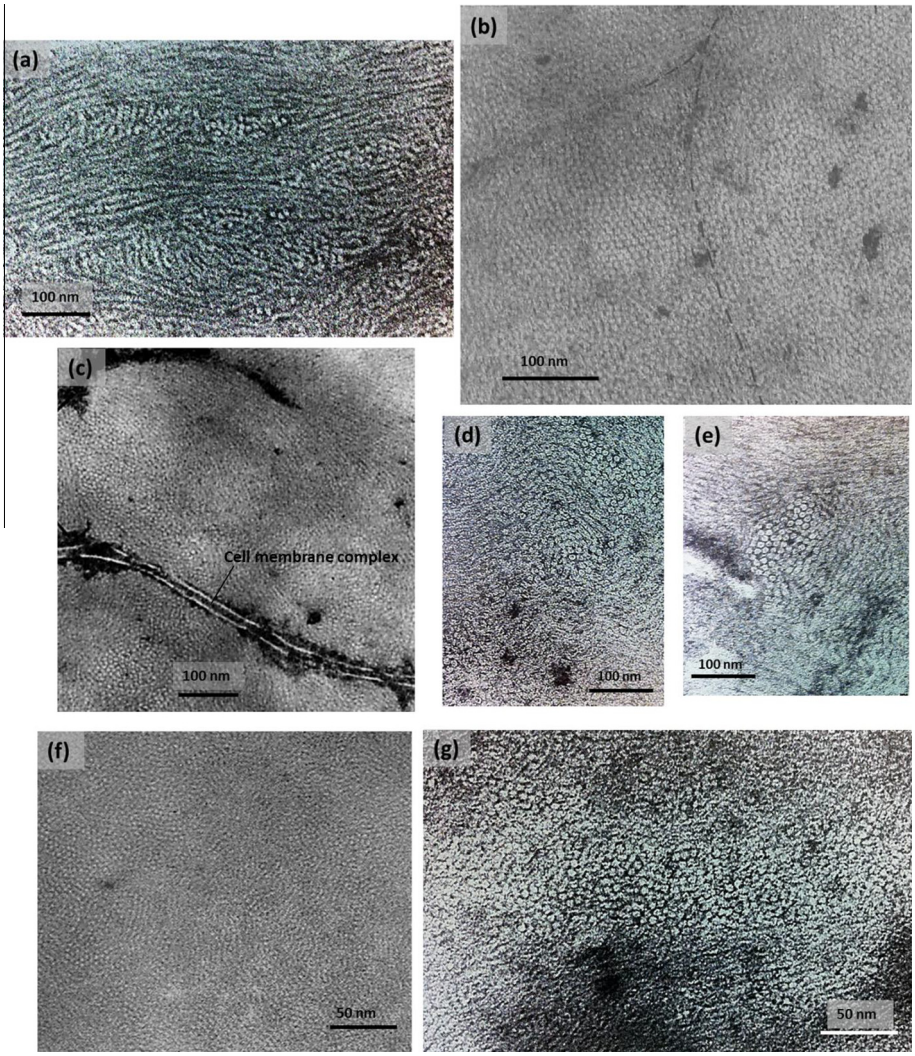

Fig. 16. Transmission electron micrographs showing the filament-matrix structure of α- (a–e) and β- (f and g) keratinous materials: (a) stratum corneum of human skin [84], (b) Merino wool fiber [147], (c) porcupine quill tip (with cell membrane complex indicated) [146], (d) bovine horn and (e) human nail [16], (f) seagull feather rachis [91] and (g) fowl claw [16]. The 7 nm diameter intermediate filaments and 3 nm diameter beta-keratin filaments embedded in matrix are observed.

rials composed of α-keratin and β-keratin [16,84,91,146,147]. For all figures except for a, e and g, the filaments are perpendicular to the foil plane and therefore show circular profile. Stratum corneum, wool, quill, horn, and fingernail show clear IFs embedded in an amorphous matrix (electron dense, dark background). The diameters of the IFs (∼7 nm) appear to be substantially constant, but there are wide variations in the IFs orientations. Feather and claw exhibit beta-keratin filaments (3–4 nm diameter) embedded in an electron dense matrix.

Fig. 17 compares the tensile stress–strain curves of several typical keratinous materials (whale baleen from [14], wool from [148]). All curves are characterized by a response that resembles that of metals:

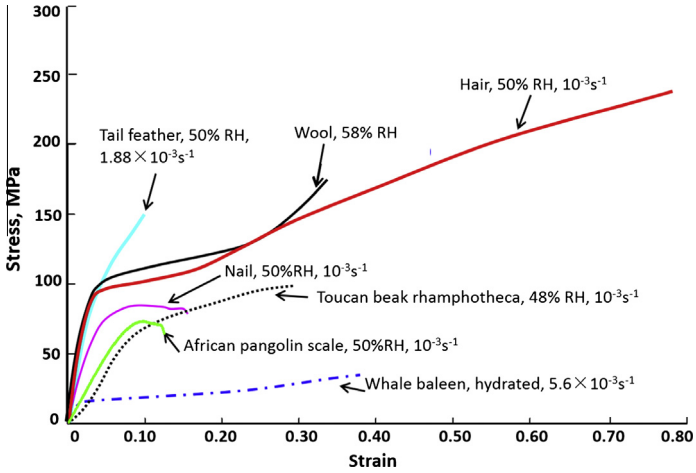

Fig. 17. Tensile stress–strain curves of several typical keratinous materials (wool from [148], whale baleen from [14]).

(a) a linear portion, corresponding to the elastic region, with a Young's modulus ranging from 1 to 5 GPa. Care should be taken in evaluating these values because some researchers may not use extensometers and therefore the slope incorporates machine effects;
(b) a plastic region with a much lower slope;
(c) a slope change corresponding to strengthening (slope increase) or failure (slope decrease).

Hair and wool show an initial linear region, a yield region with an inflection and a post-yield region where the materials stiffen and break. Nails show similar curve with lower stiffness and strength. Whale baleen in hydrated condition also exhibits the three regions but substantially lowered strength and longer yield region. The feather shows an elastic modulus that is similar to wool, but fractures without an obvious yield region. The toucan beak is less stiff and shows somewhat a yield region. The pangolin scales fracture after a very short plastic region. These different responses are a consequence of the structural organizations of the filaments and matrix, the arrangements of keratinized cells and/or sample preparation. The small diameters of wool, hair and hagfish slime threads lead to greater ductility because crack formation and propagation are retarded and the α to β transformation provides an additional strain.

Table 8 lists the mechanical properties of different keratinous materials. It is clear that their mechanical behavior is highly dependent on hydration levels, and the mechanical properties encompass a large variation: the Young's modulus and strength range from 0.005 to 4.5 GPa and 18 to 221 MPa, respectively under similar relative humidity. This will be detailed in each keratinous tissue in the following sections.

3.1. Keratinous materials based on α-keratin

The stratum corneum, wool and hair, quills, horns, hooves, nails, whale baleen and hagfish slime are presented in this section.

3.1.1. Stratum corneum

Stratum corneum is the outermost layer of mammalian skin (about 20–40 μm thick, Fig. 8a; [81]) and serves as a diffusion barrier, defense from external attack and even camouflage from predators [5]. It is composed of flattened cornified keratinocytes; these anucleated cells are embedded in a lipid-rich intercellular matrix. The keratin filaments extend throughout the entire cytoplasm in a web like pattern, and integrate at cell–cell junctions, maximizing the mechanical support [156]. From the top sur-

Table 8
Mechanical properties of different keratinous materials.

Materials	Young's modulus (GPa)	Fracture strength (MPa)	Fracture strain	RH (relative humidity)	Ref.
Stratum corneum	1	18		10% RH	[149]
	0.005	2		100% RH	
Wool		260	0.30	0% RH	[111,148]
	4.5			65% RH	
	2.5	180	0.57	100% RH	
Quill	2.7	146	0.25	65% RH	[150]
	1.0	60	0.49	100% RH	
Horn	3.9	77	0.035	50% RH	[151]
	0.7	25	0.61	Soaked in water	
Whale baleen	1.2	30	0.35	Immersed in sea water	[14]
Hagfish slime threads	0.006	180	2.2	Tested in sea water	[112]
Feather	3.7	221.0	0.092	0% RH	[152]
	1.5	106.3	0.163	100% RH	
Beak	1.3	47.5	0.122	50% RH	[153]
Claw	2.7	90.3	0.057	0% RH	[152]
	2.1	68.7	0.067	50% RH	
	0.14	14.3	0.205	100% RH	
Snake epidermis[a]	3.43–4.73 (inner to outer)			43% RH	[154]
Pangolin scale	0.963	72.43	0.13	50% RH	[155]

[a] Effective elastic modulus from nanoindentation.

face planar view (Fig. 18, [157]), overlapping layers (about 15–20 layers) of dead cells with approximately 25–45 μm in diameter are observed [158]. The cells are continuously exfoliating and being replaced by those from the living layers beneath. These cells migrate through the epidermis toward the surface of skin, which takes approximately fourteen days [159]. In most of the cells, the cytoplasmic space is completely filled with filaments (IFs) about 7 nm in diameter embedded in a matrix of high sulfur proteins. The IFs are arranged in a variety of orientations (Fig. 16a).

The mechanical properties are highly dependent on the relative humidity, temperature and loading orientation. Fig. 19 shows the tensile stress–strain curves of new born rat stratum corneum. With

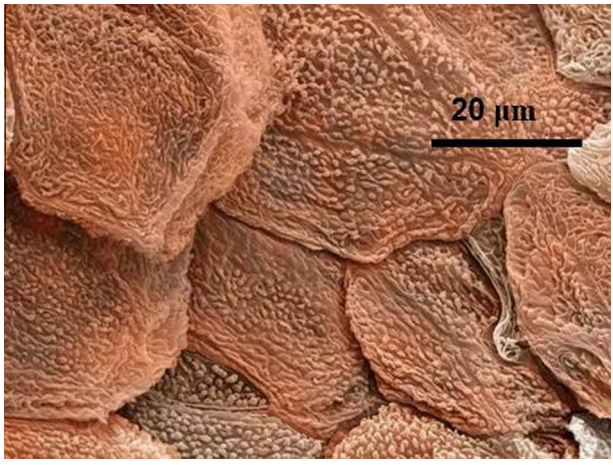

Fig. 18. Colored scanning electron micrograph of top surface of stratum corneum of human skin, showing the overlapping, layered keratinocytes [157].

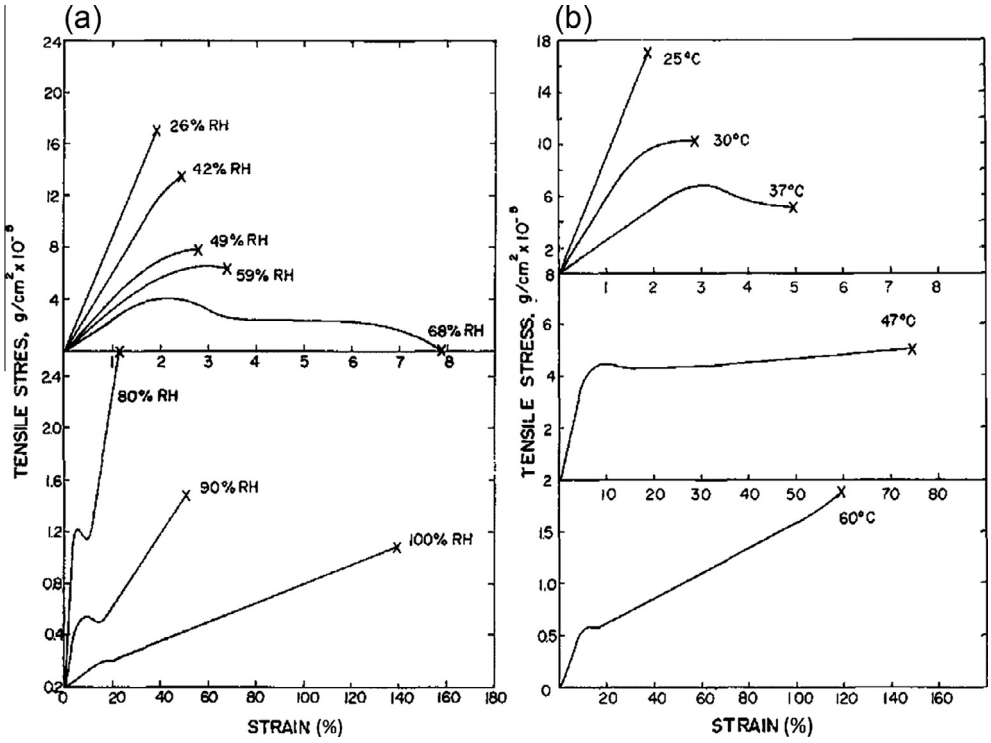

Fig. 19. Tensile tests (stress–strain curves) of new born rat stratum corneum at strain rate of 0.5 cm/min [160]: (a) curves at 25 °C and different humidities; (b) curves at 10% water content at different temperatures.

increasing moisture content and temperature, both modulus and strength decrease, but breaking strain increase [160]. This is related to a molecular relaxation process, and the strong plasticizing action of water facilitates the glass transition temperature of the fibrous protein component to migrate to lower temperatures with increasing moisture content. With more absorbed water, the interchain hydrogen bonds between amide and carbonyl groups are replaced by direct water–polymer linkages, and the segmental mobility of the macromolecular backbone increases, thus reducing the strength [160]. The Young's moduli of porcine stratum corneum measured by nanoindentation were reported to be 10 MPa (wet) and 100 MPa (dry) [161]. In-plane tensile moduli of human stratum corneum ranges from 5 MPa to 1000 MPa with decreasing water content [149]. The in-plane tests show cohesive strengths of 2–18 MPa in testing environments of 100–0% relative humidity, and out-of-plane strengths of 0.1–0.8 MPa (100–45% relative humidity) [149].

In vitro adhesion tests reveal that the human stratum corneum shows a graded intercellular delamination behavior: delamination energies increase from $\sim$3 J m^{-2} near the surface to $\sim$15 J m^{-2} for the inner layers, while the delipidized specimens show initial delamination closer to the stratum corneum center and higher delamination energies than untreated ones [162]. Studies of the effects of solar UV radiation on the barrier function of stratum corneum revealed that with increasing UV exposure to 800 J cm^{-2}, equivalent to 60 continuous days radiation, the stiffness remains constant but the fracture stress decreases, and the fracture strain and delamination energy decrease significantly, indicating the damage to the intercellular cohesion [163].

3.1.2. Wool and hair

Wool is a noteworthy example of the hard keratinous material. It is by far the most important animal fiber used in textile application, and the structure and mechanical behavior have been extensively stud-

ied [16,17,25,38,111,131,164]. A clean wool fiber contains approximately 82% keratinous proteins with a high concentration of cysteine. About 17% is protein material of low cysteine content termed 'non-keratinous material' located primarily in the cell membrane complex, and about 1% of non-proteinaceous material consists of waxy lipids, plus a small amount of polysaccharide material [58].

Wool fibers (with a diameter ~20 μm) consist of cells: flattened cuticle cells form a sheath around the cortical cells and continuous intercellular materials. Fig. 20 shows the hierarchical structure of a merino wool fiber [131]: the outermost layer, cuticle, consists of overlapping scales and it constitutes about 10% weight of the total fiber. The middle cortex, formed by spindle-shaped cells about 100 μm long, consists of orthocortex and paracortex (Fig. 21a and b), which have different assemblies of structural components and lead to the curly nature of the wool [165]. Lipid-rich cell membrane complex holds the cortical cells together in which macrofibrils formed by IFs (microfibrils in Fig. 20) and matrix proteins are observed. At the nanoscale, the α-helix chains associate into IFs, and then are embedded in a sulfur-rich matrix, which consists of proteins, nuclear remnants, cell membrane complex, intercellular cement. Fig. 21 [16] shows optical and transmission electron micrographs of stained merino wool. The cells in orthocortex are more densely stained than those in paracortex from optical observation (Fig. 21a), and the orthocortical cells and paracortical cells have different IFs/matrix packing arrangements [146,147,166]: the IFs in the paracortex (Fig. 21c) are more uniform and show clear hexagonal packing; whereas in cross-sectioned orthocortex (Fig. 21d), the IFs are organized into discrete bundles with a characteristic appearance resembling the 'whorl' of a finger print. The amount of matrix in the paracortex appears to be greater than that in the orthocortex, which has been confirmed by electron diffraction [167].

The tensile properties of wool are largely understood in terms of the two-phase composite model (Fig. 22a): crystalline IFs are embedded in an amorphous, water-sensitive matrix [105]. Several variations of this model have been used [106–108,110,164,168,169], and a review has critically evaluated the relevant models [109]. Present below are the essential elements of the two-phase model (rule of mixtures). It is assumed that both the IFs and matrix undergo the same strain. This is actually a simplification, because sliding of the IF in the matrix takes place and the interfacial shear stresses between them are not constant.

At each strain ε:

$$\sigma = V_f \sigma_f + V_m \sigma_m \tag{4}$$

where V_f and V_m are volume fractions of IF and matrix, and σ_f and σ_m are stresses acting on IF and matrix. The IFs and matrix stresses have functional dependencies of the strain, $f_f(\varepsilon)$ and $f_m(\varepsilon)$. Thus, the general expression, applicable to any strain ε, is:

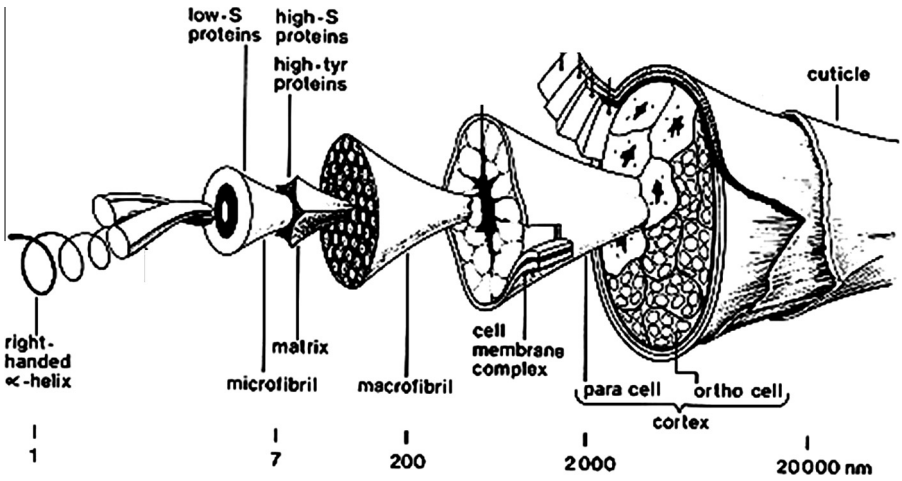

Fig. 20. Schematic of the hierarchical structure of a fine merino wool fiber [131].

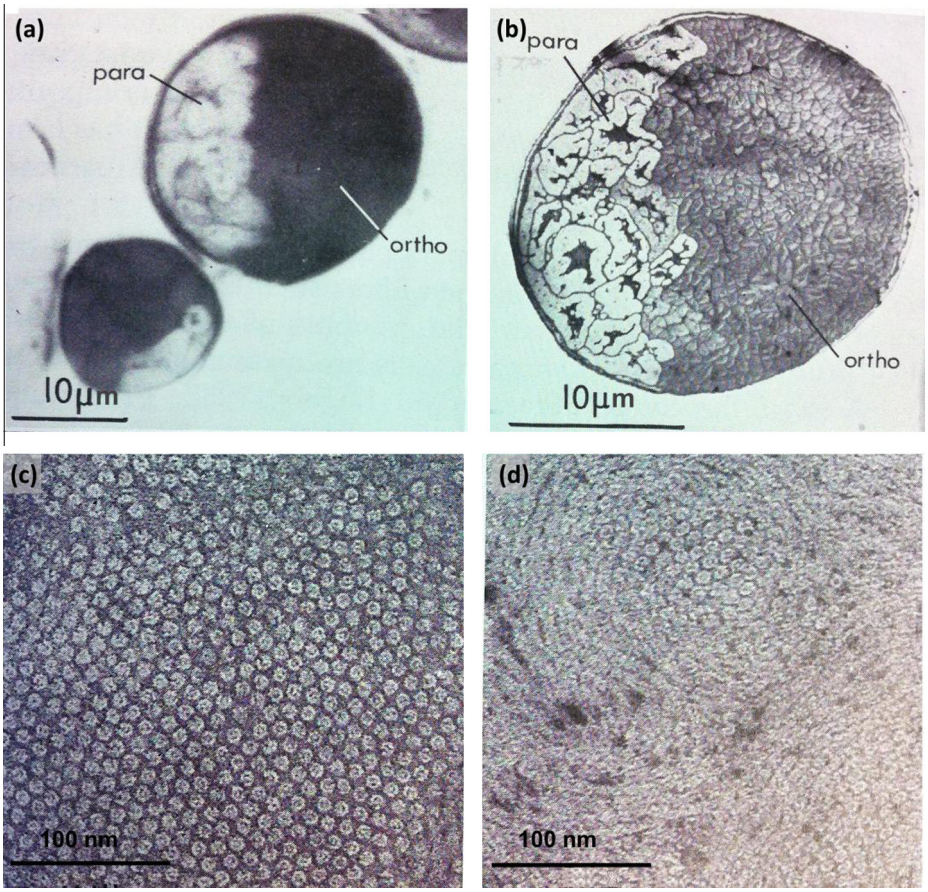

Fig. 21. Microstructure of Merino wool: (a) light microscopy of cross section of Merino wool. Transmission electron micrographs of (b) a cross section of Merino wool, the paracortex (para) and orthocortex (ortho) show clearly different morphologies; (c) quasi-hexagonal array of intermediate filaments (circular shape) embedded in matrix in the paracortex; (d) whorl-like pattern of intermediate filaments in the orthocortex [16,147].

$$\sigma = V_f f_f(\varepsilon) + V_m f_m(\varepsilon) \tag{5}$$

Fig. 22b shows the stress–strain curves of IFs, matrix and the fiber from a modified two-phase model for α-keratin fibers [107]. Three distinct regions can be discerned: a near linear region (Hookean region) up to 2% strain which is associated with stretching of the α-helices with changes in bond angles without significant change in structure within the IFs [109]. Between 2% and 30% strain, the yield region, the unfolding of α-helices into the β-sheet configuration occurs and progresses in the IFs. In the post-yield region (after 30% strain), the fiber stiffens and breaks [170]. X-ray analysis has shown that the α to β transformation proceeds gradually through both the yield and post-yield regions [171].

Fig. 22c shows the predicted stress–strain curves of separate IF and matrix based on another two-phase model [110]: the curve for IF increases initially to a critical stress (point c) where unfolding of α-helices and formation of β-phase starts, then the stress drops to an equilibrium stress (eq) and remains constant as the transition of α to β proceeds until completion; further increase in stress stretches the β-form elastically. The matrix is assumed to be a cross-linked elastomer and shows smoothly increasing stress as strain increases, and the curve fits exactly a large large-strain rubber–elasticity stress–strain relationship Eq. (6) [172] for up to 35% strain:

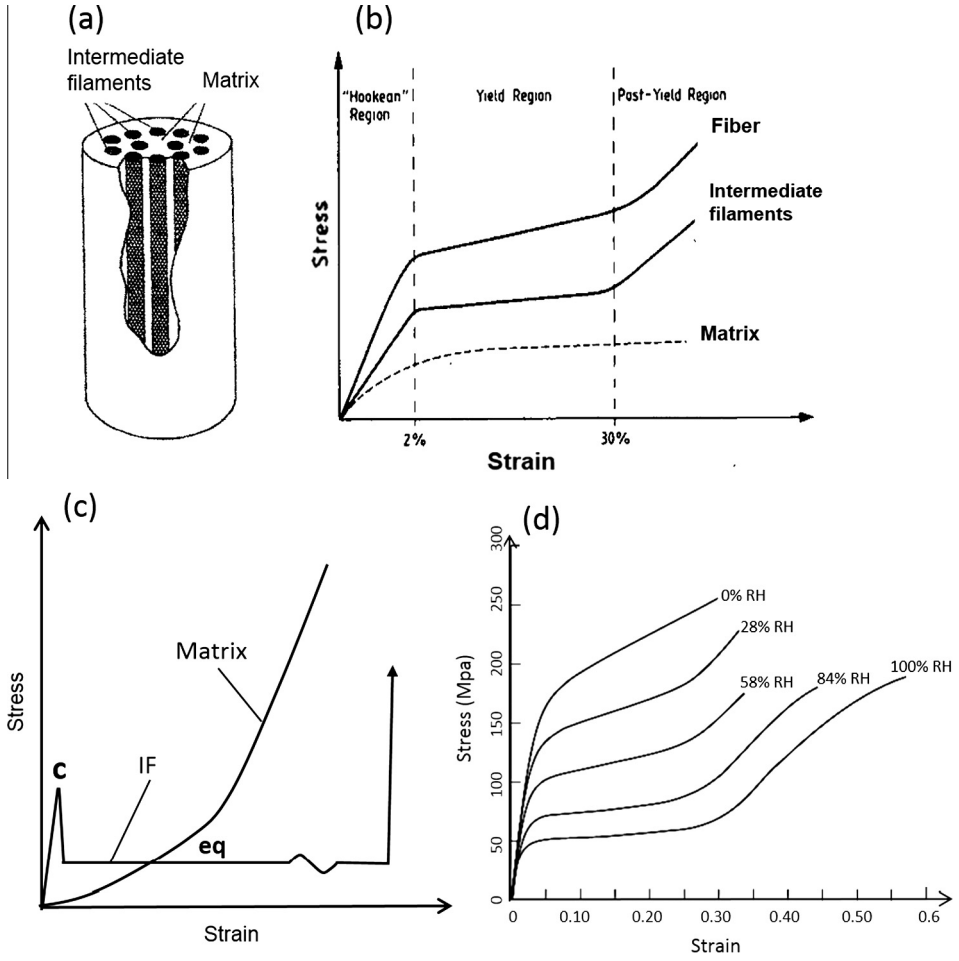

Fig. 22. (a) Two-phase composite model for a wool fiber: cylinders of intermediate filaments (IFs) embedded in matrix [105]; (b) schematic stress–strain curve proposed for a wool fiber in water (not drawn to scale) [107]; (c) stress–strain curves of independent IF and matrix from a modified two-phase model (c, critical stress; eq, equilibrium stress) (reproduced from [110]); (d) stress–strain curves of wool fibers at different relative humidities (RH) [148].

$$\sigma = (NkT/3)n^{\frac{1}{2}}\left[L^{-1}(\lambda/n^{\frac{1}{2}}) - \lambda^{\frac{3}{2}}L^{-1}(1/\lambda^{\frac{1}{2}}n^{\frac{1}{2}})\right] \tag{6}$$

where σ is stress, N is the number of chains per unit volume, k is the Boltzmann's constant, T is the temperature, n is the number of random links between cross-links, λ is the stretch ratio ($\lambda = \varepsilon + 1$), and L is the Langevin function, defined, for a general variable x, as $L(x) = cothx - 1/x$. The Treloar equation is based on entropic effects associated with chain extension. Recent studies on whelk egg capsules, which also show the α-helix → β-sheet transition that is reversible (detailed in Section 3.1.9), have found that the process is driven more by internal energy than entropy changes [116,173].

There is general agreement in the literature as to the structure–mechanical relationships in the Hookean and yield regions [106], but studies explaining the post-yield region are still somewhat questionable. Some explanations accounting for the increase of slope in this region are:

- the straining of the stretched matrix in parallel with IFs at the equilibrium stress [108–110];

- the manner in which β-structured zones expand from the center of α coil domains to the periphery [103];
- the unfolding of the remaining α-helices produces the increase [107];
- the further extension of the unfolding α-helices and extending the matrix protein jammed alongside the IFs. This is expressed by Eq. (7) to calculate the fraction of unfolded α-helices, x, required to obtain a strain ε at the turnover from yield to post-yield region, where V_s is the volume swelling for wet fiber above dry one at the end of the yield region (defined as the volume change from dry to wet divided by dry fiber), V_f is the IF volume fraction in the material. Feughelman [106] assumed a change in length by a factor of 2.25 for a polypeptide unit as it is transformed from α-helix to a β-unit.

$$V_s = 1.25V_f x + \frac{2.25x}{(1-x)}(1-V_f) \tag{7}$$

After obtaining the fraction of unfolded α-helices, x, Eq. (8) is employed to calculate the strain ε, and 0.02 corresponds to the strain at the end of Hookean elastic region.

$$\varepsilon = 1.25x + 0.02 \tag{8}$$

Feughelman [106] reported that the estimated strain ε at the turn-over from yield to post-yield region agrees well with direct experimental measurements: for Corriedale (sheep) wool fibers, $V_s = 0.42$ and $V_f = 0.56$; using Eq. (7) one obtains $x = 0.21$; then by Eq. (8), $\varepsilon = 0.29$. In comparison, the ε value of 0.30 is obtained for the same fibers experimentally, demonstrating excellent agreement.

The hydration has a great influence on the longitudinal tensile properties. The dehydration of wool fibers increases the tensile modulus approximately threefold, but increases the torsional modulus by a factor of 15 [105]. The smaller change in tensile modulus indicates that the IFs, carrying the majority of the stress in this direction, are only slightly affected by decreased hydration. However, the large change in torsional modulus indicates that the matrix properties are strongly affected by hydration. In torsion, the matrix carries a large portion of the applied stress. It can be concluded that dehydration affects the properties of the matrix to a far greater degree than it does the IFs [111]. Fig. 22d [148] shows that the yield stress and breaking stress decrease with increased water content, which was

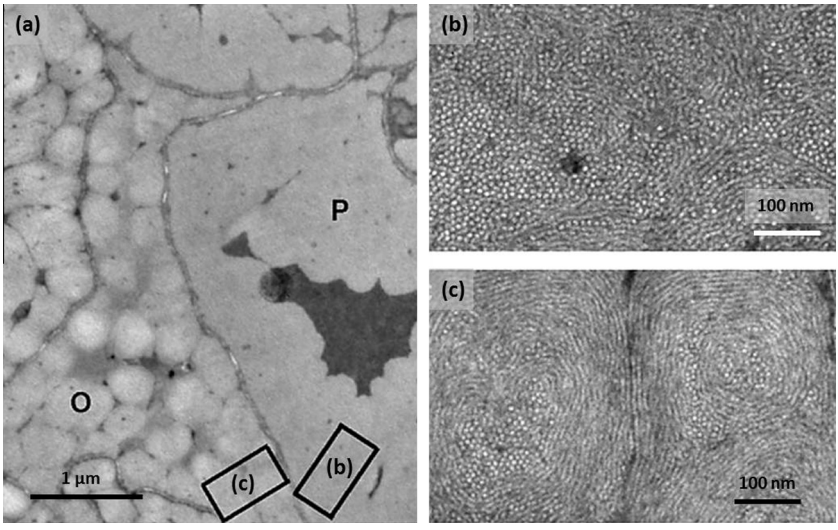

Fig. 23. Transmission electron micrographs of a red deer hair: (a) cross section of the hair showing the paracortex (P) and orthocortex (O). High magnification images of rectangular regions (b and c) are shown in (b) and (c); (b) hexagonally arranged IFs embedded in matrix in paracortex; (c) IFs arranged in a whorl-like pattern in orthocortex [174].

attributed to the action of water in the α-keratin–water network: as a cross link between keratin chains, as a swelling agent reducing interchain interaction, and as a plasticizer of the keratin structure [122]. The tensile strength of wool decreases from 260 to 150 MPa as the relative humidity increases from 0% to 100%. Considering that the density of keratinous materials is around 1 g/cm^3, wool has specific strengths (tensile strength/density) ranging from 150 to 260 kN m/kg, comparable to that of stainless steel, about 250 kN m/kg (2000 MPa and 7.9 g/cm^3 as the tensile strength and density, respectively).

Hair is another important fiber that has been widely used and studied. The structure of hair shows many features same as wool except for a larger diameter (~80 μm): the fiber consists of flattened cuticle cells overlapping around cortical cells and a central medulla (may be discontinuous or absent); the cortex forms bulk of the hair shaft and is composed of paracortex with hexagonally aligned IFs in matrix and orthocortex with IFs arranged in a whorl-like pattern, shown in Fig. 23 [174]. The proportions of paracortical and orthocortical cells determine the straightness of hair.

The mechanical properties of hair have been studied, but not as extensively as wool. Fig. 24 shows the tensile stress–strain curves and results of human hair at different strain rates [175]. All curves

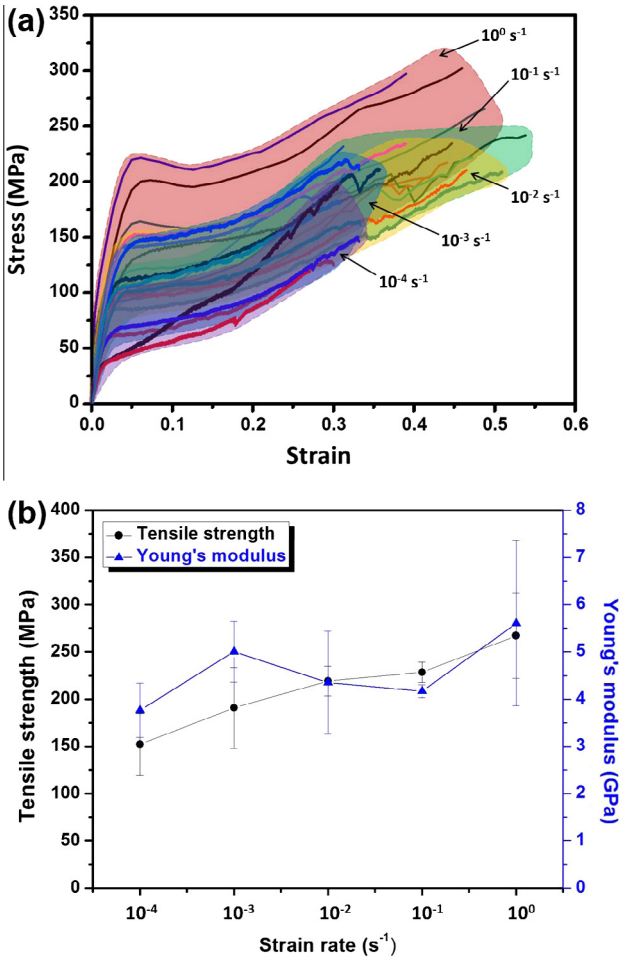

Fig. 24. Tensile results of human hair at different strain rates [175]: (a) stress–strain curves grouped for each strain rate; (b) Young's modulus and tensile stress as a function of strain rate (error bars indicate standard deviation).

show the three regions typical of α-keratin: a linear Hookean region, a yield region and a post-yield region. It is clear that as strain rate increases, the yield stress, tensile strength and Young's modulus increase from 100 MPa to 220 MPa, from 160 to 250 MPa, and from 4 to 5.5 GPa, respectively. It has been accepted that for wool the cuticle cells contribute little to the mechanical properties since they are loosely organized on the fiber. However, one interesting finding of the cuticle cells of human hair was observed: the cuticle cells of unstretched hair originally overlap in a closed mode (Fig. 25a); they become open (Fig. 25b) after stretched at a relatively high strain rate (10^0 s^{-1}) [175], and this opening is not obvious for hair stretched at lower strain rate (10^{-3} and 10^{-4} s^{-1}). This change indicates that the cuticle cells may also play a role in mechanical deformation of hair. Fig. 25c and d represents the fibrous structure of hair: the fracture surface shows relatively smooth morphology of fractured fibers and the side view clearly shows the fibers.

3.1.3. Quills

Quills are the hard keratinous materials covering porcupines, hedgehogs, and echidnas, to protect them from aggressors. Porcupine quills are designed to pierce opponents and resist axial load and bending, and have been studied widely [138,139,150,176–179]. Porcupines can be divided into two main families: Old World (African porcupine) and New World (American porcupine). Fig. 26 [179] shows the morphologies of African and American porcupine quills: both consist of a stiff outer sheath and a porous core, an assembly that maximizes the flexure strength/weight ratio [12]. The African porcupine quills are embedded in clusters. They are long and thick (35–50 cm), and have stiffeners attached to the cortex (Fig. 26c), gradually extending to the center with foam-like cells filling the remaining area. The surface of African porcupine quills shows irregular scales on the cortex and pores (diameter about 100 nm) [179]. The American porcupine quills are interspersed with hairs. They are

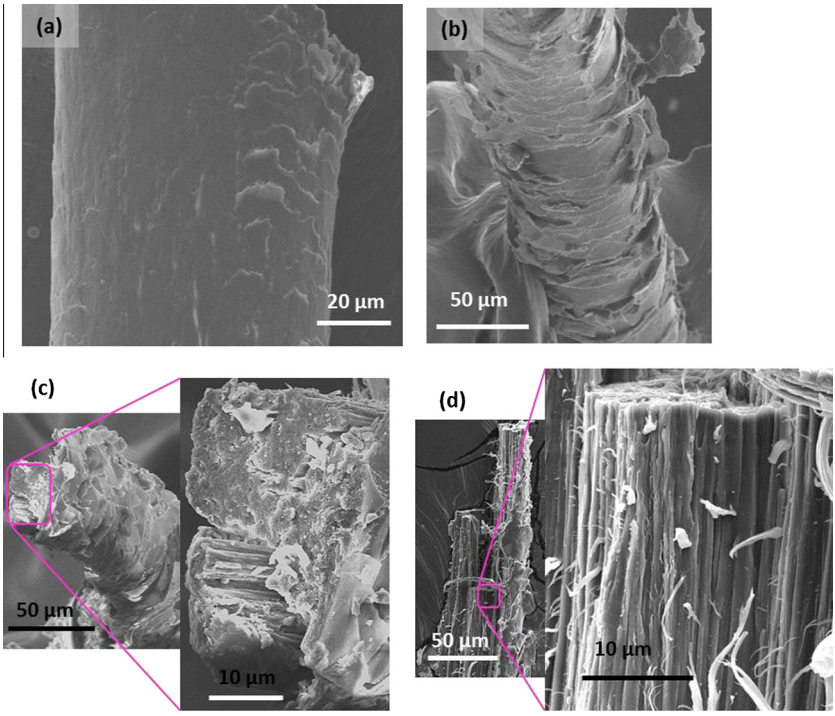

Fig. 25. Scanning electron micrographs showing the structure of human hair: (a) intact hair before stretch showing the overlapping cuticle cells on hair surface; (b) stretched hair (at strain rate of 10^0 s^{-1}) showing opened cuticle cells; (c) surface of tensile fractured hair; (d) side view of tensile fractured hair [175,155].

short (8–10 cm) without struts inside, with a closed-cell foam core. The cells in center are larger than those close to cortex. The surface of American porcupine quills has overlapping keratin scales that create a serrated structure, providing smooth insertion and making them difficult to pull out.

X-ray micro-diffraction of African porcupine quill shells revealed that the shells consist of three layers: a moderately ordered α-keratin in the outer layer, an amorphous and poorly ordered β-keratin layer and a highly ordered α-keratin in the inner layer [180]. Fig. 27 [181] shows the fractured surface of an American porcupine quill shell (loaded in circumferential direction). An outer layer with smooth fracture surface, a middle layer with the fibers aligned axially along the quill and a thin and somewhat indistinct inner layer can be observed. Quills (from North American porcupine) show a clear fine filament-matrix structure (Fig. 16c, [146]). The IFs, measuring about ~7 nm in diameter

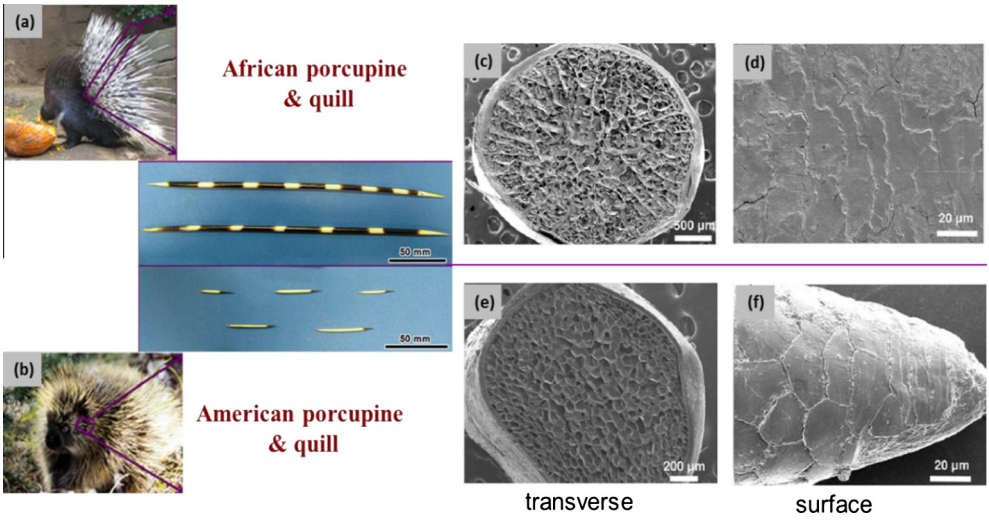

Fig. 26. Morphologies and structures of porcupines and their quills [179]: (a) African porcupine and the quills; (b) American porcupine and the quills. Scanning electron micrographs of African porcupine quills: (c) the transverse cross section with stiffeners to the cortex; (d) outside surface of the cortex; scanning electron micrographs of American porcupine quills: (e) the transverse cross section; (f) the surface of the quill tip, with overlapping and backward facing scales.

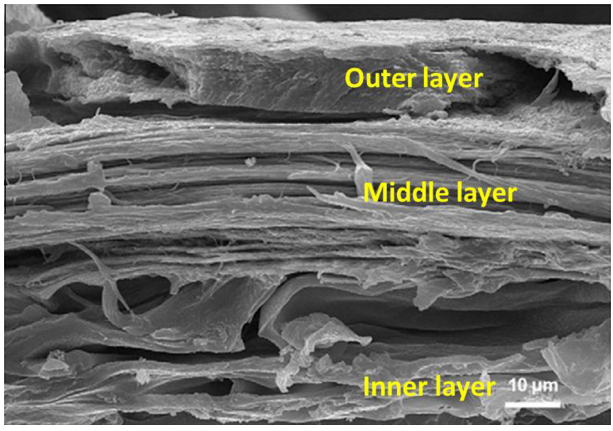

Fig. 27. Fracture surface of an American porcupine quill cortex after being loaded in the circumferential direction at 100% RH [181].

embedded in matrix, show different packing arrangements: near-hexagonal packing (lower left region in Fig. 16c) and layered arrangement (upper right region in Fig. 16c). The cortical cells are separated by cell membrane complex (about 25 nm thick) composed of a central dense layer and less dense regions on both sides of the central layer. The longitudinal sections of quill tips show somewhat longitudinal oriented IFs although no structural regularities along the IF axis have been resolved [146].

Fig. 28a shows the compressive stress–strain curves of African and American porcupine quills and cortex (foam removed) [139]. Whole quills exhibit higher compressive strength and toughness than the cortex alone, which indicates that the foam influences the local buckling behavior significantly (Fig. 28a). The critical buckling strength of a thin-walled cylindrical shell can be calculated from Eq. (9), assuming an isotropic material [182,183]:

$$\sigma_{cr} = \frac{E}{(a/t)\sqrt{3(1-\nu^2)}} \tag{9}$$

where t is the thickness of the cortex, ν is the Poisson's ratio (0.3), and a is obtained by subtracting half of the wall thickness from the outer radius of the cortex.

Using geometrical measurements, the buckling strength is predicted to be 83.9 MPa (E = 2.6 GPa) for African porcupine quill, a value much lower than the experimental one (135.2 MPa) which was attributed to the axial alignment of the keratin fibers (the predicted strengths were based on an iso-

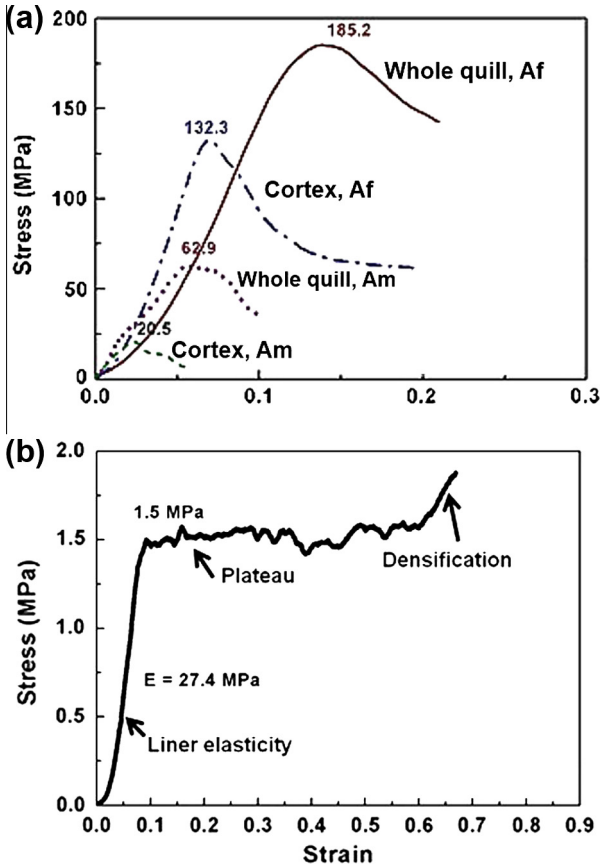

Fig. 28. Compressive behavior of porcupine quills [139]: (a) compressive stress–strain of whole quill and cortex of African (Af) and American (Am) porcupine quills; (b) compressive stress–strain of foam of African porcupine quill.

tropic material). The predicted buckling strength for American porcupine quill is 26.0 MPa (E = 1 GPa), which is comparable to measured value (20.5 MPa), indicating a more isotropic nature of the keratin filament orientation [139].

It is reported that the porcupine quill foam can undergo high tensile or compressive deformation to accommodate buckling of the cortex [179]. From the compressive stress–strain curve in Fig. 28b, the foam behaves as a classic polymeric solid: a linear elastic region and then a plateau region where the cell walls bend and deform, followed by an upturn in the curve where the cell walls collapse and the material densifies. Fig. 29 shows the morphologies of the compressed quills [139]. It can be seen that: (1) the foam firmly remains attached to the cortex, providing support to delay the onset of local plastic buckling of the cortex (Fig. 29b); (2) the buckling of the cortex is accompanied by tensile and compressive deformation of the foam. Around the buckled cortex regions, compressive deformation occurs, shown in Fig. 29b; in the central region, the foam is in transverse tension, and the arrow shows small tears in the foam walls caused by tensile stress (Fig. 29c). This may help release the strain energy stored in the cortex.

3.1.4. Horns

Horns are hard keratinous materials and appear on bovid animals including cattle, sheep, gazelles, and waterbuck. Horns function as a weapon to protect from predators, as a shield to catch blows, to combat with other males to win females for mating, and possibly regulate body temperature [151,184]. They are remarkably tough, resilient and highly resistant to impact forces, since they are usually subject to extreme loading impacts during life and will not grow back once broken [185,186]. Horns possess very high energy absorption before breaking [141]: the work of fracture of fresh waterbuck horns was found to range from 10 to 80 kJ/m^2 along the length of the horn; taking

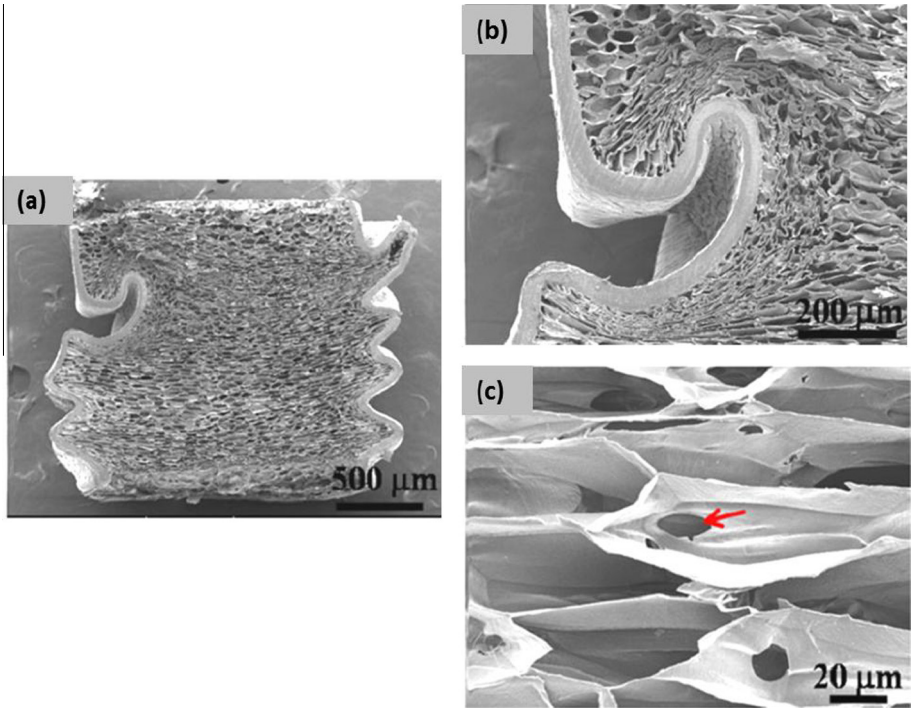

Fig. 29. Scanning electron micrographs of compressed American porcupine quill [139]: (a) morphology of the longitudinal cross section of compressed quill; (b) foam and cortex at the buckling part; (c) damaged foam, with a red arrow indicating a tear caused by compressive load.

into account specific gravity of different materials, the specific/relative work of fracture of horn keratin (32 kJ/m^2) is greater than most other biological and synthetic materials (antler 6.6 kJ/m^2, bovine femur 1.6 kJ/m^2, glass 5 kJ/m^2, mild steel >26 kJ/m^2) [187,188]. This excellent mechanical performance results from the complex hierarchical structure and the crack-stopping mechanisms. Fig. 30a [185] shows the morphology of a bighorn sheep horn. The horn has spiral ridges on the surface corresponding to seasonal growth spurts, and a hollow interior, which on the live animal encloses a porous bone. It is a three-dimensional laminated composite and has a gradient in porosity (elliptical dark tubules about 40–100 μm in diameter, Fig. 30b) along the horn transverse section. The hierarchical structure is shown in Fig. 30c: it consists of longitudinally aligned lamellae (parallel to tubule direction, 2–5 μm thick) which stack along the radial direction. The lamellae are composed of IFs embedded in an amorphous matrix. The fine filament-matrix structure of bovine horn under transmission electron microscope is shown in Fig. 16d [16].

Mechanical properties of horns are important in order to prevent breakage and absorb energy. Fig. 31a [189] shows that the tensile properties of bovine horn sheaths are highly hydration dependent: with increasing water content, both the Young's modulus and tensile strength decrease (from

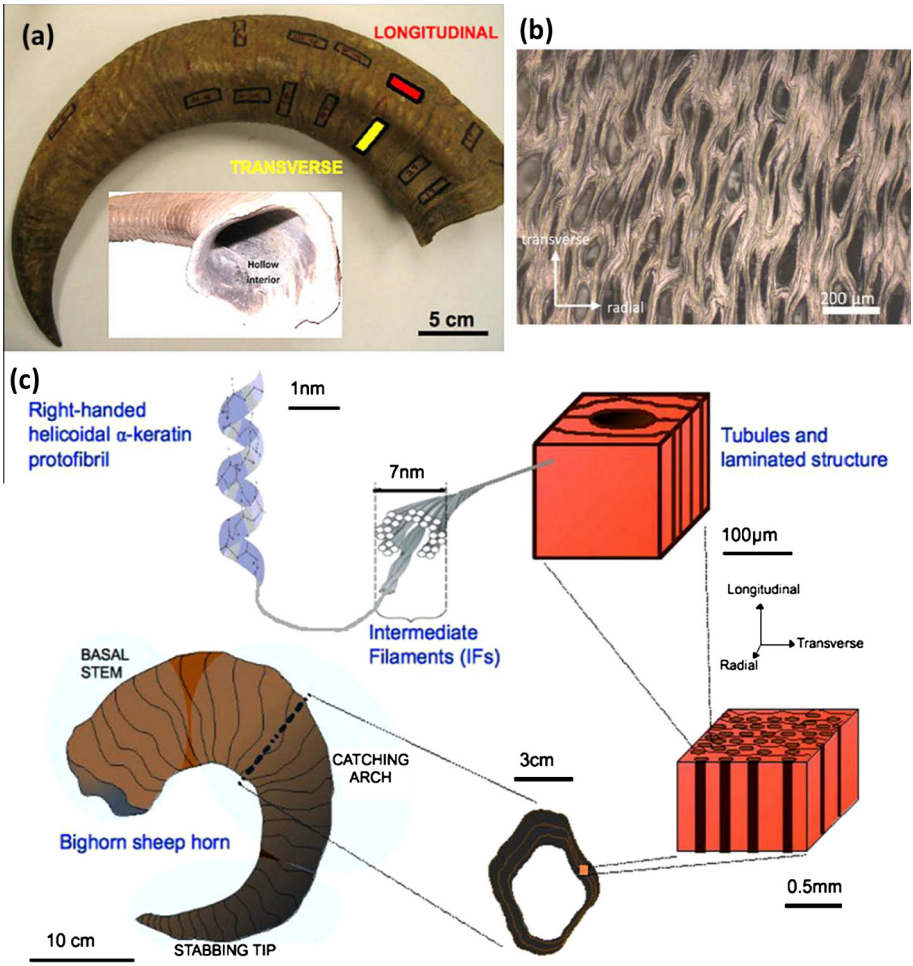

Fig. 30. (a) Photograph of the bighorn sheep horn showing the ridges on the surface and the hollow interior; (b) cross-sectional micrograph showing the tubules in the horn; (c) hierarchical structure of the horn [185].

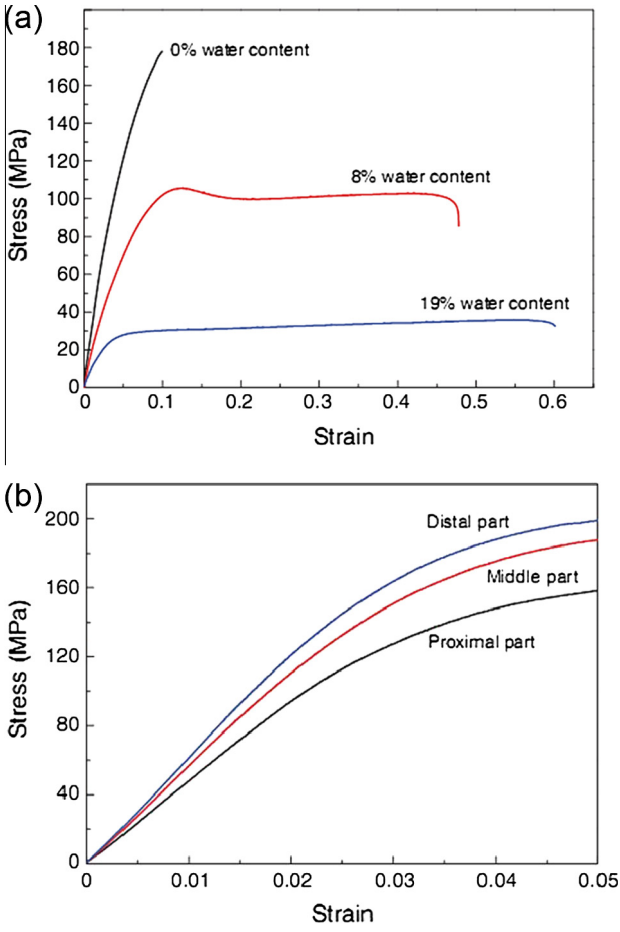

Fig. 31. (a) Tensile stress–strain curves of bovine horn sheaths at three hydration levels; (b) flexural stress–strain curves of samples obtained from different parts along the bovine horn sheath [189].

2.34 to 0.85 GPa and 154 to 39.7 MPa, respectively), but tensile strain increases. This dependence is similar to other horns studied. An earlier study reported that [190] the moisture in a sheep horn severely decreased its elastic modulus. The oryx horns showed that both the elastic and shear modulus decreased significantly with an increase in the moisture content [125]. The study used a modified Voigt model [191] based on a discontinuous fiber composite (Eqs. (10)–(13)):

$$E_c' = E_f V_f \left(1 - \frac{\tanh(\beta L)}{\beta L}\right) + E_m V_m \tag{10}$$

where the factor $\left(1 - \frac{\tanh(\beta L)}{\beta L}\right)$ was added. The parameters in Eq. (10) are:

$$E_m = 2(1+\nu)G_m \tag{11}$$

$$\beta = \left(\frac{2G_m}{E_f r^2 \ln(R/r)}\right)^{1/2} \tag{12}$$

$$\ln\frac{R}{r} = 0.5\ln\left(\frac{2\pi}{3^{1/2}V_f}\right) \tag{13}$$

where E_f and E_m are the Young's moduli of composite, fibers and matrix, respectively; V_f and V_m are the volume fractions of fibers and matrix, respectively; G_m is the matrix shear modulus; L, r and R are the half fiber length, fiber radius, and interfiber distance, respectively.

Kitchener and Vincent [125] compared the estimated bending stiffness values (E_c') at different humidity levels with experimental measurements. In the wet condition, v is 0.5 and G_m is tested as 0.3 GPa so E_m is 0.9 GPa by Eq. (10); E_f is 6.1 GPa the same as dry horn; V_f, V_m, r and L are 0.53, 0.47, 3.65 nm and 20 nm, respectively. Therefore, the calculated stiffness is 1.9 GPa which agrees with the experimental result, 1.8 GPa. This indicated that the modified model for horns is a reasonable assumption.

The hydration dependence is considered to be due to the water–matrix interaction, similar to that of wool which has been widely studied [17,105,111,122,164,192]. The explanations described previously (Section 2.4.4) can be applied to horns.

In Fig. 31b, flexure tests (three point bending) of the specimens from different positions in a bovine horn sheath show that the distal part has higher strength and stiffness than the middle and the proximal parts. The gradient in the stiffness and strength along the length of horn sheath is important for the cattle, since during defense, the distal part of a horn needs higher strength to stab the opponent; whereas the proximal part should be more flexible to absorb energy during fighting. The gradient of mechanical properties is due to the different water contents and keratinization degrees in the proximal, middle and distal parts [189]. Tombolato et al. [185] observed a gradient in the amount of porosity across a bighorn sheep horn, which would also contribute to differences in strength.

The relationship of hydration and work of fracture can also explain the horning behavior of bovids [141]. The horn keratin has the highest work of fracture (41.63 ± 1.69 MJ m^{-3}) at 8% water content [189], similar to other studies that horn sheaths of gemsbok, mouflon and waterbuck show maximum toughness when they are in the fresh state [141]. This explains why the bovid animals dip their horns into mud or plants to avoid the over dehydration and to ensure optimized mechanical properties.

Fig. 32 [189] shows the morphologies of the fracture surfaces after tensile testing the bovine horn sheath. The laminate structure is clear, and each layer has a rippled appearance (Fig. 32a). The flattened keratinized cells have a labyrinth-like surface morphology and are laminated together (Fig. 32b). This lamellar structure exhibited by the flattened, curved dead keratin-filled epithelial cells is somewhat similar to that of the mouflon fractured horn sheath [142]. This microstructure leads to an enhanced toughening effect on the fracture resistance, since [189]: (1) the wavy interface between the cells may help resist crack nucleation and propagation; (2) the labyrinth-like surface of the flat-

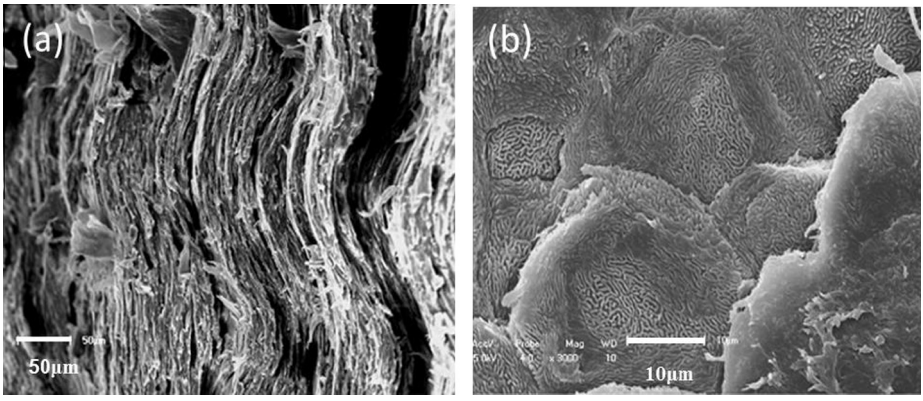

Fig. 32. Scanning electron micrographs of the tensile fracture surface of bovine horn sheath: (a) the layered structure of tabular cells; (b) flattened keratinized cells in layers with a surface mesh morphology [189].

tened cells may enhance the friction between lamina and thus help to pin the neighboring lamina; (3) the lamellar structure may help maintain an appropriate hydration level that may be essential for optimum toughness, which is similar to findings of previous studies on the horn sheaths of gemsbok, mouflon and waterbuck that the maximum toughness was in the fresh state [142].

3.1.5. Hooves

Hooves are hard keratinous materials, and have been the focus of a number of studies. The hoof wall copes with a diversity of high ground-reaction forces and transfers these to the bony skeleton, and any damages remain in the hoof until that part is worn off. Therefore, the hoof wall must be capable to withstand repeated high stresses, and studies show that the stratum medium (the central epidermal layer) of hoof wall is one of the most fracture-resistant biological materials known [193].

The hoof wall has been considered as a multi-level hierarchical composite, shown in Fig. 33a [114]. It is composed of flattened, keratinized cells that are organized into 200–300 μm diameter tubules (along the hoof length) with medullary or hollow cavities (~50 μm) and intertubular materials that lie at large angles relative to the long axis of tubules, forming a macroscale composite [193–196]. In addition, hooves are formed from α-keratin that has been considered as fiber-reinforced composite at nanoscale. Fig. 33b shows a circularly polarized light micrograph of the cross section of a tubule (areas a, b and c) and associated tubule material at outer hoof wall region overlaid with cell boundaries [193]. Medullary cavities appear dark in the centers of tubules. Cells of the tubule cortex are organized into concentrically arranged lamellae, where each lamella is composed of a single layer of cells.

The packing arrangement of IFs along the hoof wall thickness has been studied via polarized light microscopy [193]. From Fig. 34 [114], at the inner wall, the intertubular material shows that most of

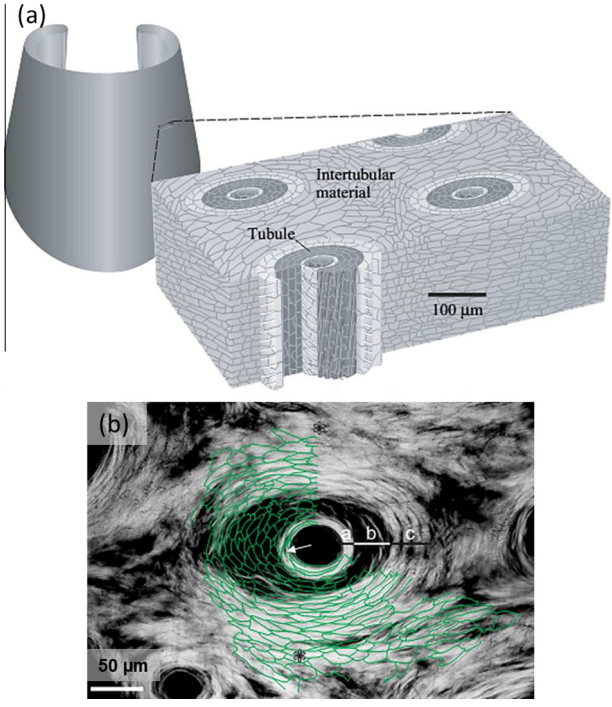

Fig. 33. (a) Schematic drawing of the equine hoof wall showing cells organized into tubules and intertubular materials [114]. (b) Circularly polarized light micrograph of cross section of a tubule and intertubular material from equine hoof wall. Green curves overlaid are cell boundaries from the section under non-polarized light. The lightest areas show molecules close to the plane of section while darker areas show molecules oriented perpendicular to the plane of section. Tubule cortical lamellae types are indicated as a, b and c [193].

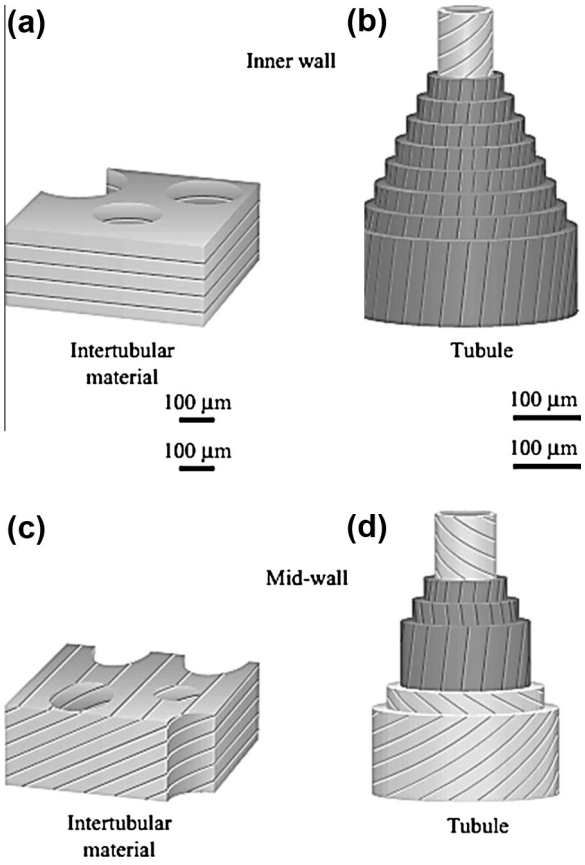

Fig. 34. Schematic illustrations of the packing orientations of IFs in both intertubular material and tubule at different locations of equine hoof wall. At inner wall: IFs plane in (a) intertubular material and (b) tubule; at middle wall: IFs plane in (c) intertubular material and (d) tubule [114].

the IFs are aligned nearly perpendicular to the tubule axis (Fig. 34a), while the tubules show inner type lamellae that have cross-helical IF orientation (helical angles 40–60°) and lamellae (surrounding the inner type) that are wound in register in right-handed helical (helical angles 0–12°) (Fig. 34b). At the middle wall, the intertubular material shows IFs arranged in planes in an acute angle (Fig. 34c), while the tubules show three types of lamellae: inner, middle and outer. The inner lamellae are similar to those in the inner wall, the middle lamellae cross between adjacent lamellae (0–33°) and the outer lamellae show crossed helices from adjacent lamellae (helical angles 50–60°). By taking advantage of varying tubule and intertubular material organizations and altering the orientations and volume fractions of IFs along the hoof wall thickness, the substructures are able to provide high fracture toughness and control crack growth. The structural complexity enables the hoof wall to absorb much energy as the crack grows (by separating the two phases of the composite [197]), occurring at the level of the IFs and matrix of keratin, at cell boundaries within the hoof wall, and at the level of the tubular and intertubular components [123,196].

The mechanical properties of hoof wall are modulated through hydration gradient and a complex structure design [123,193]. There are two hydration gradients within the hoof: a horizontal one where the outer surfaces of the hoof have low hydration levels and the interior, adjacent to the dermis, maintains a high hydration level, and a vertical gradient, hydration decreasing from the germinative region to the distal contact surface. Longitudinal tensile results on the central epidermal layer (stratum med-

Table 9
Mechanical properties of equine and bovine hoof walls.

Equine hoof [123]	Young's modulus (GPa)	Yield stress (MPa)	Fracture toughness (kJ/m^2)	Relative humidity (RH) (%)
	0.41	9.18	11.9	100
	2.63	38.9	22.8	75
	3.36	–	5.6	53
	14.6	–	6.7	0

ium) of horse hoof wall specimens at various hydration levels (Table 9) show that the Young's modulus increases significantly with decreasing hydration: 0.41 GPa at 100% RH to 14.6 GPa at 0% RH. The stress–strain curves indicate a general increase in modulus and a decrease in maximum strain with decreasing hydration. The hydration effect was attributed to water more strongly influencing the properties of the matrix phase than the IFs, similar to wool [123].

Fracture tests (Table 9; pre-notch along the tubule direction) showed that the fracture toughness reaches a maximum at 75% RH (22.8 kJ/m^2), which is an order of magnitude higher than that measured for fresh bone (1.0–3.0 kJ/m^2, [198]). This indicates that the hoof wall keratin is remarkably fracture-resistant. In many materials a decrease in hydration can adversely affect the notch sensitivity and fracture properties, making them brittle. At very high hydration levels the load carrying capacity is severely decreased due to the lowering of the yield stress. It was reported that the hoof wall midway possesses water contents 17–24% by mass [199], which is the in the same range for the 75% RH [123], indicating that the hoof wall keratin appears to function *in vivo* at the hydration state closely matching the optimum condition for fracture toughness.

The observation of the fracture surface at different locations and orientations reveals the crack diversion mechanisms preventing cracks from reaching the living tissue of hoof [193]. The tubules reinforce the hoof wall against fracture inward to inner tissue, and cracks along the tubule direction would be diverted by intertubular material to external surface. Fig. 35 shows schematic illustrations and scanning electron micrographs of the crack paths and fracture surfaces of specimens (compact tension) at inner, middle and outer regions in stratum medium and along different orientations. Along the hoof wall thickness direction with notches parallel to the tubule axis (white areas in Fig. 35b), crack paths in the inner region tend to bifurcate to two directions (along the tubule axis and along the intertubular IF plane). In the middle region (where the dominant component is intertubular material) advancing cracks clearly deviate toward the circumferential direction following the intertubular IF plane (fracture surface shows the cross section of the tubule material, Fig. 35b middle with the schematic and scanning electron micrograph), while at the outer region cracks propagate along the tubule axis. Fig. 35c shows that in the middle region, cracks in specimens with upward notches (along the tubule axis) are redirected to external surface along the intertubular IF plane, and in specimens notched inwards (perpendicular to the tubule axis) the cracks deviate downwards, following the intertubular IF plane. In Fig. 35d, the crack path in specimens notched inwards (transverse to the tubule axis) is also redirected to along the intertubular IF plane. It was concluded that the mid-wall diversion mechanism of intertubular material inhibits inward and upward crack propagation, and that the inner- and outer-wall diversion mechanisms prevent inward crack propagation [193,196].

Hooves undergo constant impact with the hard soil whereas horns impact during combat. Although these velocities are not very high, less than 10 m/s, they nevertheless generate stress waves traveling through the material, which should be attenuated in order not to damage the underlying live tissues, primarily the bone. Thus, mechanisms to dampen the propagation of stress waves operate. The following are proposed to be the principal ones: (a) decay of wave produced by viscoelastic response of keratin; (b) scattering of wave by cylindrical tubules and internal interfaces.

3.1.6. Nails

Nails, covering the ends of fingers and toes in primates and a few mammals, and curved claws from mammals (e.g. cat) show an α-type X-ray diffraction pattern [29]; both are grouped as Nails in this section. Nails serve as a stiff backing to the soft terminal pads, preventing the skin from rolling back-

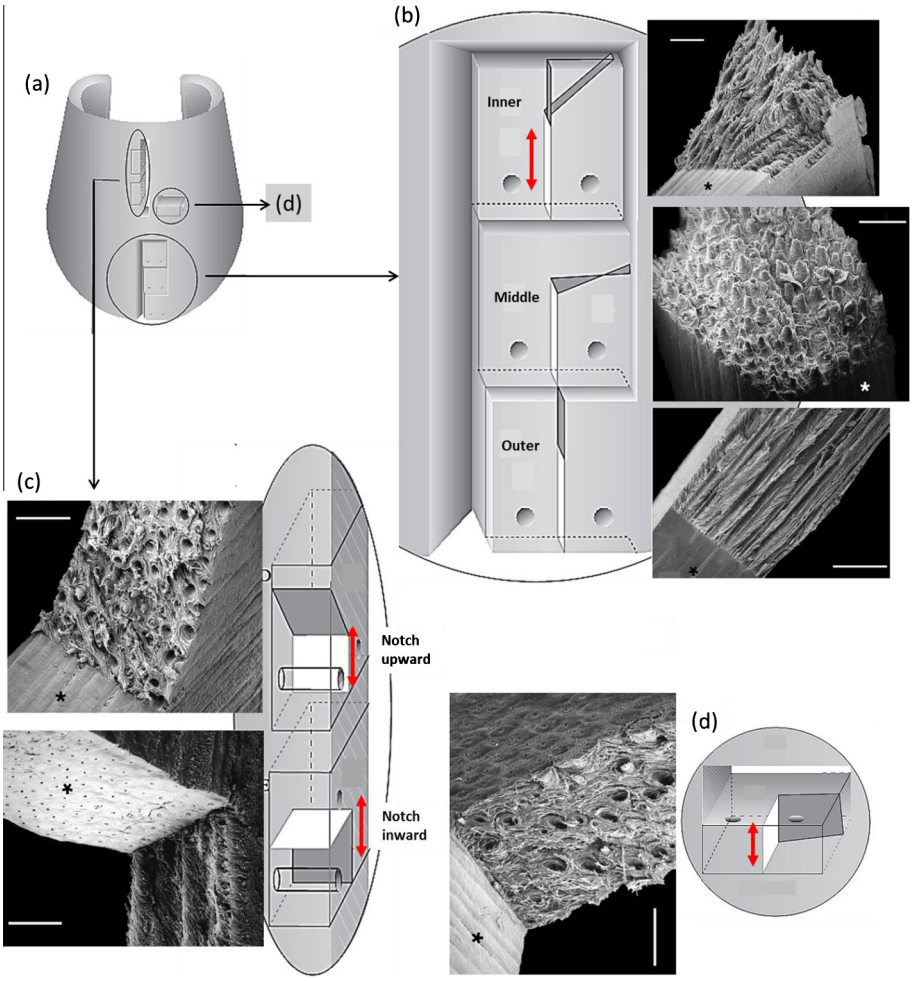

Fig. 35. Schematic summarizing the crack diversion mechanisms (white areas indicate notch surfaces, and dark gray areas fracture surfaces) and scanning electron micrographs of the fracture surfaces (compact tension) of equine hoof wall (notch surfaces appear smooth, marked with asterisks; scale bars, all 1 mm). Red double-head arrows indicate the tubule direction. (a) The hoof wall and specimens in three groups: at different regions along the thickness direction, at middle region with notches parallel and perpendicular to tubules, and at middle region with notches trans-passing tubule axis. (b) Specimens at inner, middle and outer regions of the hoof wall with notches upward parallel to tubule axis and the crack paths, and the corresponding fracture surfaces. (c) Specimens at middle region with notches upward (parallel to tubule axis) and inward (perpendicular to tubule axis) and the crack paths, and the corresponding fracture surfaces. (d) Specimens at middle region with notch inward (trans-passing tubule axis) and the crack path, and the fracture surface [193].

wards over the distal phalanx [140]. Fingernails are one characteristic feature of primates [200]; they are used to lever up objects, open cracks, scratch and fight, during which the loadings are usually from below and cause upward bending forces. The structure of human nails is composed of three histological layers which are deposited by the nail matrix at the nail base [201–203]. Along the transverse cross section (Fig. 36a) of fingernails, the layers resemble a sandwich structure (shown in Fig. 36b): a dorsal layer making up about a quarter of the nail thickness, an intermediate (or middle) layer composing approximately two-thirds of the nail thickness, and a thin ventral layer. The keratin fibers in the intermediate layer (Fig. 36c) are transversely oriented (parallel to the free edge of the nail) while those in the ventral and dorsal layers may not show preferred orientation [204,205] or crossing fibers

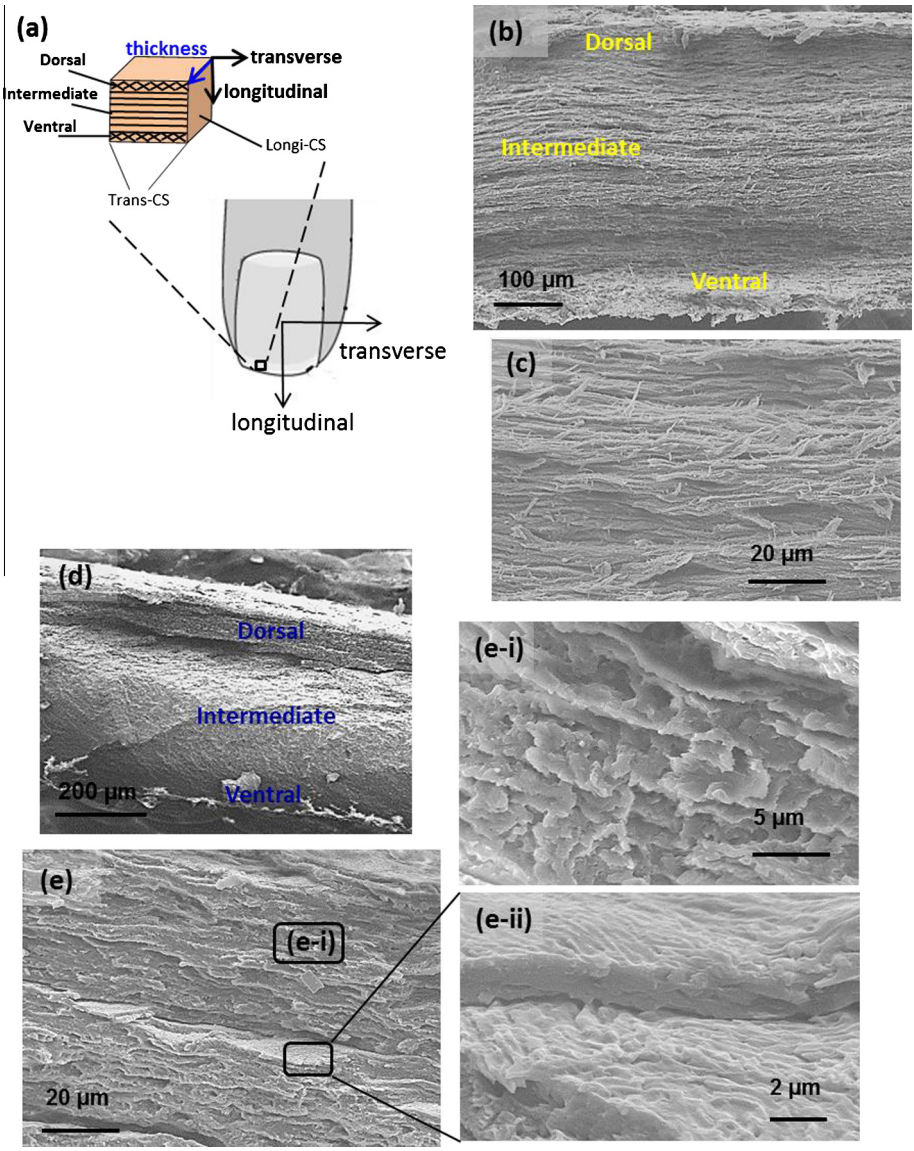

Fig. 36. (a) Schematic drawing of a fingernail and the three-layered structure with fiber orientations on the transverse cross section (Trans-CS). The longitudinal (along finger axis) and transverse (along fingernail edge) directions are indicated. Scanning electron micrographs of transversely torn fingernail: (b) Trans-CS with dorsal, intermediate and ventral layers indicated; (c) thick intermediate layer showing clearly the transversely oriented fibers. Scanning electron micrographs of the longitudinally freeze-fractured fingernail: (d) longitudinal cross section with dorsal, intermediate and ventral layers indicated; (e) dorsal layer showing clearly the lamellae formed by tiled keratinized cells; (e-i) crossing lamellae (about 2–4 μm in width); (e-ii) keratinized cells with surface sutures forming the interlocking bonds.

[155]. This is why nails often crack parallel to the free edge of the nail and the fracture does not penetrate into the live tissues.

Each of the three layers in the nail plate consists of closely bonded but poorly defined lamellae. Each lamella is composed of one or more layers of flattened epithelial cells [206]. Fig. 36d and e shows

the lamellar structure of the longitudinal cross section from freeze-fractured fingernail. The dorsal layer exhibits lamellae parallel to nail surface (Fig. 36e); each lamella is about 2–4 μm in width (Fig. 36e-i) and is composed by one layer of keratinized cells (Fig. 36e-ii). The cells show surface sutures that interlock keratinized cells, thus increasing bonding and the material strength. The intermediate layer shows relatively smooth morphology, which may be due to the fractured surface of the lamellae, and the tilted arrangement may be a result of the orientation parallel to the lunula (the half-moon area). Interestingly, the ventral layer consistently shows similar structure as the dorsal layer. The lamellar structure may also be interpreted as layered structure with different orders, shown in Fig. 37: a 1st order for the dorsal, intermediate and ventral layers, a 2nd order for the layered structures in each 1st order layer (in dorsal and ventral layers the 2nd order layers are parallel to nail surface about ~2 μm thick, while in intermediate layer the 2nd order layers show step-like morphology), and a 3rd order for the sheet structures in nanoscale in each 2nd order layers. Fig. 16e shows the IF-matrix structure of a human fingernail, in which the IFs exhibit different packing orientations, indicated by either the transverse or longitudinal sectional profiles.

Among the first studies of the mechanical properties of fingernails, Baden [204] reported elastic modulus values from experimental cut tests and by measuring the velocity of sound in nail plate (~2–4.3 GPa); Ramrakhiani [207] showed that spherical indents on the nail surface recovered over a period of time. Tensile testing on fingernails along the axis of fibers in intermediate layer yielded a strength of 86 MPa under ambient environment. Humidity has a profound effect on the mechanical behavior of fingernails: when hydrated (100% relative humidity), the tensile strength decreases from 85.6 to about 22.5 MPa, and the Young's modulus decreases from 2.05 to 0.19 GPa (Fig. 38). Table 10 shows the Young's and shear moduli of fingernails at different hydration levels [208]. It is clear that increasing the relative humidity significantly lowers both moduli, but the decrease of the shear modulus is greater than that of the Young's modulus, indicating that the water plasticizes the matrix rather than affecting the keratin fibers, similar to wool. The ratio of Young's modulus over shear modulus is minimized at 55% RH, close to the natural nail hydration conditions. This suggests that the resistance to torsion and bending forces may be balanced at this point.

Scissor cutting tests on fingernails at different layers and different orientations are reported to investigate how the structure design resists bending forces and prevent crack propagation [140]. This

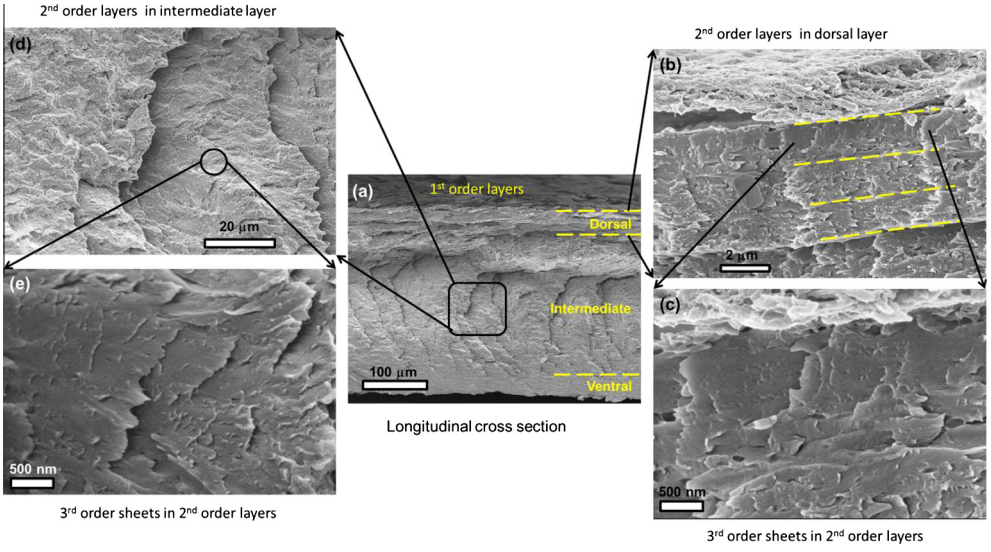

Fig. 37. Scanning electron micrographs of freeze-fractured fingernails showing the layered structures at different levels: (a) dorsal, intermediate and ventral layers as 1st order; (b) layered structures as 2nd order in dorsal layer; (c) sheet structure as 3rd order in dorsal layer; (d) layered structure in intermediate layer; (e) sheet structure as 3rd order in intermediate layer (Figure courtesy from Dr. W. Yang).

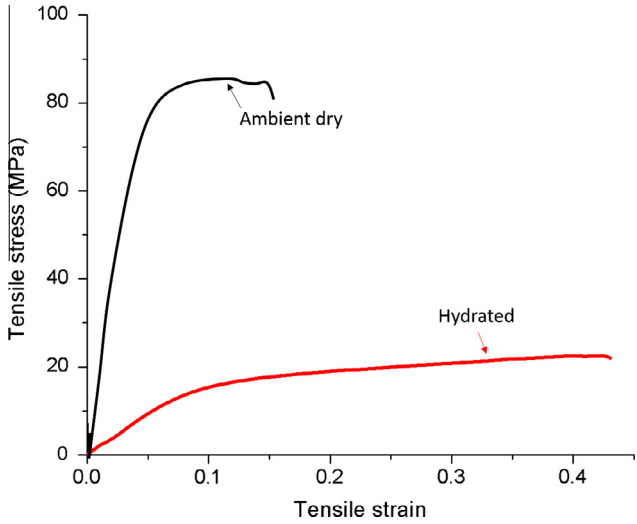

Fig. 38. Tensile stress–strain curves of human fingernails at ambient dry and hydrated conditions (room temperature).

is not a perfect fracture toughness test, but is all that is available in the literature. The energy required to cut the nail longitudinally (approximately 6 kJ/m^2) is about twice the transverse energy (Fig. 39a) due to the laterally oriented fibers in the thick intermediate layer. As mentioned earlier, this prevents the crack propagating longitudinally to the lunula and deflects it away from the nail bed, allowing for self-trimming. The energy to cut the intermediate layer transversely is about a quarter of that to cut it longitudinally, indicating a significant mechanical anisotropy (Fig. 39b). The dorsal and ventral layers show similar energy values needed to cut through, creating an isotropic behavior, which can act to prevent the cracks forming at edge.

3.1.7. Whale baleen

Baleen is the filter-feeding apparatus inside the mouth of baleen whales, and consists of an assembly of keratinous plates which are tapered along the lingual edge into bristles (baleen hair), resembling a comb, seen in Fig. 40a [209]. The whale baleen, often called whalebone, has been a substitute for ivory in carving, collar stays and toys due to its elegant appearance. An interesting feature is that baleen has been a popular material used in the manufacture of corsets, which fashionable ladies wore to compress their waistlines from the 11th to the late 19th centuries.

Although little is known about the properties of whale baleen, it represents the most highly calcified keratinous material, e.g. the sei whale baleen has calcium content of 41 mg/g while that of wool is 2.8 mg/g [14]. For instance, the sei whale baleen contains 14.5% hydroxyapatite (dry weight) [104,210]. The baleen plates are composed of keratin cells organized into tubules and intertubular material (similar to horns and hooves), and Fig. 40b shows clearly the flattened cells arranged circum-

Table 10
Mechanical properties of human fingernails at different relative humidity levels [208].

Relative humidity (%)	Tensile modulus (GPa)	Shear modulus (GPa)
100	0.47	0.02
65	2.22	0.22
55	2.32	0.29
33	2.70	0.30
0	4.34	0.32

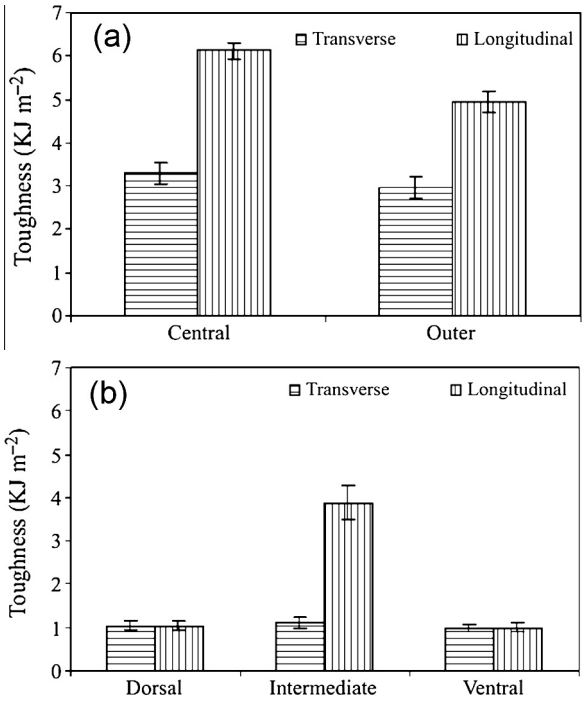

Fig. 39. The energy needed (toughness, kJ/m^2) for cutting human fingernails transversely and longitudinally: (a) cutting tests on whole nails with central and outer sections; (b) cutting tests on dorsal, intermediate and ventral layers [140].

ferentially around the tubule axis and in layers in the intertubular region [211]. The hierarchical structure of humpback whale baleen is shown in Fig. 40c [14], from the level of whole baleen down to the level of tubule and intertubular regions, and then to nanoscale of the IFs, calcium salt crystallites and matrix proteins. A feature distinct from other keratinous materials is that the calcium salt crystallites are deposited between IFs. This increases the stiffness and strength of the baleen to compensate for the special circumstance of baleens that they never have the opportunity for air-drying, a primary strengthening mechanism for most keratinous materials that increases their strength [14].

Tensile tests on different baleen bristles and wool reveal that calcification indeed contributes to the stiffening of the baleen [14]. Fig. 41a shows the stress–strain curves of baleen bristles from sei, humpback, minke whales and wool. It is clear that humpback and sei baleens show similar Young's modulus (about 1.2 GPa), which is comparable to wool fibers (1.21 GPa). Minke baleen has a lower value (0.65 GPa), whereas wool exhibits significantly higher yield and breaking stresses than the three baleen bristles. The sei and humpback baleens contain higher calcium salt concentrations than the minke, which may account for the higher Young's modulus and yield strength. The wool fibers naturally have a low amount of calcium, indicating that they may not be obviously mechanically influenced by changing the calcium content. Fig. 41b–e shows the tensile stress–strain curves of natural and decalcified wool fibers and the three baleen bristles. It can be seen that decalcification results in the greatest decrease in Young's modulus for sei (46%) and humpback baleens (20%), and little effect on the minke baleen (2% decrease). Decalcification causes no effect on the yield strain of the baleen bristles, and has little effect on the tensile properties of wool fibers (a slight increase in Young's modulus and no change in yield stress). The decrease in mechanical properties caused by removal of calcium in sei and humpback baleens demonstrates that the calcification boosts the stiffness and yield stress of baleen keratins, a stiffening mechanism developed by baleen whales to strengthen the material in the impossibility of controlling the moisture content.

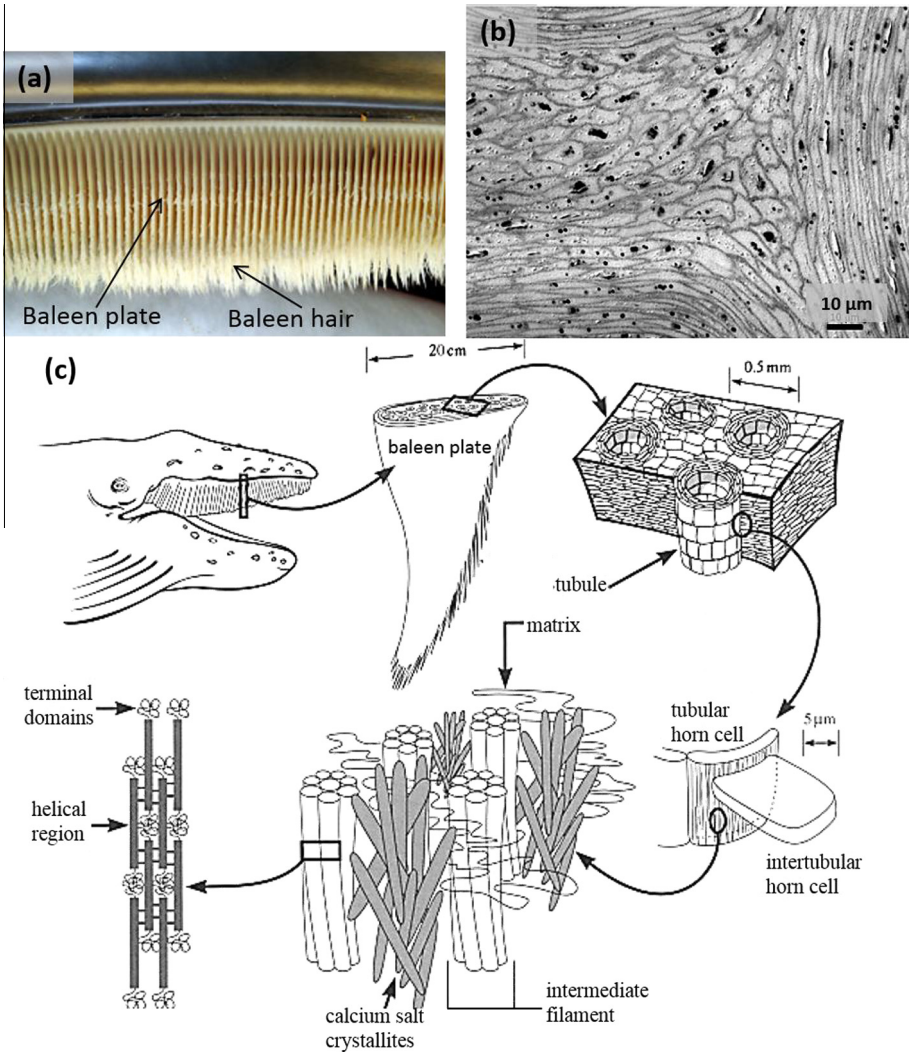

Fig. 40. Whale baleen and its hierarchical structure: (a) racks of baleen plates emerging from the upper jaw of the whale taper into a fringe of bristles, acting as a sieve for filtration of prey [209]; (b) hematoxylin and eosin stained sections from sei baleen, showing clearly the tubular flattened keratin cells arranged circumferentially around the tubule axis and in layers in intertubular region [211]; (c) hierarchical structure of humpback whale baleen [14].

3.1.8. Hagfish slime threads

Hagfishes are living fossils since there has been little evolutionary change in some of them over the last 300 million years [212]. Shown in Fig. 42a [213], they live on the bottom of deep waters and have an eel-shaped body without fish scales. They have a very special and complex jawless feeding apparatus, and the two pairs of keratinous teeth are anchored to dental plates, a bilaterally folding, paired series of cartilages, seen in Fig. 42b [214]. The most startling feature is that the hagfishes, when threatened or provoked, are able to excrete surprising quantities of slime which has keratin IFs bundles (slime threads) in a woven structure holding the slime (indicated by the arrow in Fig. 42c, [215]). The unique defense mechanism lies in that the slime contains mucins (proteins with the ability to form gels) bonded together with keratin threads, which can expand once contact with seawater to become almost three orders of magnitude more dilute than typical mucous secretion, and effectively

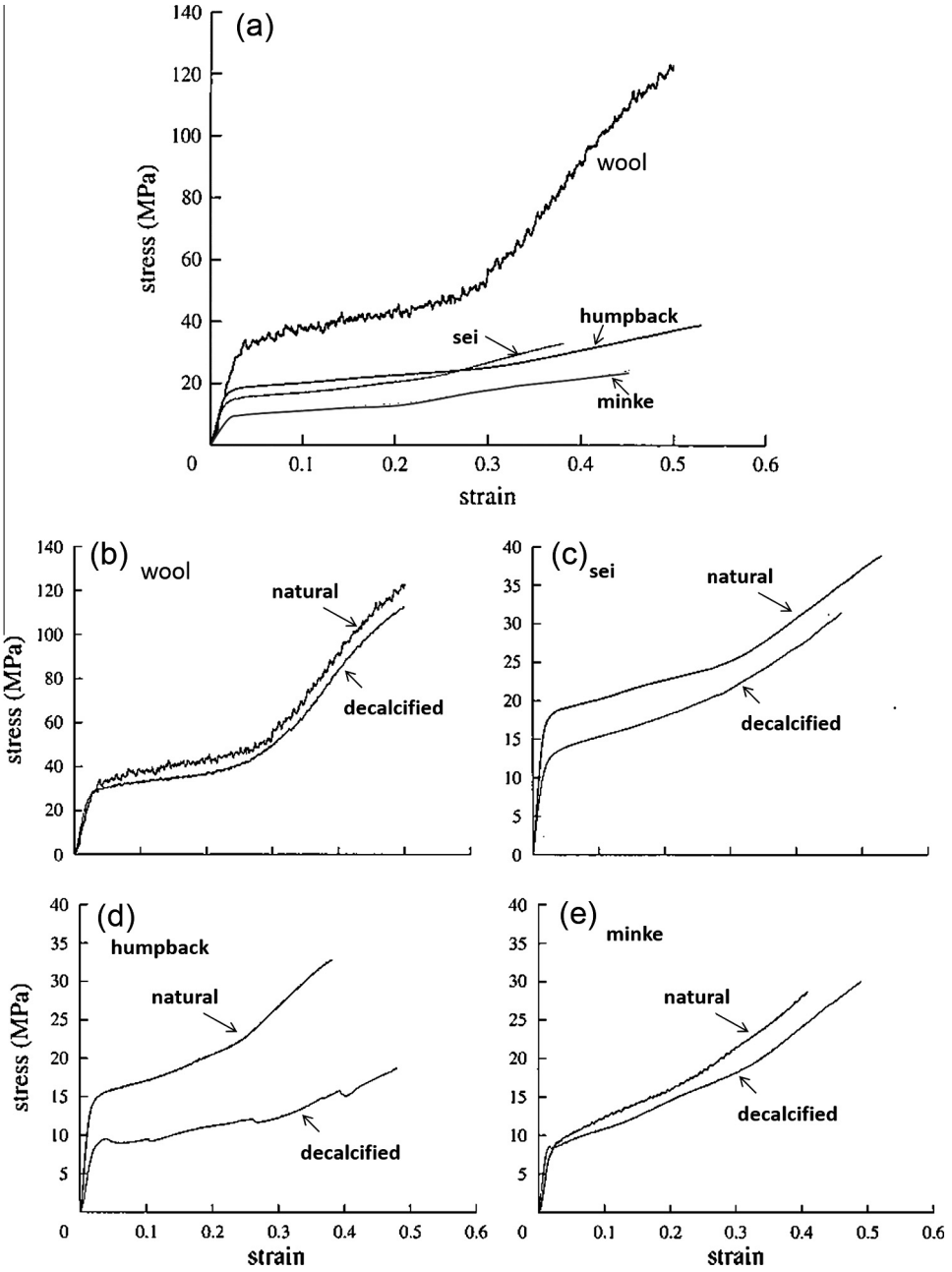

Fig. 41. Tensile stress–strain curves of: (a) whale baleen bristles from sei, humpback and minke whales in comparison with wool fibers (all in hydrated condition), (b) natural and decalcified wool fibers, (c) natural and decalcified sei baleen bristles, (d) natural and decalcified humpback baleen bristles, and (e) natural and decalcified minke baleen bristles [14].

chokes the predators with this gill-clogging slime [214], shown in Fig. 42d and e. A hagfish (*Eptatretus cirrhatus*) immediately produces a large amount of slime into the mouth of a shark as the shark is trying to eat it; thus, not being able to remove the slime, the shark has to release the hagfish.

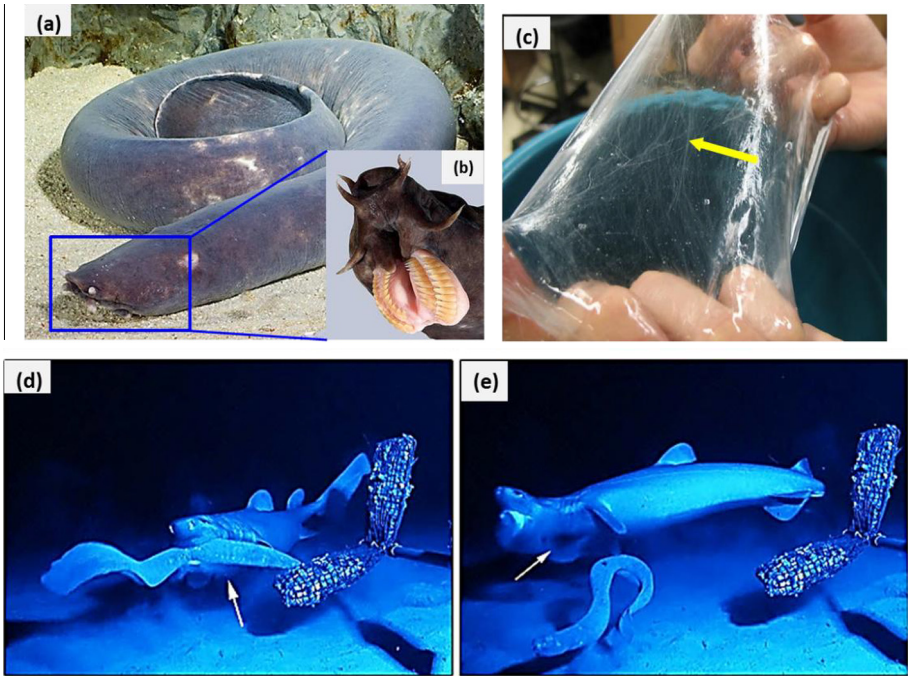

Fig. 42. (a) A Broadgilled hagfish (*Eptatretus cirrhatus*) resting in a spiral shape [213]. (b) Head of the Broadgilled hagfish with keratinous teeth on dental plate [214]; (c) hagfish slime and the slime threads, showing a chaotic woven structure that holds the sheets of slime together (indicated by a yellow arrow) [215]; hagfish slime function as a defense against gill-breathing predator: (d) a seal shark (*Dalatias licha*) is trying to bite and swallow the hagfish (*Eptatretus cirrhatus*), but the hagfish projects jets of slime (arrows) into the predator's mouth. The slime secretion took less than 0.4 s. (e) Choked, the predator releases the hagfishes and gags in an attempt to remove slime from its mouth and gill chamber [214].

It is reported that the hagfish slime is formed as the slime glands eject a two-component exudate comprised of coiled threads (also called 'skeins', coiled bundles of keratin IFs) and mucin vesicles into seawater (indicated by arrow and arrowheads in Fig. 43a, respectively) [216]. The rapid deployment of hagfish slime upon secretion involves hydrodynamic forces and the presence of mucin vesicles assisting the unraveling of skeins into long threads (seen in Fig. 43b). The process has been studied and proposed as consisting of the following steps [124,216]:

- slime exudate is expulsed into convectively mixing seawater;
- the swelling and elongation of mucin vesicles form mucin strands;
- these mucin strands attach to the thread skeins and transmit the hydrodynamic forces to the thread skeins, thereby initiating unraveling;
- entanglement of the threads and mucin strands results in the complete unraveling of thread skeins, forming the whole slime that is a highly complex network of mucin strands (0.0015%), slime threads (0.002%) and seawater (99.996%).

Fig. 43c and d depicts the threads (arrow) and mucin strands (arrowhead) in whole hagfish slime. All of these are in contrast to most IFs which function intracellularly. The IF-rich threads by the hagfish gland thread cells are released extracellularly to interact with mucins and seawater, modifying the viscoelastic properties of the mucous exudate [217].

Hagfish slime threads have been considered as a matrix-free keratin IFs model since they consist of tightly packed and aligned IFs [112]. Mechanical tests on slime threads under different conditions (see stress–strain curves in Fig. 44) show that threads in seawater exhibit a low initial stiffness (6 MPa),

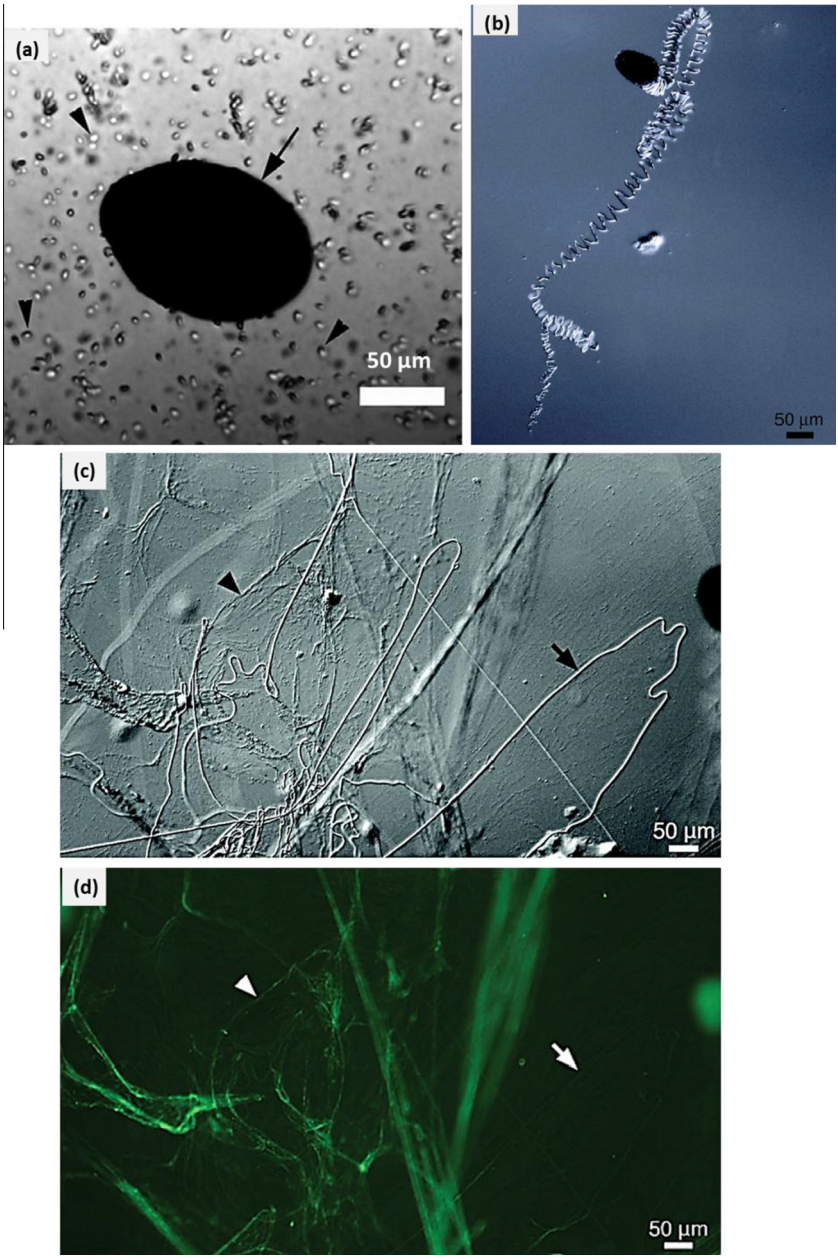

Fig. 43. Structural characterization of the hagfish slime threads (bundles of keratin IFs): (a) a concentrated exudate (forming the slime) released by the slime glands; it contains both coiled slime threads (skeins) (arrow) and mucin vesicles (arrowheads) that rupture in seawater [216]; (b) differential interference contrast (DIC) image of partially unraveled thread skein in seawater illustrating their coiled structure [124]; (c) DIC image of the whole slime network depicting unraveled threads (arrow) and mucin strands (arrowhead) connecting threads; (d) fluorescence image of the same area in (c) highlighting the mucin network (arrowhead) [124].

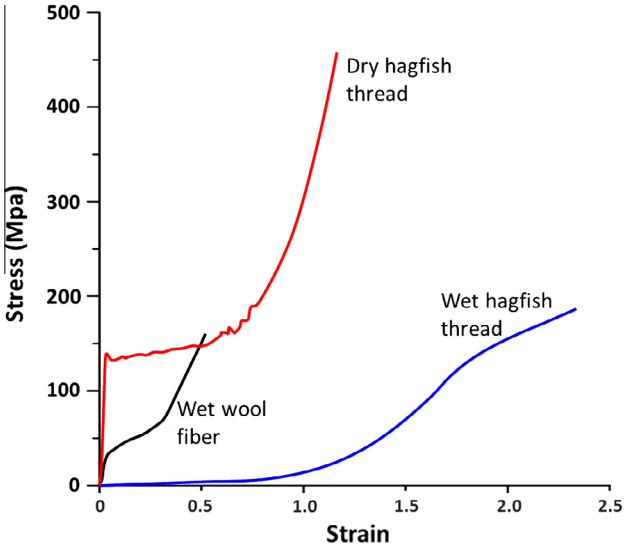

Fig. 44. Tensile stress–strain curves of hagfish threads in seawater (blue), wet wool fibers (black) and a hagfish thread tested in air (red) (reproduced from [115]).

high tensile strength (180 MPa) and a large extensibility, up to strain of 2.2 which is attributed to the soft elastomeric terminal domains of IFs [112]. In comparison, the dry threads show a high initial stiffness of 3.6 GPa, which is about 600 times the one for hydrated threads, and a high tensile stress of 530 MPa and maximum strain of 1.0. The dramatic mechanical difference between hydrated and dry threads indicates that matrix-free IFs are remarkably hydration sensitive [115]. Note that this is not contrary to the accepted view that in hydrated hard α-keratinous materials the matrix proteins interact with water molecules more than IFs, since the threads consists of only IFs but no matrix. It should also be mentioned that the strength of dry slime threads reaches 560 MPa, the highest value reported for any keratin. This may be due to the absence of the amorphous matrix and to a scale effect, the cross sectional dimension being very small (~4.5 μm).

It is interesting that compared with the significant hydration sensitivity of hagfish slime threads, hard α-keratinous materials are much less dependent on hydration (initial tensile modulus drops by a factor of 2.7 after hydrated [115,218]. This indicates that the matrix helps the IFs to resist swelling and maintain high stiffness and strength [124]. In addition, the mechanical properties of dry threads are comparable to those of hydrated hard α-keratinous materials, e.g. wool (Fig. 42), suggesting that IFs in hydrated wool are maintained in a partly dry state [115]. This is supported by the fact that hard α-keratins do not swell nearly as much as slime threads when placed in water. It is also possible that the amorphous phase blocks the direct access of water to the IFs, and this hydration is decreased. The inhibition of swelling is also a possible factor.

Mechanical studies on mucins and whole slime reveal that the slime threads provide elasticity and dominate the slime's mechanical properties, while the mucins impart additional viscosity and assist in the rapid deployment of the slime into the mature state. Measurement of mucin mechanics demonstrates that the mucins are not capable of providing shear linkage between adjacent slime threads, indicating that the hagfish slime cannot be considered as a fiber-reinforced composite. This is not necessary since the threads have enough length to span the entire slime network [216].

3.1.9. Whelk egg capsules

Whelks are various sea snails (marine gastropods), and the flesh has been used for food by humans and other animals. An interesting feature of this organism is that after fertilization, the female whelk lays meter-long helical strings of disk-shaped egg capsules (known as a 'mermaid necklace') that

shield hundreds of embryos inside. Fig. 45a and b shows a channeled whelk (*Busycotypus canaliculatus*) and its egg capsules [219]. During incubation period (~10 months), the capsules have to protect the delicate embryos from various environmental damages, such as strong hydrodynamic forces generated by water at velocities more than 10 m/s, abrasion from sand, diffusion of poisonous substances, ultraviolet light, and attack from predators [220,221].

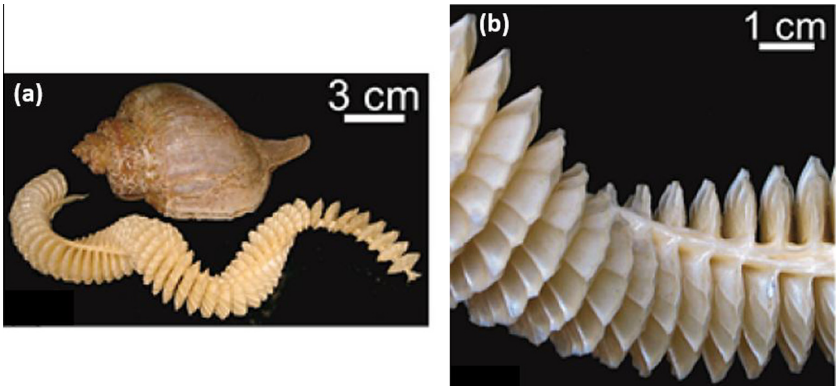

Fig. 45. Photographs of (a) a whelk (*Busycotypus canaliculatus*) and its string of egg capsules and (b) close view of the capsules [219].

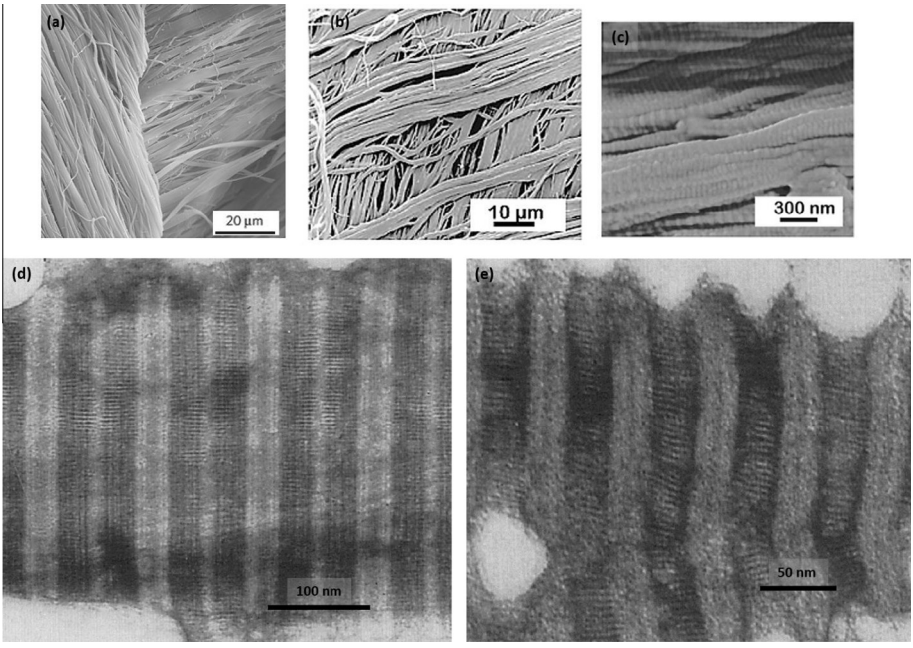

Fig. 46. Fibrous structure of the whelk egg capsule wall: scanning electron micrographs of egg capsule walls from (a) *Busycon canaliculum* [116] and (b) *Pugilina cochlidium* [225] showing the layered fibrils in cross-plywood sheets and slightly misoriented sheets, respectively; (c) scanning electron micrograph of the fibrils with the banding pattern [225]; transmission electron micrographs of egg capsule walls from (d) *Buccinum undatum* and (e) *Urosalpinx cinerea* revealing the regular lateral separation (~4.2 nm) within the bands [222].

The whelk egg capsule is a robust proteinaceous biopolymer, and studies have found that it possesses an α-helical coiled-coil structure (wide-angle X-ray scattering, sequencing of proteins) and shows multiple laminate sheets of ordered fibrils with periodicities 50 nm [219,222,223], which is structurally analogous to the α-keratinous materials [18,224]. At the nanoscale, the capsule wall shows distinct structural features: it consists of cross-plied or slightly misoriented sheets of protein fibrils (Fig. 46a and b); higher magnification observation of the fibrils reveals a crimped morphology and features a banding pattern with spacings of 50–105 nm depending on species (Fig. 46c–e) [225]. Transmission electron microscopic investigations show that the bands of both large and small whelks (*Buccinum undatum* and *Urosalpinx cinerea*) have a regular lateral separation of about 4.2 nm (Fig. 46d and e) [222], and this hierarchical structure is also observed for other whelk capsule walls, such as *B. canaliculatus* [226].

The whelk egg capsules also show very unique mechanical properties as an effective shock/energy absorber: under extension it undergoes α-helix ↔ β-sheet transition with large and reversible extensibility, and although this suggests of an elastomer that features low modulus, high extensibility, and entropy-driven elastic recovery, the capsule wall recovery is correlated to the internal energy arising from the facile and reversible α ↔ β transition [116,219,226]. Fig. 47a shows a typical tensile stress strain curve of capsule wall that indicates three regimes: an initial linear region with modulus ~160 MPa, a plateau with low modulus (~2 MPa) between 3% and 80% strain which corresponds to the α → β transition, and a stiffening region up to 170% breaking strain. Wide-angle X-ray scattering analysis of the capsule wall during deformation confirms the α-helix structure at 0% strain, the β-sheet formation at 70% strain and the α-helix structure at full unloading back to 0% strain [116]. When cyclically strained, the capsule wall shows a fourth regime: a large hysteresis loop on unloading with an

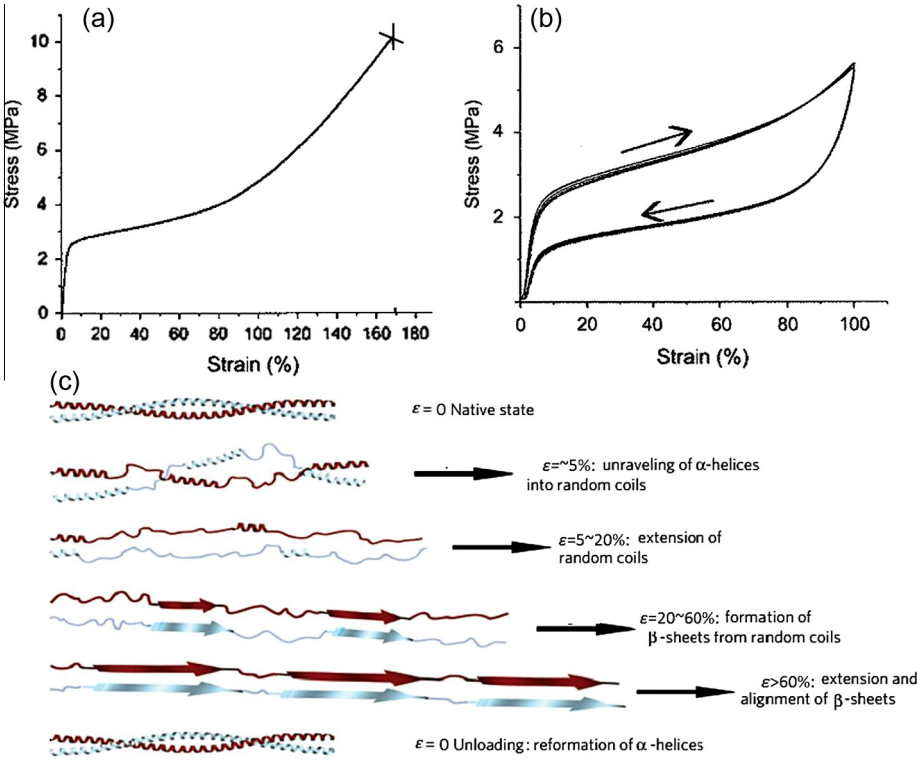

Fig. 47. Tensile stress strain curves of the egg capsule wall (a) extended to breaking and (b) cyclically strained to 100% multiple times continuously [219]. (c) Schematic illustration of the α-helix ↔ β-sheet transition during extension cycle at different strains [116].

energy absorbing hysteresis of 50% at 100% extension, and the recovery of strain and modulus is near instantaneous and fully repeatable (Fig. 47b) [227]. Fig. 47c shows schematically the structural changes of $\alpha \rightarrow \beta \rightarrow \alpha$ at different strains during load–unload cycle [116].

Through thermodynamic analysis on the high reversible extensibility relating the total elastic force (f) with the internal energy (f_U) and entropic energy (f_S) shown in Eqs. (14) and (15),

$$f = f_U + f_S = \left(\frac{\partial U}{\partial l}\right)_{V,T} - T\left(\frac{\partial S}{\partial l}\right)_{V,T} \tag{14}$$

where U is the internal energy and S is the entropy. Using the Maxwell relationship one can obtain:

$$f = \left(\frac{\partial U}{\partial l}\right)_{V,T} + T\left(\frac{\partial f}{\partial T}\right)_{V,l} \tag{15}$$

The total elastic force (f) of capsule wall decreases as temperature increases from −1 °C to 80 °C, contrary to rubbery elastomer which shows force increases with temperature, this indicates that internal energy change dominates over the entropy decrease in Eq. (15). This is verified by further incorporating the Clausius–Clapeyron relation to interpret the results; the findings agree with Flory's theoretical analysis of some elastic proteins that can achieve high extensibility through internal-energy dominant mechanisms [116].

3.2. Keratinous materials based on β-keratin

Feathers and avian and reptilian scales show the same keratin genes [228], and it is well-accepted that the hard keratin of feathers and these scales is the β-sheet based on X-ray diffraction patterns [24,26,57,100,229,230] and transmission electron microscopy [16,91]. Therefore, feathers are discussed here representing both. Beaks and claws are also included in this chapter.

3.2.1. Feathers

How birds fly has fascinated humans ever since very early days; even Leonardo da Vinci wrote a paper [231] examining flight behavior of birds and proposing the mechanisms. Among the distinct characteristics enabling birds to fly, the feathers are the most essential component and make the most contribution [232], a unique feature that distinguishes them from other animals.

Typically, a feather is composed of a central shaft and laterally attached vanes on the two sides (Fig. 48a, adapted from [233]). The shaft can be subdivided into the calamus and the rachis, and consists of a hollow tube called cortex and a foam core called medulla. The proximal part of the feather shaft, the calamus, anchors the feather into the bird's skin (embedded in the feather follicle) and has a cylindrical shape, and the rachis with a more angular shape (above the skin) supports barbs and barbules which are connected via hooks and bow radiates, forming the vanes that are light, flexible and resistant to damage [233,234]. The flight feathers are long and asymmetrically shaped (seen in Fig. 48a) on the wings (remiges) but have bilateral symmetry on the tail (rectrices). In addition, the asymmetry and organization of the remiges give the feathers an airfoil shape: (1) the leading edge of a feather is narrower than the trailing edge (Fig. 48b); (2) the feathers are aligned on the wing, partially overlapping with each other, as the trailing edge of a feather is covered by the leading edge of next feather (Fig. 48b [235]).

The demands of flight cause the feather shaft (the major structural support of the feather) to bend, similar to a cantilever [236]; thus the shaft must be lightweight, sufficiently stiff and resistant to wear-induced damage, since it can be replaced only periodically during molting [237]. The general design of a feather shaft resembles a sandwich-structured composite: a dense keratin cortex surrounds a spongy keratin medulla, which maximizes strength and resists flexure and rupture while minimizing weight [183,238]. Fig. 49 shows the cross sections of flight feather shaft from California gull along the shaft axis from the calamus to feather tip, indicating the geometry change from circular to rectangular. The dorsal and ventral walls of the cortex are thicker compared with the lateral walls. There are membranous struts inside the cortex at the calamus, reduced struts and increasing foam-like medullae at middle rachis, and all foam-like medullae at distal rachis. It has been generally

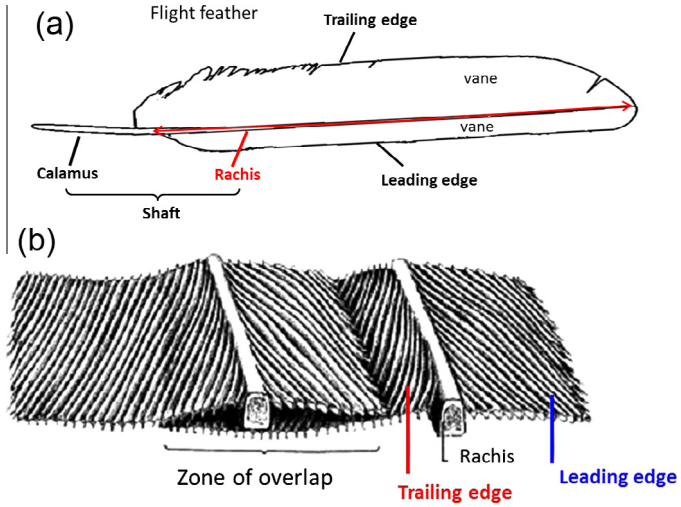

Fig. 48. Morphology of a flight feather: (a) components including calamus, rachis and asymmetrical vanes (adapted from [233]); (b) [235] organization of flight feathers – the overlapping zone between two remiges – that gives an airfoil shape.

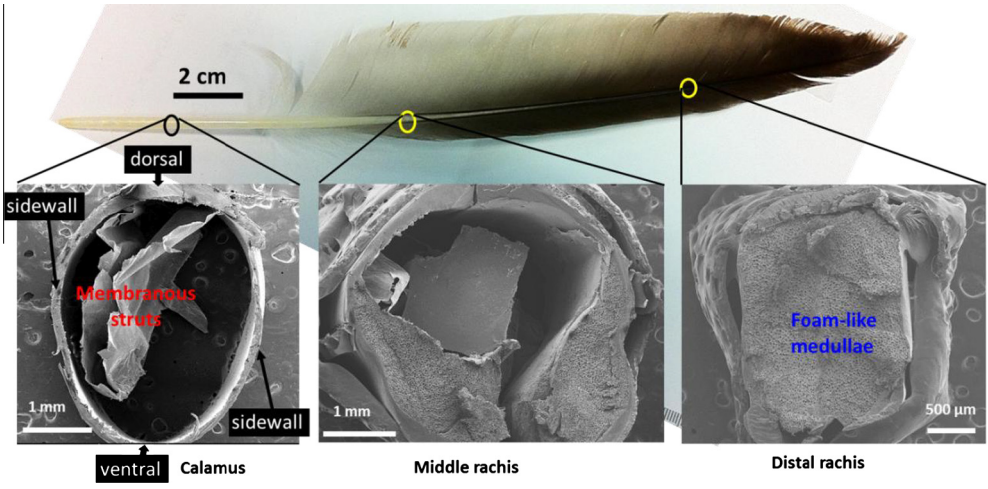

Fig. 49. Structure of the feather from California gull: a feather (upper) and scanning electron micrographs of transverse cross-sections of the cortex along the feather shaft length (the dorsal, ventral and sidewalls of cortex are indicated). It is a hollow cylinder filled with struts at calamus, reduced struts and increasing foam-like medullae at middle rachis, and all foam-like medullae at distal rachis.

agreed that the feather rachis has three major components, which are illustrated in Fig. 50 [155]: (i) the superficial layers consist of fibers that wound circumferentially around the rachis (Fig. 50a and b, orientation indicated by double-headed arrow); (ii) a thick layer, through the thickness of the cortex, composed of the fibers (6 µm in diameter reported by [239]) aligned in parallel to the rachis axis (Fig. 50a and c, orientation indicated by double-headed arrow); (iii) the feather central core composed of closed-cell foam-like medullae, and the cell (about 20–30 µm in diameter) walls exhibit a porous and fibrous structure (Fig. 50e and f) with curved fibrils piling up with spaces, further down in the structural hierarchy.

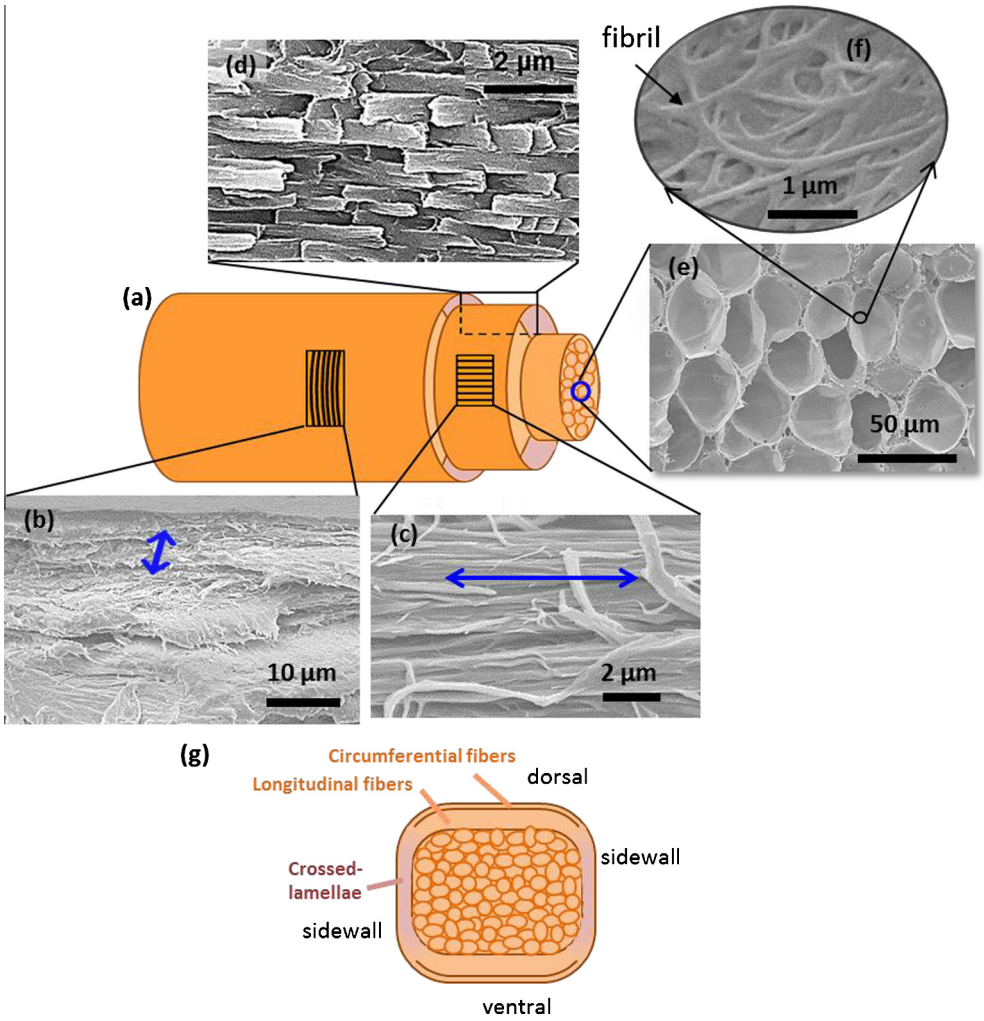

Fig. 50. Fibrous structural components of a feather from seagull: (a) schematic drawing of the feather rachis; (b) circumferential fibers in thin outer layer (orientation indicated by double-headed arrow); (c) longitudinal fibers (orientation indicated by double-headed arrow) composing the thick bulk inner layer; (d) crossed-lamellae composing the entire sidewalls of cortex; (e) closed-cell foam-like medullae of the feather core; (f) the fibrous structure of the medulla; (g) schematic of the transverse cross section of the feather cortex, showing the circumferential and longitudinal fibers composing the dorsal and ventral cortex and the crossed-lamellae composing sidewalls.

An interesting finding by Wang et al. [155] is that the entire lateral walls of rachis and barbs reveal a crossed-lamellar (300–600 nm thick) structure, as shown in Fig. 50d. The lateral walls of cortex in the rachis and barbs consist of oppositely oriented in alternate layers of crossed-fibers (about 100–800 nm in diameter), shown in Fig. 51 (the arrows indicate the boundary between the cortex and sidewall of cortex) [240]. Transmission electron micrographs of feathers show the fine filament-matrix structure (Fig. 16f) [91] with the β-keratin filaments, about 3 nm in diameter, embedded in an amorphous matrix.

Feathers of flying birds have to withstand aerodynamic forces [241,242], and the knowledge of the relationship elucidating the functions of feathers and their hierarchical structure is still insufficient and somewhat debatable. The Young's modulus of cortical rachis reported in the literature shows sig-

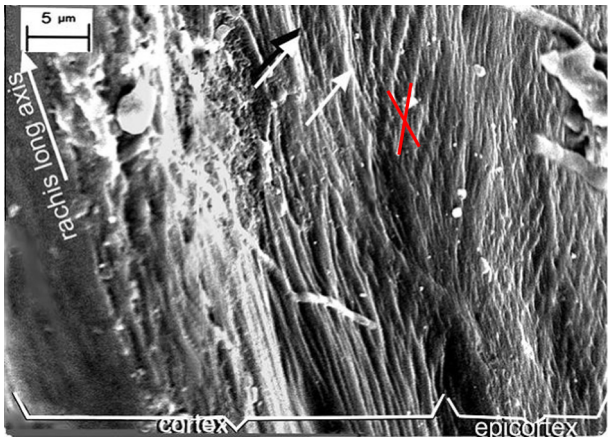

Fig. 51. Scanning electron micrograph of the sidewall of feather cortex (epicortex) showing the crossed-fiber structure (indicated by two red crossing lines) from a domestic chicken (*Gallus gallus*). Arrows show the boundary between the cortex and sidewall of cortex [240].

nificant variations, ranging from 9.0 GPa (tension, [243]) to 0.05–0.68 GPa (tension on contour feathers (feathers cover the exterior body), [244]). This is surprising considering that the feather keratin should have somewhat similar mechanical properties, since β-keratin is biochemically highly conservative [245] and the molecular packing and filament framework is common to various avian keratins [57]. Thus the variability in Young's modulus may be due to differences in experimental procedures [120].

Bonser and Purslow were the first to identify the interspecific variations in Young's modulus of feather rachis of eight species of birds [120]. Based on tensile tests on cortex strips from rachis, they reported that the variations in mechanical properties of feather keratin among different species were low, and the mean Young's modulus of the feather cortex is about 2.5 ± 0.1 GPa, shown in Fig. 52a. These are more reasonable values than the range quoted above [243,244].

The feather rachis resembles a cantilever beam structure whose bending is controlled by the flexural stiffness along its length. For the dorsoventral plane, this stiffness is determined by both the longitudinal Young's modulus and the second moment of area [120]. Significant intraspecific variations in

(a)

Species	Young's modulus (GPa)	*N*
Rock pigeon	2.42	9
Willow ptarmigan	2.71	11
Mute swan	2.39	1
Eurasian sparrowhawk	2.41	9
Black-headed gull	2.04	3
Tawny owl	2.76	6
Grey heron	1.78	3
Common starling	2.67	9
Mean	2.50	51

(b)

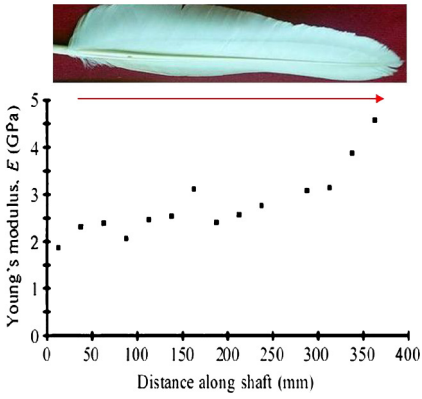

Fig. 52. (a) Young's moduli of feather keratin from eight species of birds; (b) longitudinal variation in Young's modulus along the length of a mute swan's primary feather [120].

Young's modulus and geometry along the length of feather rachis were identified [120,233,244]. Fig. 52b shows that along the wing feather of a Mute Swan, from the proximal part to the distal end, the tensile Young's modulus increases monotonically, from 1.8 GPa to 3.8 GPa [120]. Earlier studies [244] also showed similar longitudinal variations in Young's modulus along feather length in four different species of birds. This may be due to the structural changes of the cortex: as moving from the proximal to the distal part, the thickness of the inner layer with keratin fibers aligned parallel to the axis of the feather becomes larger [246,247], indicating that the fraction of longitudinally aligned filaments increases from the proximal end to the distal end; therefore the stiffness of the cortex increases. Cameron et al. [248] reported that a higher axial alignment of keratin fibers and a higher Young's modulus along the rachis length toward the feather's tip in flying bird species (geese and swans), whereas such trend was absent in the non-flying ostrich. However, no significant trends in stiffness or strength from the proximal to distal regions along the length of the feather are observed in Toco toucan rectrices (Fig. 53; [144]). This study concluded that the differences may be related to a temporal or aging effect. It is also reported that for peacock tail coverts samples at distal regions are significantly less crystalline than other regions along the feather length [249].

Liu et al. [250] separated the cortex from the internal medulla in the rachis of peacock and tested them separately and jointly. This was done in both dry and wet conditions and the effect of humidity is, as expected, dramatic. Fig. 54a and b presents the compressive response of cortex and medulla, respectively. The medulla has the classic plateau associated with the collapse of the medullary cells. There is some synergy because the entire rachis has a higher strength, both in the dry and wet conditions, than what is predicted from a simple rule-of-mixtures from medulla and cortex, shown in Fig. 54c.

The bending stiffness (product of Young's modulus and second moment of area) has been reported to be predominantly influenced by the geometry of feathers rather than by the material properties [233]. From Fig. 55a, along the feather shaft length from proximal to feather tip for barn owls and pigeons, the bending stiffness increases first and then decreases, and the barn owl show higher stiffness values than pigeon. This is mainly due to the geometrical differences between the cross sectional

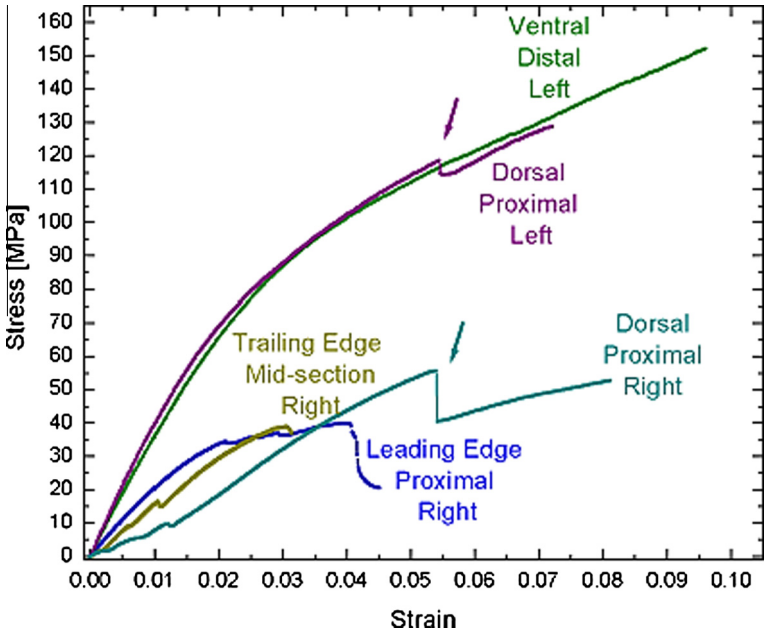

Fig. 53. Tensile stress–strain curves of feather rachis from Toco toucan rectrices, in which no obvious gradient in Young's moduli from the proximal to distal regions is observed [144].

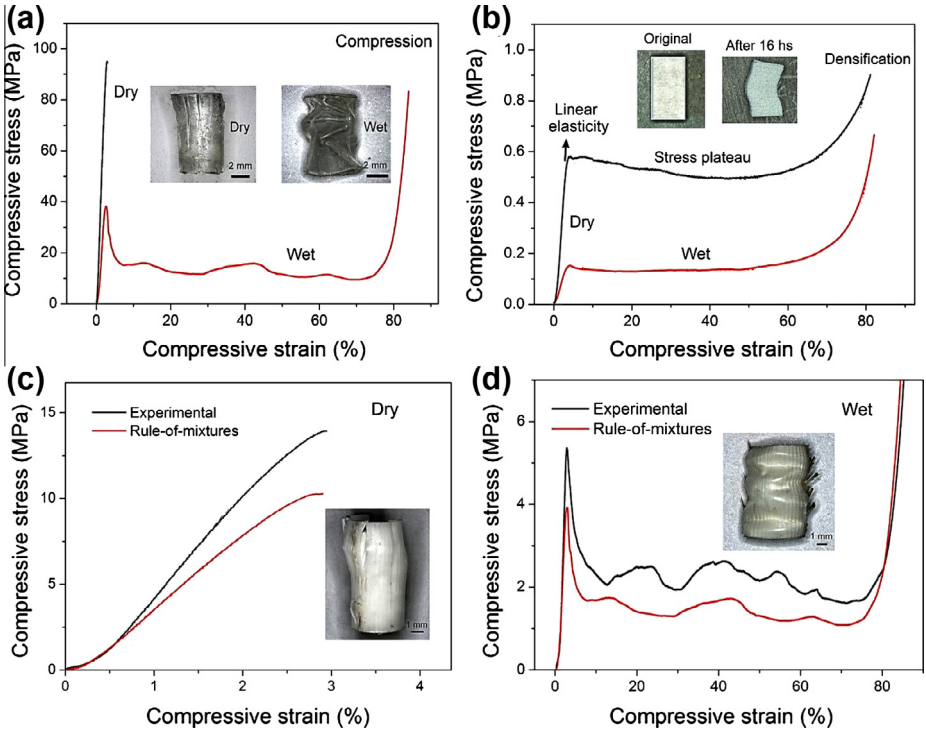

Fig. 54. Compressive behavior of tail feather from peacock: (a) stress–strain curves of cortex at dry and wet conditions; (b) stress–strain curves of medullary foam at dry and wet conditions; stress–strain curves of experimental overall rachis and the calculated ones at (c) dry and (d) wet conditions [250].

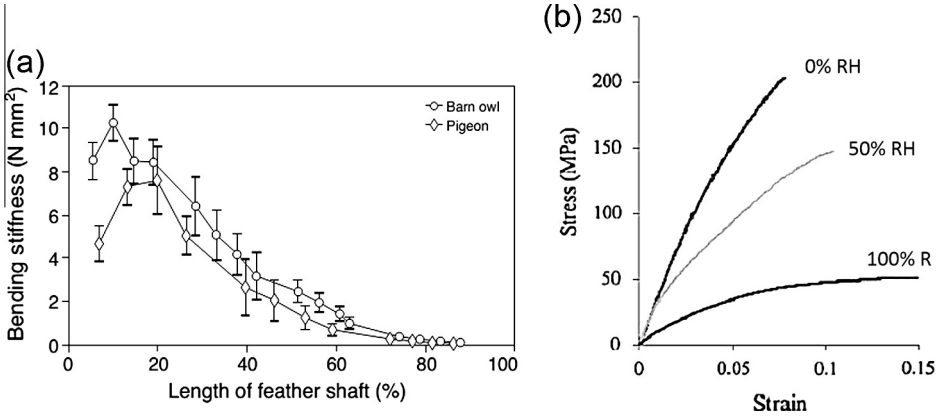

Fig. 55. (a) Variation of the bending stiffness along the length of the feathers (of rachis of remiges from barn owl and pigeon [233]. (b) Tensile stress–strain curves for rachis from ostrich contour feathers at three humidities: 0%, 50%, and 100% [152].

profiles of the two species since no significant variations in Young's moduli were found. As typical keratinous material, mechanical properties of feathers are sensitive to humidity. Very few and superficial studies on the effects of humidity on feather keratin have been conducted [251]. Fig. 55b shows the

tensile response of contour feather rachis from ostrich at different relative humidities: as the moisture content of feather rachis increases, both modulus and strength decrease, but the strain to failure increases [152].

3.2.2. Beaks

The rhamphotheca (surface layer) of bird beaks is composed of hard keratinous material, and it enables the beaks to serve a variety of functions, such as foraging, feeding, fighting, social interaction and grooming [252,253]. Avian beaks continuously grow and are composed of bone and keratin [254]. They are typical low-weight, sandwich-structured composites. Bird beaks usually fall into two categories: short/thick and long thin. But the toucan beak is both long and thick, with a density about 0.1 g/m^3. The beak comprises one-third of total length of the bird, but makes up only one twentieth of its mass [153]. Fig. 56 shows the morphology and microstructure of a Toco toucan beak [153,255,256]. It consists of an exterior keratin shell, the rhamphotheca, and an interior, bony foam with a fibrous network (Fig. 56a and b). From Fig. 56c the internal foam exhibits a closed-cell configuration, and most of the cells are sealed by membranes. The total outer shell thickness varies between 0.5 and 0.75 mm, consisting of multiple layers of keratin scales (Fig. 56d). The thickness and diameter of each scale are approximately 2–10 μm and 30–60 μm respectively.

Fig. 57a shows typical tensile stress–strain curves of the rhamphotheca of a Toco toucan beak along different orientations [255]. There is significant scatter in the results (Fig. 57b), but no systematic difference in Young's modulus and yield strength along the transverse and longitudinal directions (the mean Young's modulus is 1.4 GPa and the yield strength is 30 MPa). Thus the rhamphotheca can be considered transversely isotropic. Fig. 57c shows the compressive stress–strain curves of the interior foam, which is bone and not keratin. The plateau region is associated with the collapse of the cell walls, and the densification of the cell walls occurs after the plateau [153,255].

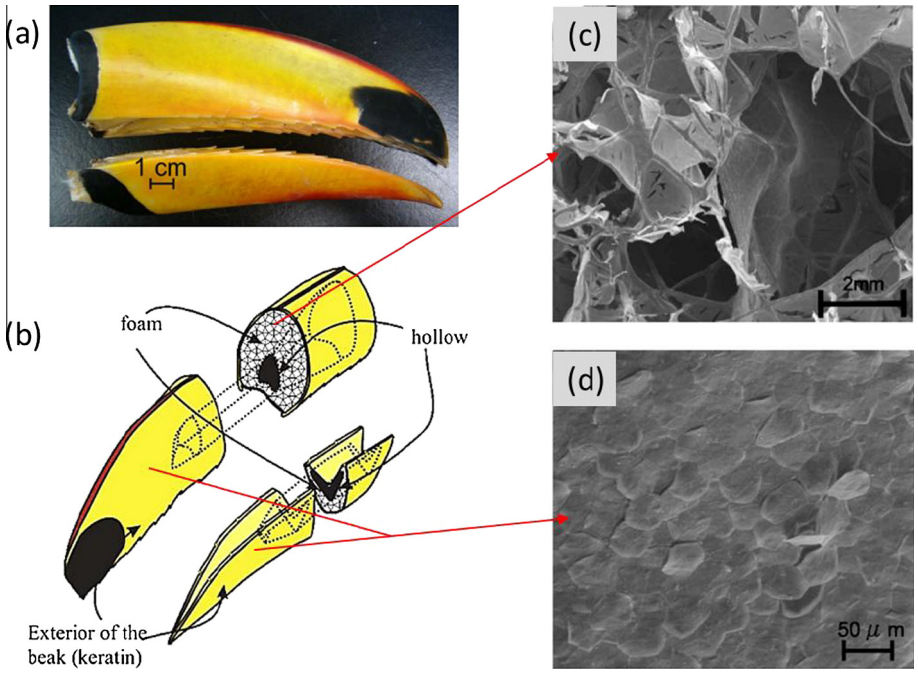

Fig. 56. Structure of a Toco toucan beak: (a) photograph of the beak showing maxilla and mandible [256]; (b) schematic showing internal and external structure; (c) scanning electron micrograph of the interior of beak, showing the foam with closed cells (several are crushed/ripped); (d) scanning electron micrograph of the rhamphotheca,(keratinous surface) showing the keratin scales [255].

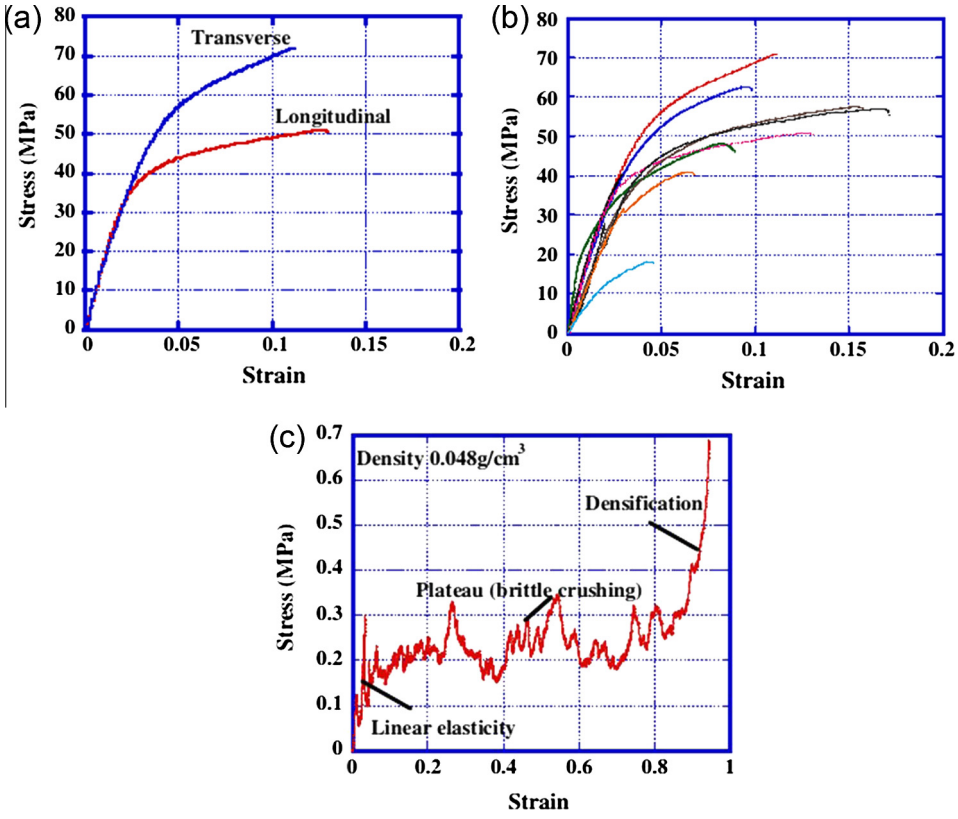

Fig. 57. Mechanical properties of a Toco toucan beak: (a) representative tensile stress–strain curves of the rhamphotheca along transverse and longitudinal orientations [255]; (b) tensile stress–strain curves showing the scatter of results; (c) compressive stress–strain curve of the interior foam showing characteristic cellular response with plateau [153].

As a polymeric composite, the rhamphotheca of the toucan beak shows strain-rate dependence and the tensile failure mode changes from keratin scale pull-out to brittle scale fracture as the strain rate increases (shown in Fig. 58). The pulled out scales are the result of viscoplastic shear of the interscale material at low strain rate which enables a large amount of molecules to move and change their configurations and the scales to slide. At high strain rate (1.5×10^{-3}/s, in Fig. 58b), the keratin scales are fail in tension, which is characterized as brittle failure. Fig. 59 presents the yield stress and ultimate tensile strength (UTS) as a function of strain rate [153]. When the yield stress approaches the UTS, brittle fracture of the scales occurs over viscoplastic deformation of the interscale material. The transition from pull out to brittle fracture is governed by the criterion,

$$\sigma_t \leqslant \sigma_g \quad \text{or} \quad \sigma_t \geqslant \sigma_g \tag{16}$$

where σ_t is the fracture stress and σ_g is the flow stress by interscale gliding. The strain rate dependence of σ_g can be expressed as

$$\sigma_g = k\dot{\varepsilon}^m \tag{17}$$

where m is the strain rate sensitivity. The competition between viscoplastic shear of the interscale material and brittle fracture is similar to the response showed by the abalone shell in tension [257].

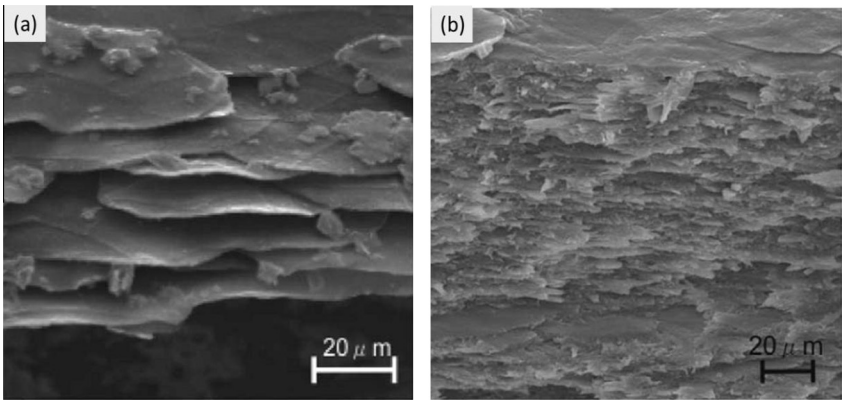

Fig. 58. Scanning electron micrographs of the fracture surfaces of the Toco toucan rhamphotheca after tensile testing [153]: (a) pullout failure at strain rate of 5.0×10^{-5}/s; (b) brittle failure at strain rate of 1.5×10^{-3}/s.

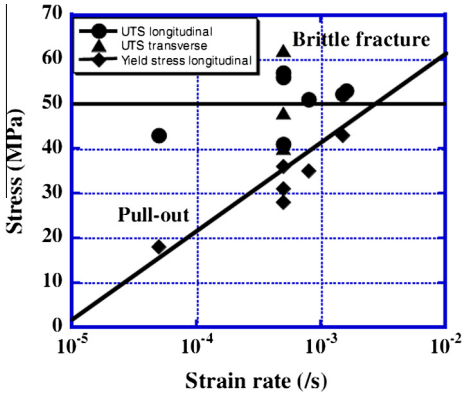

Fig. 59. Yield strength and ultimate tensile strength (UTS) of the Toco toucan rhamphotheca as a function of strain rate [153]. Note transition from ductile (pullout) to brittle fracture.

3.2.3. Claws

Claws are curved, pointed appendages found at the end of digits in most amniotes (terrestrial egg laying animals), and they differ from nails which are flat and do not possess a sharp point. Claws of birds and reptiles show a β-type structure, which are the subjects in this section; whereas the claws of mammals are not because they show an α-type (see Section 3.1.6). The claw functions are catching and holding prey, digging, climbing and grooming. Fig. 60 shows the morphologies during a mouse claw development [258]. It begins on the webbed digits on the 14th day of gestation with a slight thickening of the epidermis near the tip of the digit (Fig. 60a and b). By 15 days a groove on the dorsal and lateral surfaces of the digit outlines the proximal border of the claw field. A proximal fold starts to form at the proximal groove at 16 days of gestation (Fig. 60c and d). The claw develops and reaches the end of the digit by birth at 21 days of gestation (Fig. 60e and f), and at this time it is similar to adult claw (Fig. 60g and h). The claw is curved both longitudinally and laterally and extends well beyond the end of the digit.

Claws consist of a superficial and a deep layers of hard keratin, these two layers being produced by the basal and terminal matrices respectively [259,260]. The beta-keratin filaments are oriented parallel to the direction of growth in claws of various species and at intermediate angles in claws of some

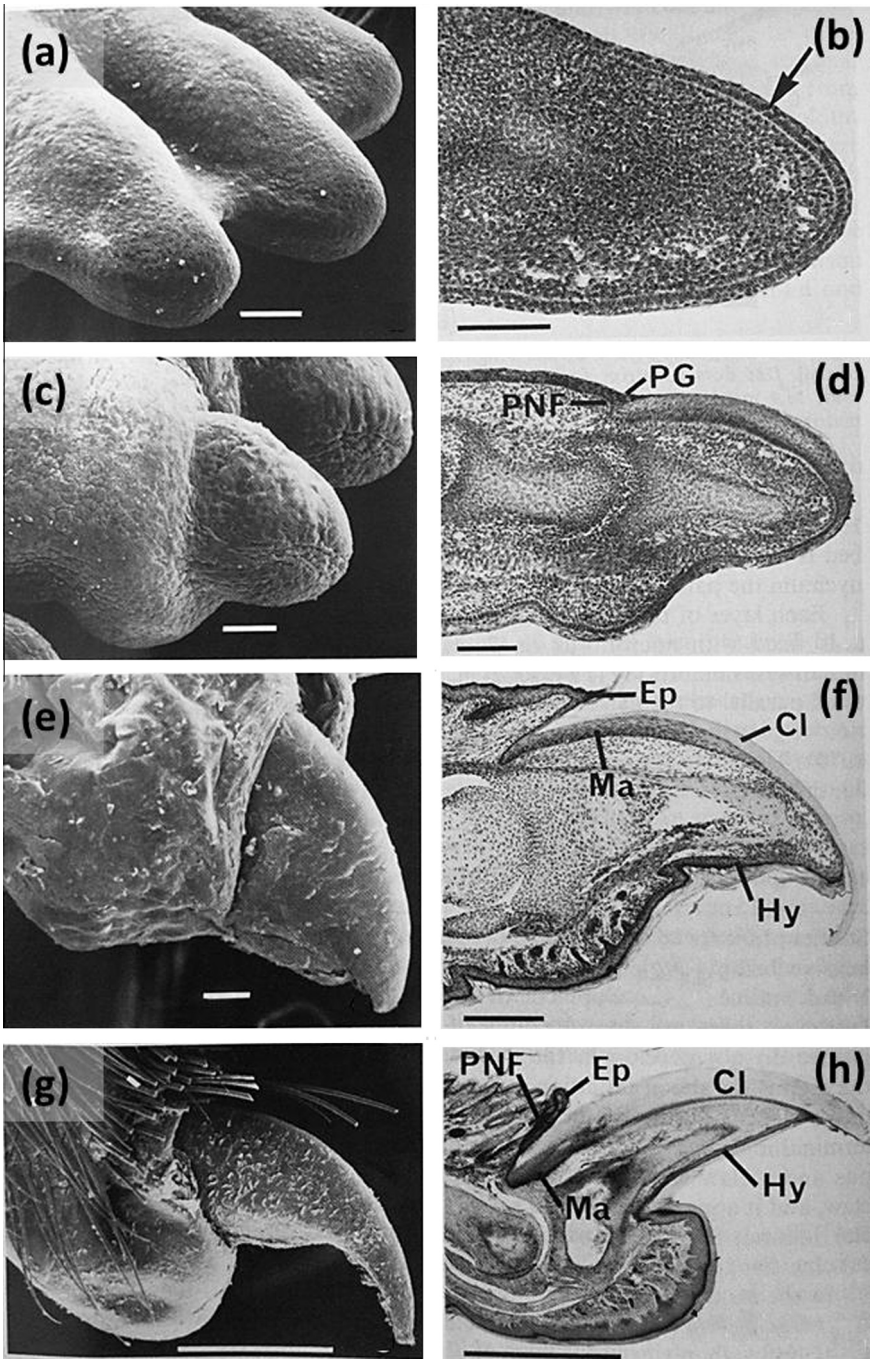

Fig. 60. Surface views (a, c, e, and g) and longitudinal sections (b, d, f, and h) of digits of fetal (a and b 14 days of gestation, c and d 16 days gestation), newborn (e and f) and adult mice (g and h) showing evolution of the claw morphology. Arrow in (b) indicates the initial epidermal thickening of claw. Cl, claw; Ep, eponychium (the thickened layer between the claw and epidermis); Hy, hyponychium (the thickened epithelium under claw); Ma, matrix; PG, proximal groove; PNF, proximal nail fold. Scale bars: (a–f), 0.1 mm; (g and h), 1.0 mm [258].

primates [204], e.g. marmosets and tamarins. A transmission electron micrograph (Fig. 16g) of fowl claw shows clearly beta-keratin filaments with about 3.5 nm in diameter embedded in a dark (densely stained) matrix [16].

Claws have to transmit and withstand substantial forces during locomotion, and must resist abrasive wear from contact with substrates [261,262]. The mechanical properties of claws have not been studied widely or in detail. It is reported that for ostrich claw keratin, the tensile Young's modulus along the length direction is 1.84 GPa and that perpendicular to claw length is 1.33 GPa [263]. This weak anisotropy is compared with horse hooves which have comparable modulus (2–3 GPa) and are 10–40% less stiff transversely than longitudinally [264,265]. The porcupine quills are only about 10% as stiff transversely as longitudinally [111]. The mechanical anisotropy of keratins comes from the preferential orientation of fibers, which is correlated with the real loading conditions the animals and tissues experience. The explanation for the weak anisotropy of claws may be that the loadings that the claws endure through life are less predictable or do not have a preferred direction [263].

The effects of water content on the tensile mechanical properties of ostrich claw are listed in Table 8 [152]. As the relative humidity (RH) increases from 0% to 100%, the Young's modulus and tensile strength decrease significantly, from 2.7 to 0.14 GPa, and from 90.3 to 14.3 MPa, respectively, while the strain to failure increases. This trend is similar to those of α-keratinous materials discussed in Sections 2 and 3.1. As it was reported [263] that claw keratin tends toward isotropy in Young's modulus along and across the claw axis, it is suggested that the claw keratin is less ordered and more sensitive to hydration [152].

3.3. Keratinous materials based on α- and β-keratin

3.3.1. Reptilian epidermis

The epidermis of reptiles synthesizes both α- and β-keratins [92,100,266–271]. The α-layer of squamates (lizards and snakes), turtle leg and neck epidermis, and crocodilian epidermis, yields an α-type X-ray diffraction pattern [230] and consists of 7–8 nm diameter filaments in an amorphous matrix [272]. The β-layer of squamate scales, turtle and tortoise shell epidermis and crocodilian epidermis yields a β-type X-ray diffraction, and consists of 3 nm filaments in an amorphous matrix [273].

The reptilian epidermis has certain characteristics in common whereas among the orders of reptiles, the anatomy of the epidermis differs remarkably [273,274]. We discuss below the nature of keratins in reptiles.

- *Squamata.* Lizard epidermis is composed of a complex sequence of cornified layers consisting of the Oberhäutchen (from German: little surface skin), beta, mesos, and alpha layers (shown in Fig. 61,

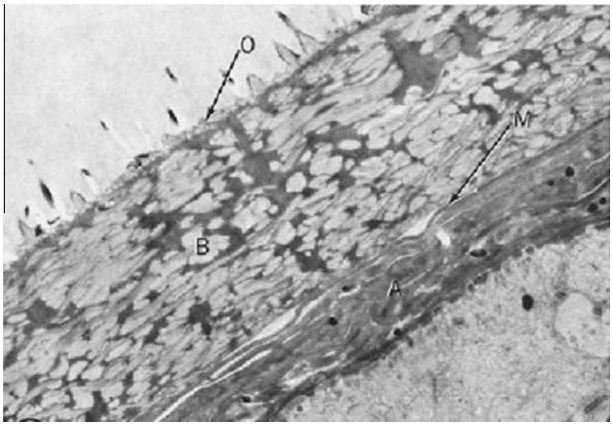

Fig. 61. Cross section of epidermis of American chameleon showing both α- and β-keratin layers. O: oberhäutchen layer; B: beta layer; M: meso layer; A: alpha layer [275].

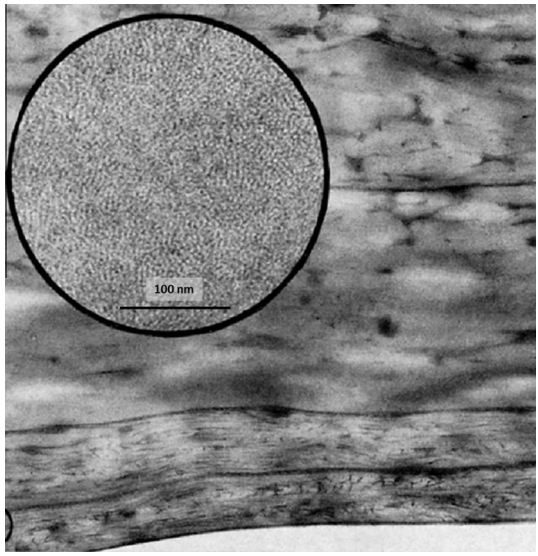

Fig. 62. Transmission electron micrographs of the epidermis of the desert iguana, *Dipsosaurus dorsalis*. The β layer (upper) is compact without visible cell outlines. The inset shows the β pattern keratin consisting of 3 nm filaments embedded in amorphous matrix. The bottom of the figure is the mesos-layer where the cells become more reticulated. The mesos experiences a transition from the β to the α layer and the filaments yields an α-keratin pattern [273].

[275]), which all rest upon a stratum of living cells. Fig. 62 shows a transmission electron micrograph of the beta-layer of desert iguana, and the structure with 3 nm filaments embedded in matrix [273]. The snake (Kenyan sand boa *Gongylophis colubrinus*) epidermis also shows similar structure including the Oberhäutchen layer, beta-layer (thick), mesos-layer (2–10 layers of flattened cells containing α-filaments), alpha-layers (several keratinized cell layers), lacunar tissue (1–4 cell layers) and the clear layer (lies directly above the stratum germativum), shown in Fig. 63 [154].

- *Crocodilia.* The cornified epidermis of crocodilians (crocodilian scales) varies in composition. It has the characteristics of a beta layer (corneocytes about 0.3–0.6 μm thick composed of β-keratin) and

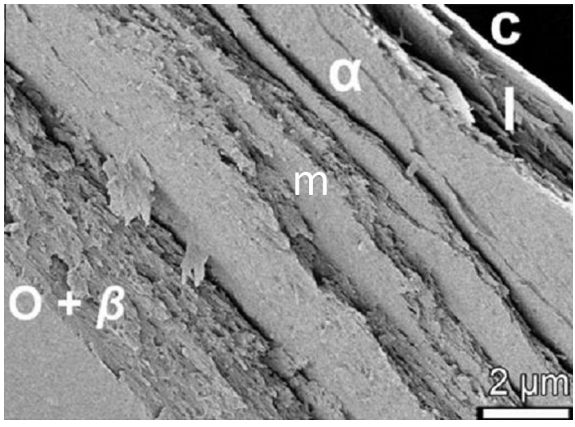

Fig. 63. Cryo-scanning electron micrograph of the epidermis of the ventral scale from the Kenyan sand boa *Gongylophis colubrinus*. The epidermis consists of (from outside to inside): Oberhäutchen + β-layer (O + β), mesos-layer (m), α-layer (α), lacunar tissue (l), and clear layer (c) [154].

the hinge region appears like a mesos layer with characteristics of both α- and β-keratins [270,273,274,276].

- *Testudines.* The cornified epidermis of the carapace of the turtles and tortoises is composed of β-keratin which is firmly attached to the underlying living cells. The pliable epidermis of their head, neck and leg skin is composed of α-keratin over a layer of living cells [92,99,273,277].

The mechanical properties of epidermis from reptilians have been investigated. Tensile tests on skin strips (the outer from the inner layer of the dermis, 0.30 mm) from a gecko (*Ailuronyx seychellensis*) show a breaking stress of 0.9 MPa, an elastic modulus of 4.6 MPa and failure strain at 0.3 [278]. Mechanical studies on the epidermis shed in four snake species demonstrate that all species show a gradient in properties: the integument consists of hard, robust outer scale layers (Oberhäutchen and beta-layer) with a higher effective modulus and higher hardness, and soft, flexible inner scale layers (alpha- and clear layers) [154,279]. Fig. 64 shows the nanoindentation results for the outer scale layers and inner scale layers of ventral scales from Kenyan sand boa *G. colubrinus* [154] as a function of indentation depth. It is clear that the outer scale layers exhibit much higher values all through the load–displacement than the inner scale layers (Fig. 64a), and thus the effective modulus obtained for outer scale layers (4.1 GPa) is higher than that of the inner scale layers (3.2 GPa). There is also a difference between the hardness values of the outer (0.28 GPa) and inner (0.14 GPa) scale layers. Compared with other keratinous materials and considering the mechanical variations of α- and β-keratins, it was suggested that the β-layers' main function is to protect the epidermis against abrasion [280], and that the high abrasion resistance of snake epidermis is due to the material property gradient of

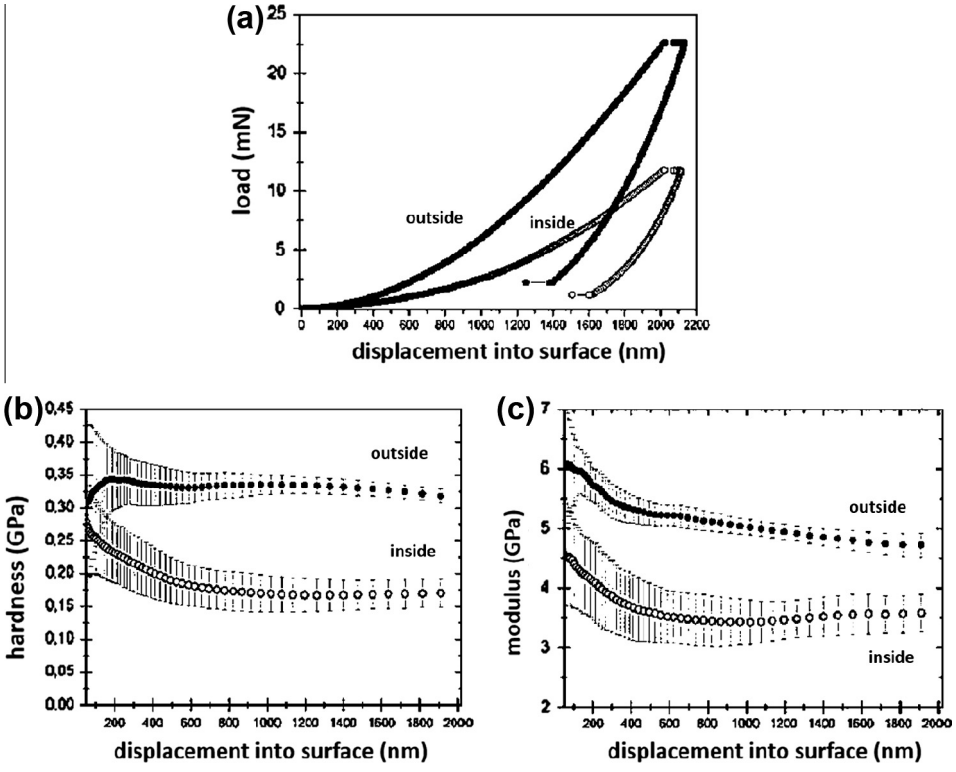

Fig. 64. Variation in nanoindentation from the outer (outside) and inner (inside) scale layers in Kenyan sand boa *Gongylophis colubrinus*. (a) Load–penetration curves; (b) hardness variation with penetration in outer and inner layers; (c) effective elastic modulus as a function of penetration for outer and inner layers. The error bars denote the standard deviations [154].

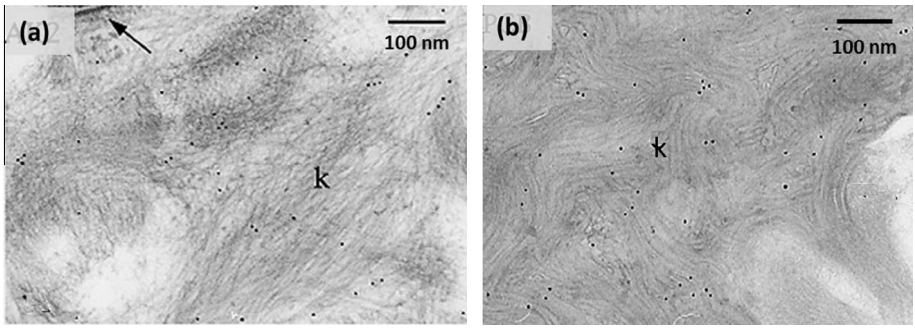

Fig. 65. (a) Carapace epidermis of spiny soft shell turtle (*Apalone spinifera*) showing the prevalent α-keratin bundles (k) (immunogold-labeling with AK2 antibody which recognizes α-keratin); arrow points to a desmosome. (b) Carapace epidermis of Florida redbelly turtle (hard-shelled) (*Pseudemys nelsonii*) showing the β-keratin bundles (k) (immunogold-labeling with PCB antibody which recognizes β-keratin) [287].

the integument from a hard and inflexible outside to a soft and elastic inside [154]. For a system involving large loads under pressure against abrasion, such a design leads to more uniform stress distribution and the minimization of the probability of local stress concentration [183,281]. This is similar to other biological materials, such as tooth, in which the hard enamel envelops the soft pulp, with gradient of material properties to endure high amounts of stress under pressure, a key feature against abrasion wear [281,282]. Fish scales use the same design concept, a highly mineralized surface and a tougher foundation.

3.3.2. Hard and soft epidermis of testudines

Testudines (turtles, tortoises and terrapins) represent an ancient group dating back to about 220 million years with a unique type of body plan and embryonic development [99,283–285]. The shell is the shield for the ventral and dorsal parts of testudines and the outer bony plates (scutes) are covered with keratin. The dorsal shell is called the carapace and the ventral shell is called the plastron. The turtle shell has been attractive to manufacturers for a wide variety of products such as combs, containers, frames and inlays in furniture, due to its beautiful appearance, durability and organic warmth to skin. Among species, the shell scute of the hawksbill turtle with large size, fine color and unusual form makes it especially suitable for the manufacture of ornaments. Prior to the development of synthetic polymers, turtle shell was the principal biopolymer.

Recent studies [286,287] suggest that (i) both α- and β-keratins are present in the shell scutes and in skin tissues (soft epidermis on neck, tail, limb) of both hard- and soft-shelled turtles, with much higher amount of β-keratin in carapace in hard-shelled turtles and higher amount of α-keratin in the carapace and skin tissues in soft-shelled turtles; (ii) the ratio of β-keratin to α-keratin is highest in the carapace in hard-shelled turtle, higher than that in skin tissues in soft- and hard-shelled turtles and lowest in the carapace in soft-shelled turtles; (iii) the non-shelled epidermis in hard-shelled turtles and all areas of the epidermis in soft-shelled turtles synthesize β-proteins, but some mechanisms for formation of β-keratin regions are missing, preventing enough aggregation of β-keratin among α-keratin. Fig. 65 shows the prevalent α-keratin bundles in the carapace of spiny soft-shell turtles and the keratin bundles of β-type in the carapace of hard-shelled Florida redbelly turtles [287].

Mechanical properties of the turtle shell, mainly focusing on the bony cortices and cancellous interior via bending [288], indentation, compression, flexure and modeling [289–292], compression, tension and simulation [293,294], have been studied. The composite structure and mechanical properties in different orientations of dry red-eared slider turtle (*Trachemys scriptaare*) shell are illustrated in Fig. 66 [292]. Fig. 66b–d shows the keratin layers covering the bony interior. Along the cross section of the carapace, the keratin shows an elastic modulus around 3.5–4.2 GPa, the dorsal cortex 16.5 GPa, cancellous interior 12.5 GPa, and ventral cortex 12 GPa. The elastic modulus increases from ~8 GPa to 12 GPa along the suture from tooth edge toward the bulk. The keratin scutes are softer than the bone,

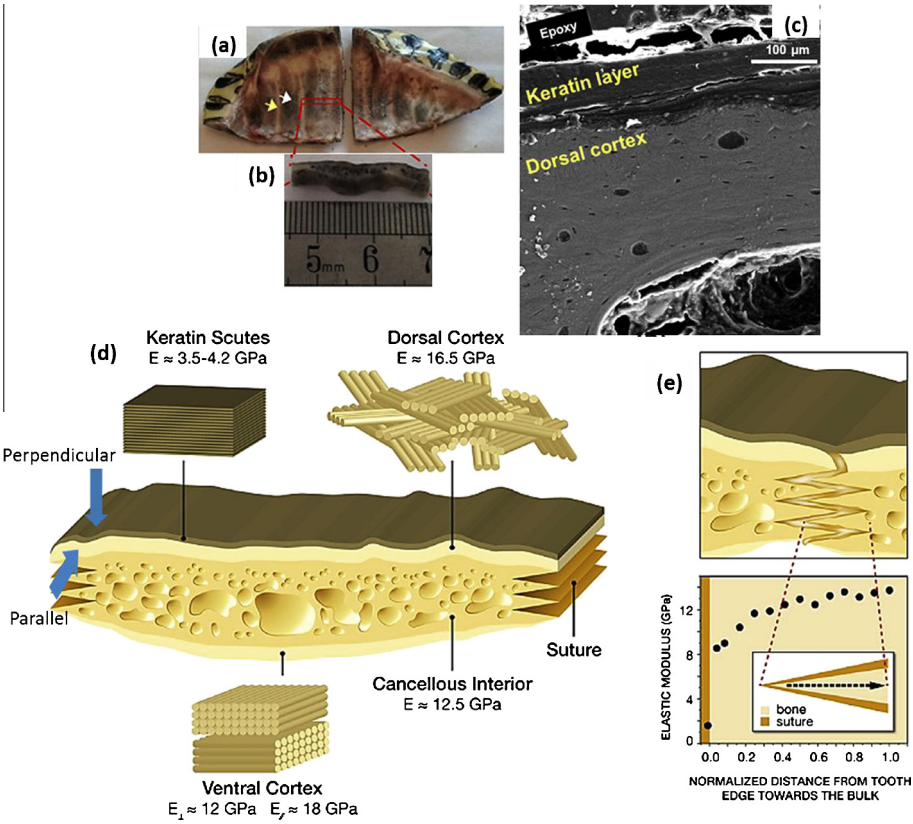

Fig. 66. Turtle shell structure and mechanical properties [292]: (a) ventral view of a dissected carapace. Arrows mark individual rib and suture; (b) section of the rib enclosed by sutures at both edges; (c) scanning electron micrograph of section through dorsal region showing the keratin layer and dorsal cortex; (d) schematic of the carapace cross-section, showing structural organization and elastic moduli of the three regions (keratin, compact and cancellous dorsal cortex). The two indenting directions used in Table 12 (parallel and perpendicular) are specified with arrows; (e) schematic of the suture with variation of elastic modulus along normalized distance from the tooth edge toward the bulk (average tooth length ~0.5 mm).

but the stiffness is sufficiently adequate, and keratin is an extremely tough tissue characterized by pronounced yielding and post-yield regions, reaching strains of over 30% (e.g. wool and hair, Fig. 17). Table 11 [292] lists the elastic modulus and hardness of the keratin scutes under different hydration levels and in different orientations. Under dry condition, the keratin layer shows modulus and hardness about 3.6 and 0.15 GPa when indented perpendicularly, and 4.2 and 0.22 GPa when indented parallel to the keratin layers, indicating only minor mechanical anisotropy. This is ascribed to the complex architecture involving the fibrous keratin IFs in matrix, the arrangement of various

Table 11
Mean elastic modulus (E) and hardness (H) of the keratin scutes measured by nanoindentation of the turtle carapace [292].

State	Indenting direction	E (GPa)	H (GPa)	Number of measurements
Dry	Perpendicular to keratin layers	3.6 ± 1.5	0.15 ± 0.09	99
	Parallel to keratin layers	4.2 ± 1.1	0.22 ± 0.08	19
Wet	Perpendicular to keratin layers	1.3 ± 0.6	0.04 ± 0.02	22
	Parallel to keratin layers	0.7 ± 0.3	0.02 ± 0.01	16

cells (corneocytes, keratinocytes and melanocytes (cells produce melanin)). Under wet conditions, both the modulus and hardness decrease significantly (1.3 GPa and 0.04 GPa in perpendicular, and 0.7 and 0.02 GPa in frontal plane). As mentioned earlier, this is due to the plasticizing effect of the water on the matrix proteins.

3.3.3. Pangolin scales

The pangolins have a large number of keratinous scales [21,295] covering their skin, the only known mammal with this adaptation [296]. The pangolins, also named scaly anteaters, are found naturally in tropical regions throughout Africa and Asia, and are famous for their distinctive protection mechanism: they curl up into a ball when threatened, with the sharp and plate-like overlapping scales projecting outwards, providing effective protection and extra defense (Fig. 67a, [297]). A coat of armor made of pangolin scales was presented to the King George III in 1820 (Fig. 67b, [298]). There are eight species of pangolins, and they are often divided into ground pangolins digging burrows and arboreal ones living in trees. Photos of an African Tree pangolin (*Manis tricuspis*) and a ground pangolin, Chinese pangolin (*Manis pentadactyla*) along with their corresponding scales are shown in Fig. 67c and d, respectively [299,300]. The projection directions of the overlapping scales are indicated by arrows on both pangolins, and the scale growth direction is shown by arrows on the scales.

The scales are reported to consist of both α-keratin and β-keratin [301]. The scales grow throughout the life of a pangolin just like hair, replacing the wear loss [302]. There are very few studies on the microstructure and mechanical properties of the scales. Fig. 68a shows the longitudinal ridges (indi-

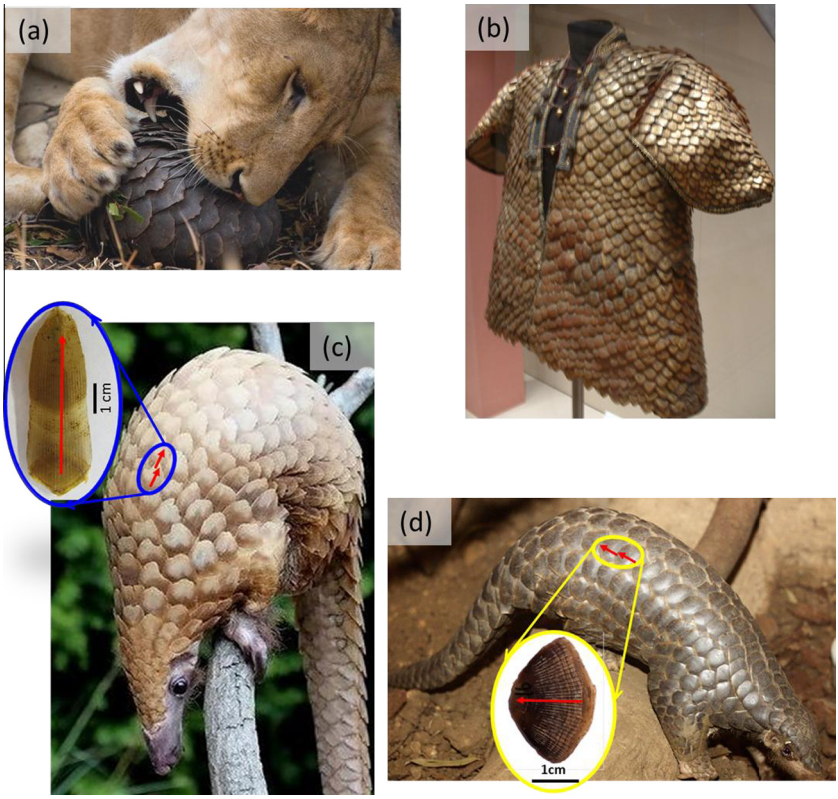

Fig. 67. (a) Protective function of the pangolin scales against lion attack [297]; (b) an armor coat made of pangolin scales [298]; (c) African Tree pangolin [299] (arrows indicate the overlapping direction) and the scale (arrow indicates the scale growth direction); (d) Chinese pangolin [300] (ground type) (arrows indicate the overlapping direction) and the scale (arrow indicates the scale growth direction).

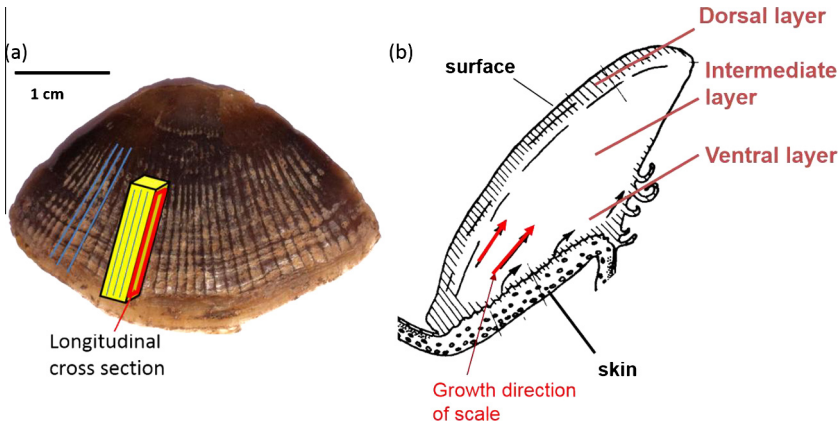

Fig. 68. (a) Single pangolin scale showing the longitudinal cross section (indicated by red rectangle drawn on the yellow solid). Blue lines indicate the ridges on external scale surface; (b) [21] schematic diagram of the longitudinal cross section of pangolin scale, showing the dorsal, intermediate and ventral layers.

cated as blue lines) on the external surface of the scales and the longitudinal cross section (indicated by red rectangle). Fig. 68b represents a schematic of the structure through the longitudinal cross section of a pangolin scale based on the histological structure and distribution of bound phospholipids, bound sulfhydryl groups and disulfide bonds [21]. The scale can be divided into three distinct regions through the cross section:

- the dorsal plate forms about one-sixth of the scale thickness;
- the intermediate plate, as the bulk of the scale, consists of less flattened cells;
- the ventral plate is only a few cells thick.

The distribution of chemical constituents in the pangolin scale is different from the reptilian type of scale [295]. Indeed, the development of scales in reptiles and pangolins are an example of convergent evolution.

From the optical micrograph of the cross section of a Chinese pangolin scale (Fig. 69a), the dorsal region shows fine structure with thin, wavy strip-like spacings that are parallel to the external surface, with dimensions about 20–40 μm long. The ventral region shows similar fine structure, which is nearly straight and parallel to the internal surface. The middle region, which constitutes the major part of cross section, exhibits elongated cellular morphology, which is tilted to the internal surface and with larger dimensions. The keratinocytes (fluoresce blue) show cross sectional profiles (Fig. 69b–d), indicating that the flattened cells pile up to form the scale. In the dorsal region, the flattened cells are arranged in layers (about 10 layers thick) parallel to wavy scale surface, with diameter about 20–50 μm and thickness 1–3 μm. The cells in ventral region show similar morphology and arrangement to those in outer region, except they are parallel to the flat inner surface. Keratinocytes in middle region are less flattened and have a random orientation. They exhibit larger dimension with diameter about 40–65 μm and thickness 6–10 μm.

Fig. 70 shows the scanning electron micrographs of cross sections of the Chinese pangolin scale, which consists of crossing lamellae (indicated by red arrows in Fig. 70a) and exhibit three regions, similar to nail keratin. The dorsal region shows lamellae with rigid rectangular shape which are wavy and parallel to the external surface with the spacing between rows of lamellae ~2 μm. In the middle, the lamellae are larger and not parallel to the scale surface, and exhibit cellular shape with the spacing between rows of lamellae about 3–8 μm. In the ventral region, the lamellar structure is similar to that of the dorsal regions, with the spacing of one lamellar row about 1.5–3 μm. According to the dimensions and morphology of the layered keratinocytes and lamellae, and referencing other keratinous tissues, it is suggested that each lamellar row is composed of one layer of flattened cells [155].

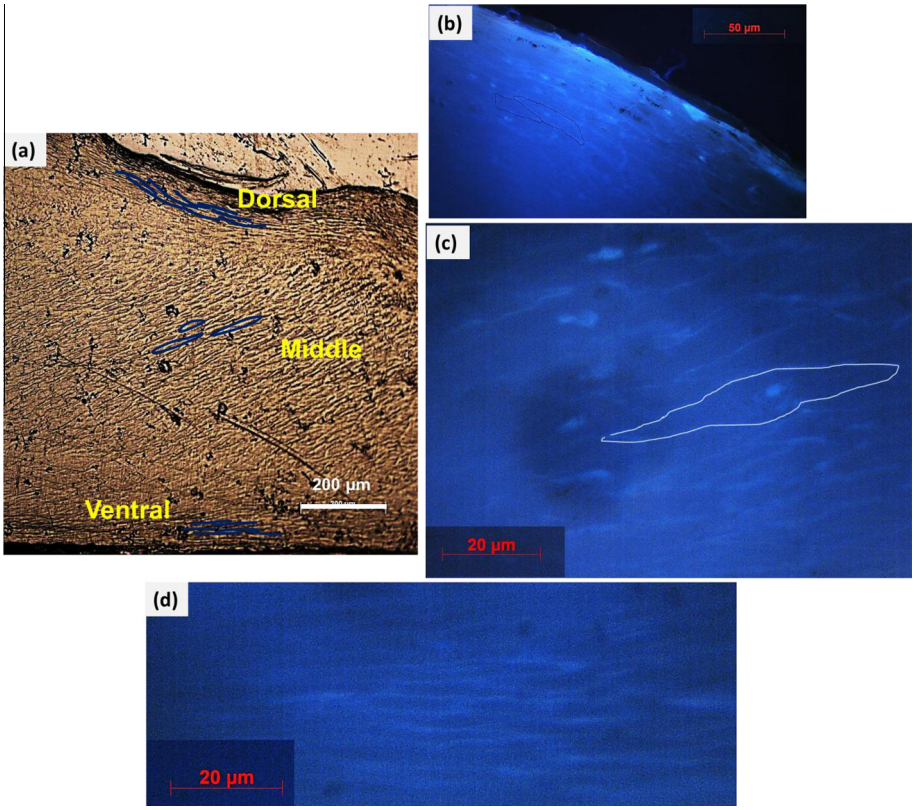

Fig. 69. Transverse cross section of a Chinese pangolin scale: (a) light micrograph, showing three regions with different morphologies (outer, middle, inner layers). Fluorescence micrographs of (b) outer layer, (c) near middle layer and (d) inner layer. Keratinocytes fluorescence blue under ultraviolet light. Cells in outer and inner layers appear more flattened, and smaller dimensions [155].

There are several reports on abrasive and tribological properties of pangolin scales, since pangolins are experts at burrowing and their scales need to have excellent abrasive resistance and sliding wear properties. In the dry tribological tests, a block-on-ring machine was used, in which scale were mounted in a steel block which is stationary with normal loading and the ring rotates to slide against the specimen (Fig. 71a) [303]. The wear rate increases first as the loading increases, and then decreases. Higher velocity leads expectantly to higher wear rate (Fig. 71b). The wear debris of scale specimens shows two types at both velocities: more blocky and flaky particles under a load due to the adhesion and stress fatigue, and more strip particles and fine powder under higher loads attributed to adhesion and the microploughing of the asperities on the ring surface. Fig. 72 shows that the friction coefficient, calculated from different loads and velocities, rises to a maximum value initially very fast (within 10 m of sliding distance), and gradually decreases to a steady value as sliding distance increases [303].

The tensile stress–strain curves and mechanical results on scales from African tree pangolin are shown in Fig. 73 [155]. They show typically two stages similar to other keratinous materials. First, there is an elastic region that is fairly linear, followed by a region with a gradually decreasing slope until failure is reached. This region is 'plastic' since it represents permanent deformation and damage to the structure. All curves at different strain rates exhibit monotonous increase and then fracture gradually without showing an obvious post-yield region, in contrast to some α-keratinous materials such as wool [148] and hoof wall [117]. With the increase of strain rate, the Young's modulus and ten-

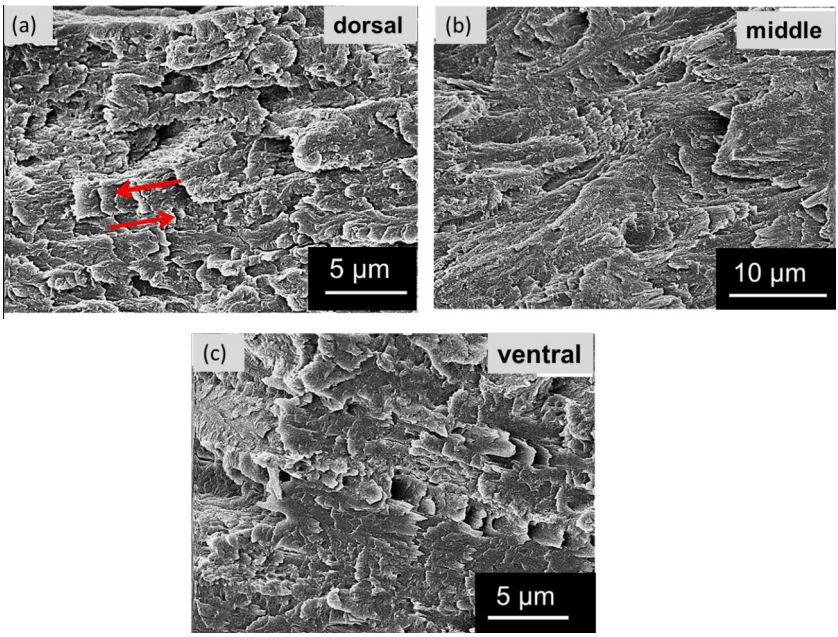

Fig. 70. Scanning electron micrographs of the crossed-lamellae structure along transverse cross section of Chinese pangolin scale: (a) dorsal layer; (b) middle layer; (c) ventral layer [155].

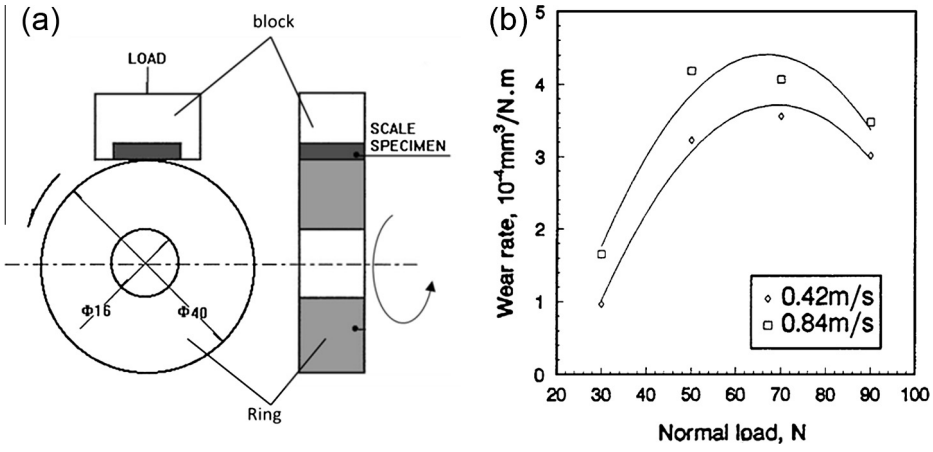

Fig. 71. (a) Schematic diagram of the block-on-ring wear test used to determine for wear rate (in volume per unit energy) of pangolin scales; (b) wear rate as a function of normal load for two sliding velocities sliding velocities: 0.42 and 0.84 m/s; as wear rate increases with velocity [303].

sile strength of pangolin scales increase linearly, from 1.2 to 1.5 GPa, and 68 to 109 MPa, respectively, but the tensile strain and toughness decrease, from 17% to 10%, and 8.8 to 6.8 MJ/m^3, respectively. This strain-rate dependence is also reported for other keratinous tissues, such as beaks that show pull-out fracture mode at low strain rate and brittle fracture at higher strain rate, equine hoof wall which show increasing Young's modulus and yield strength, total energy to breakage and maximum stress with increasing strain rate [117].

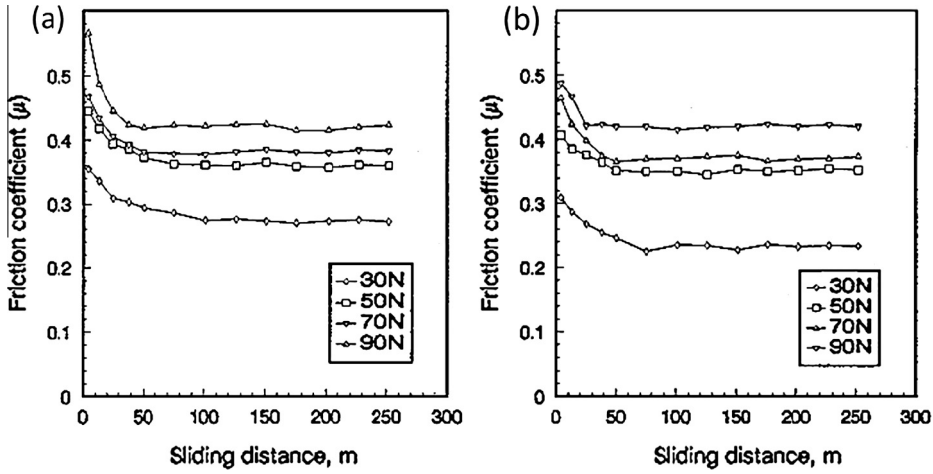

Fig. 72. Friction coefficients of pangolin scales sliding against iron ring as a function of sliding distance with different normal loads (30, 50, 70, and 90 N) at different sliding velocities (a) 0.42 m/s; (b) 0.84 m/s [303].

Fig. 74 shows the compressive stress–strain curves of pangolin scales along three loading orientations [155]. The highest compressive strength is along the scale thickness direction (128 MPa), followed by the loading orientation perpendicular to growth line direction (Perp-line) (113 MPa) and the loading orientation parallel to growth line direction (Para-line) (92 MPa). This is reasonable considering that the scales most frequently bear compressive force in the scale thickness direction exerted by teeth of the predators. After the plateau region, the compressive stress increases continuously. The Young's moduli for these three orientations are comparable, around 2.2 GPa, which is similar to other keratinous materials reported, e.g. quills of 1.9–2.3 GPa [179].

Hopkinson bar experiments (compression) on the scales yield a maximum stress of ~440 MPa along scale thickness direction at strain rates $\sim 3.5 \times 10^3\ s^{-1}$, quadruple that of quasi-static experiments. This high strain-rate sensitivity is in clear agreement with polymeric materials, to the class of which keratin belongs.

4. Bioinspired designs

Natural biological materials, exhibiting hierarchical structures and amazing functions with diverse morphologies, have been inspiring human beings since very early days. Indeed, humans have looked to nature for inspiration for more than 3000 years (since the Chinese first tried to make an artificial silk) [304]. The accuracy, efficacy, and ingenuity of biological systems have always been admired and thus investigated by scientists and engineers to develop new structures and technologies. This research area is developing rapidly, and the knowledge database has been growing exponentially. Fig. 75 illustrates the steep increase of publications and citations for 'bioinspired materials' since 1996 [305]. Keratinous materials stand out as they represent one of the toughest biological materials, serving as protective integuments in spite of purely protein constituents. Though few, keratinous materials have triggered increasing attention and great interest of researchers [12,306] to elucidate the relationship of structure and mechanical functions for the development of keratin-bioinspired materials/systems.

Bioinspiration is classified, as presented by Meyers and Chen [8], into traditional and molecular-based. In traditional bioinspiration, we try to copy the characteristics of biological materials using combinations of synthetic materials that are completely different but provide equivalent or similar mechanical response. The classic example is Velcro, based on the burrs of seeds but using synthetic materials to achieve the hooking–unhooking capability. Molecular-based bioinspiration is a much

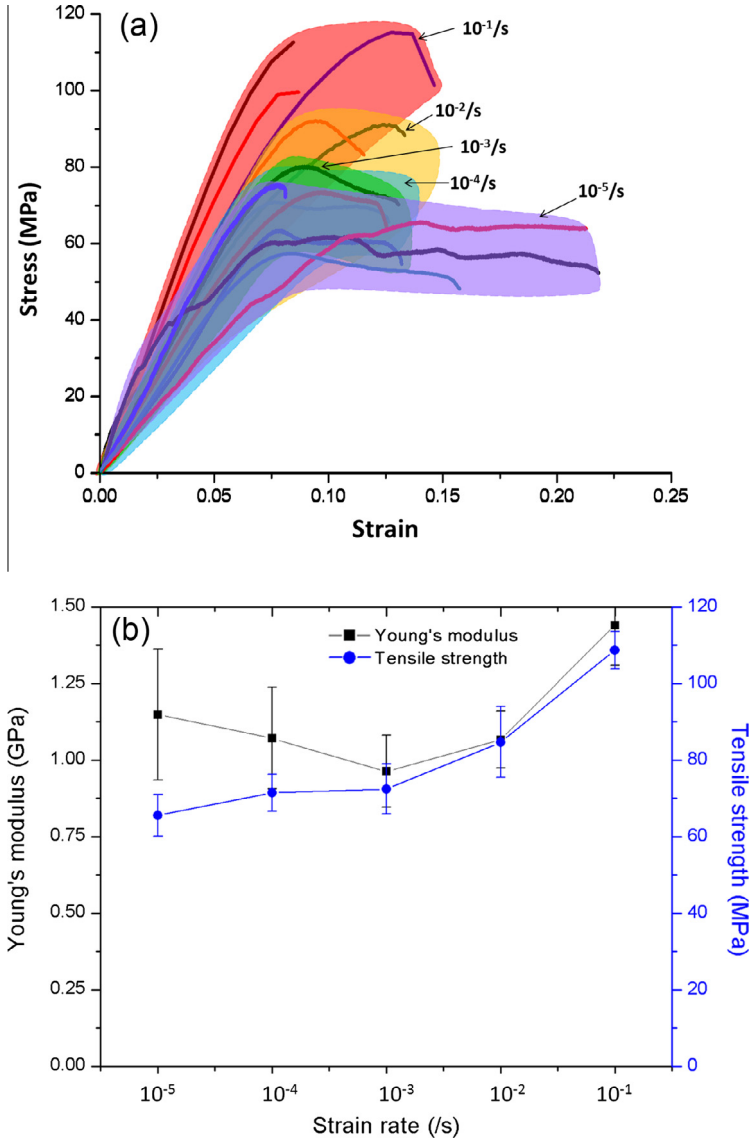

Fig. 73. Variation of tensile response of pangolin scales at different strain rates: (a) stress–strain curves grouped for each strain rate; (b) Young's modulus and tensile strength as function of strain rate (error bars represent the standard deviation at a confidence level of 90%).

more complex process because we mimic the molecular structure. The use of biological molecules to develop synthetic equivalents to the biological materials is a pursuit with significant potential pay-off. This requires fundamental biochemistry using recombinant DNA and protein engineering.

4.1. Traditional bioinspiration

It is suggested that the structure of hedgehog spine and porcupine quills [139,176] are optimally designed to resist buckling loads. Aluminum tubes filled with aluminum foam resisting compressive

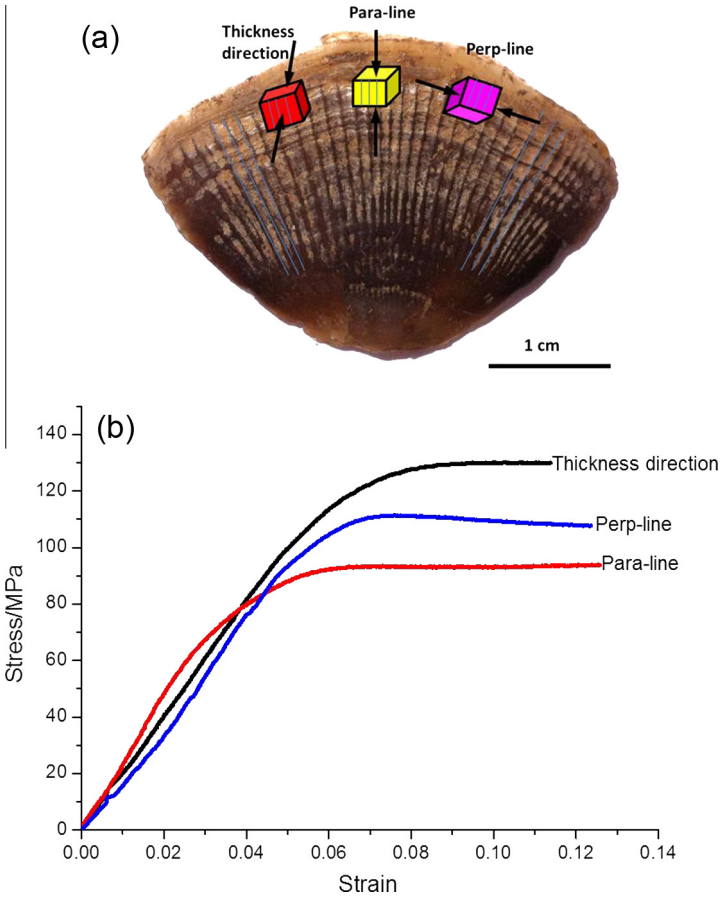

Fig. 74. Compressive response of pangolin scales: (a) compression specimens with three loading orientations (indicated by arrows; Para-line and Perp-line mean loading directions parallel and perpendicular to growth lines, respectively); (b) stress–strain curves along different orientations showing the same elastic modulus but differences in strength.

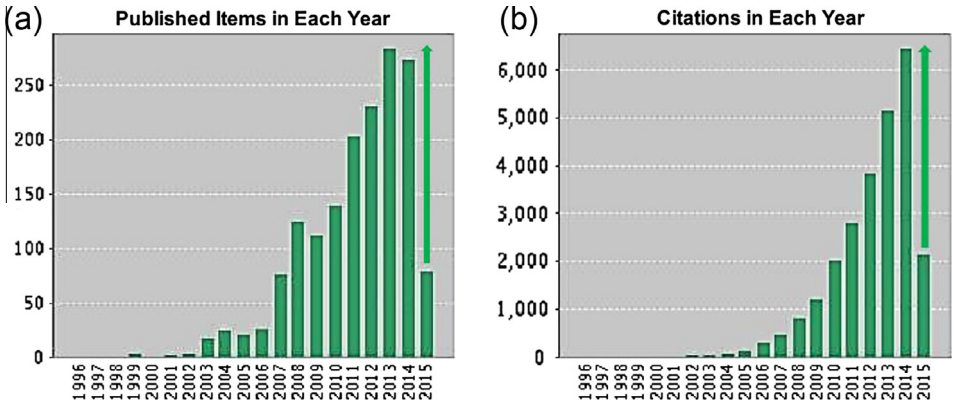

Fig. 75. Research status and trend with searched keyword "bioinspired materials" in Web of Science [305]: (a) published items in each year in recent 20 years; (b) citation in each year in recent 20 years.

loading and buckling analogous to the quill and spine, with similar structural design and reinforcement mechanism, were manufactured [307]. It is also reported that a novel composite with similar structure as horns and hooves, with a "forest" grown on the surface of laminate, exhibits enhanced mechanical properties [308]. Fig. 76a shows the schematic of processing the 3D composite that involves the growing of carbon nanotubes on the fiber cloth, stacking the matrix-infiltrated nanotube-grown fiber cloth and pressing the plates. Fig. 76b shows the structures of the SiC fabric cloth with and without the perpendicularly grown carbon nanotubes. Compared with the base composite (G_{IC} = 0.95 kJ/m^2), the nano-tube infiltrated composite showed large improvement of interlaminar fracture toughness, G_{IC} = 4.26 kJ/m^2, and this approaches the properties of the most fracture-resistant biological materials known, e.g. hoof wall with J_{crit} = 5.63 kJ/m^2 (critical J-integral value) at 53% RH [123,193].

The hierarchical architecture of feathers that provides optimal strength and weight has been mimicked to manufacture novel carbon fiber reinforced polymers with nanofibrous fractal interlayers as weight-saving composites [309]. Fig. 77a shows the how the feather fractal architecture is imitated: the rachis (mm), barbs (μm) and barbules and hooklets (nm) correspond to the carbon fiber, electrospun fibers and carbon nanotubes (CNT), respectively. The electrospun fibers with carbon nanotubes inside are the main interlayer reinforcement that enhance the ultimate strength of composite, which is compared with conventional laminated composite in Fig. 77b. The synthesis includes: (1) prepare

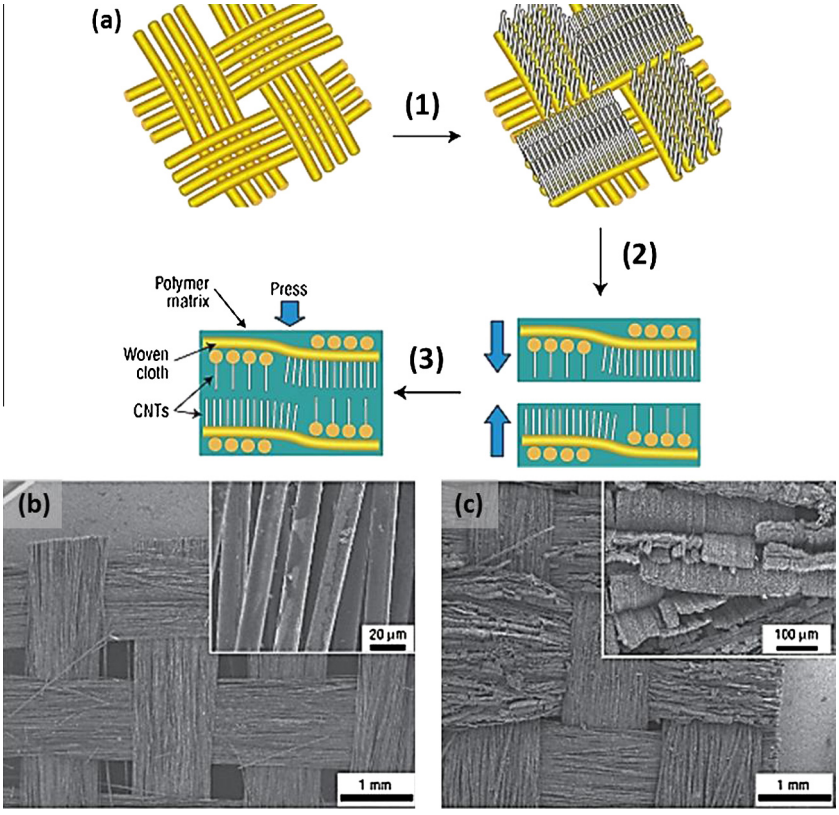

Fig. 76. (a) Processing for the manufacture of 3D carbon nanotubes (CNT) composite: (1) aligned CNTs grown perpendicular to SiC fiber cloth; (2) stacking of matrix-infiltrated (blue color) CNT-grown fiber cloth; (3) 3D nanocomposite plate fabrication by hand lay-up. (b) Scanning electron micrograph of the plain-weave SiC fabric cloth. Inset: higher magnification of the individual fibers. (c) Scanning electron micrograph of the cloth with CNTs grown perpendicularly on the surface. Inset: higher magnification image [308].

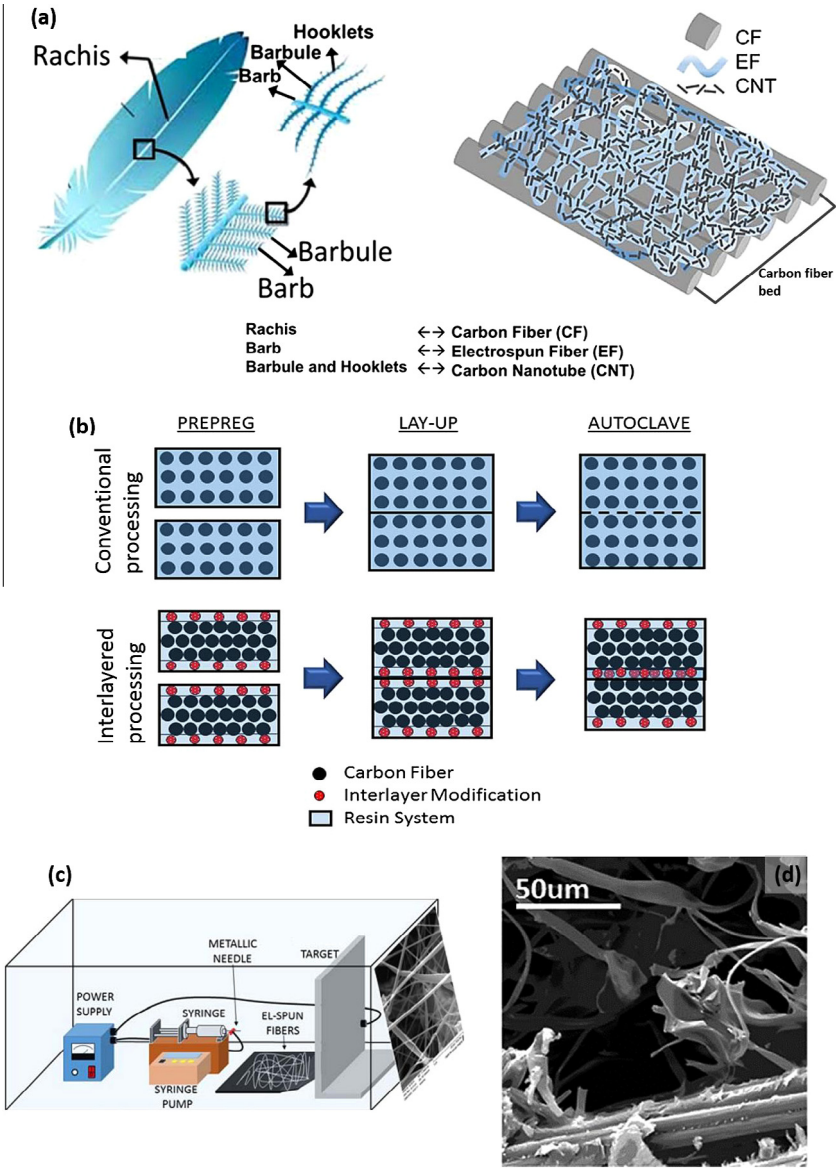

Fig. 77. The feather-inspired composite with electrospun fiber interlayers: (a) the feather fractal architecture of rachis, barbs and barbules ranging from macro-, to micro- and to nano-scales and the inspired the structure: carbon fibers form carbon fiber bed, on which carbon nanotube reinforced fibers are electrospun; (b) processing of conventional laminate composite and interlayered laminate structure; (c) electrospinning apparatus with the electrospun fibers on the right; (d) scanning electron micrograph of flexural fractured surface of the composite at the carbon nanotube reinforced electrospun fiber interlayer [309].

polymer solution for electrospun fibers: cellulose acetate in acetone solution with CNT added; (2) obtain the layers: the CNT polymer solution is used to electrospin fibers (shown in Fig. 77c) on a target which is the carbon fiber bed; (3) form the composite: consolidate the layers through lay-up within resin (vacuum and 180 °C). Fig. 77d shows the fractured morphology of the CNT reinforced electrospun fiber interlayer within the composite. The feather-inspired composite achieves higher mechan-

ical properties than conventional carbon fiber reinforced polymers: the storage modulus increased 85%, the flexural strength (307 ± 32 MPa) and modulus (38 ± 2 GPa) increased 51% and 54%, respectively, and the Mode II fracture toughness (892 ± 90 J m^{-2}) increased 165%. Taking into consideration the weight saving (specific weight 1.62 ± 0.02 g cm^{-3}, 6% reduction than conventional carbon fiber reinforced polymers) together, this CNT reinforced electrospun fiber interlayered composite demonstrates the potential for applications in several industry, such as automobiles, aerospace, marine, and sports [309].

The North American porcupine quills show interesting features that can be applied to the development of bio-inspired medical devices [310]. The quills have microscopic backward-facing barbs at the conical black tip (Fig. 78a–c), which enables an easy penetration but strong tissue adhesion through the deployment and bending of barbs during removal (Fig. 78d). Compared with barbless quill (experimentally removed barbs) and African porcupine quill (naturally barbless), the barbed quill shows significant lower penetration force and work of penetration, which is needed for some medical devices

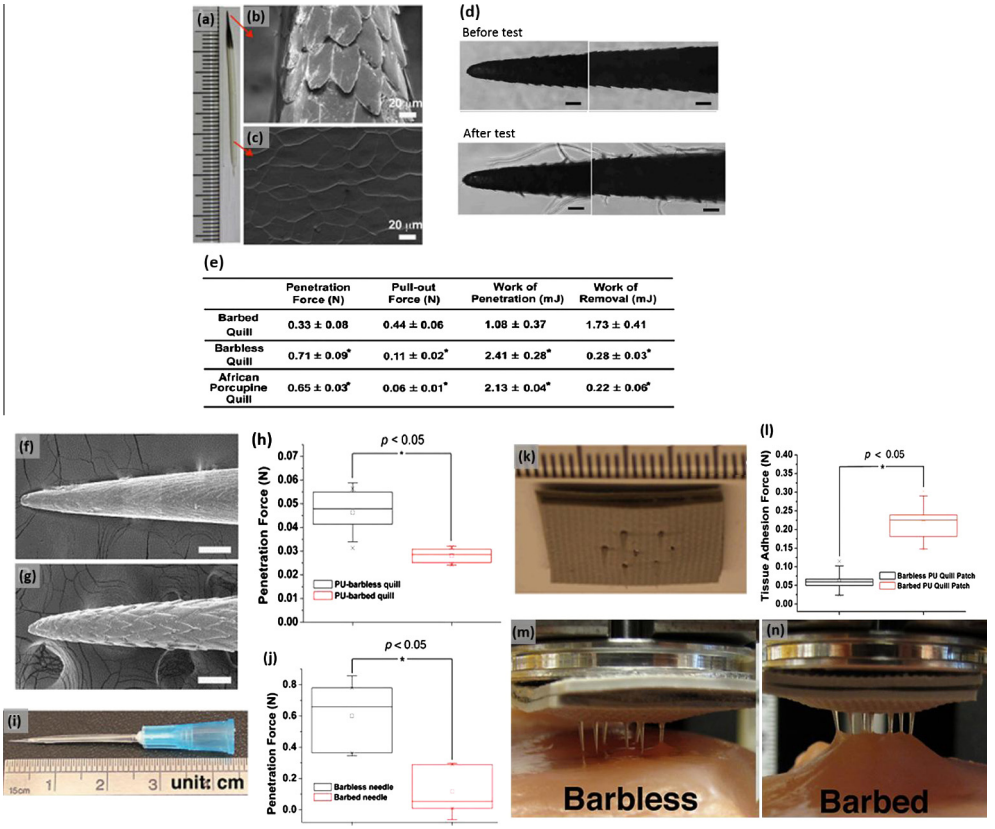

(e)

	Penetration Force (N)	Pull-out Force (N)	Work of Penetration (mJ)	Work of Removal (mJ)
Barbed Quill	0.33 ± 0.08	0.44 ± 0.06	1.08 ± 0.37	1.73 ± 0.41
Barbless Quill	0.71 ± 0.09*	0.11 ± 0.02*	2.41 ± 0.28*	0.28 ± 0.03*
African Porcupine Quill	0.65 ± 0.03*	0.06 ± 0.01*	2.13 ± 0.04*	0.22 ± 0.06*

Fig. 78. The North American porcupine quills and the bio-inspired designs: (a) North American porcupine quill; scanning electron micrographs of (b) the quill tip showing the deployable barbs and (c) quill base showing the smooth scale-like surface; (d) optical micrographs of porcupine quills before penetration and after removal; note the deployment and bending of the barbs; (scale bars: 100 μm) (e) experimental results of barbed quill, barbless quill and African porcupine quill from penetration/removal tests (mean ± SD); scanning electron micrographs of the synthetic quills using replica molding and polyurethane (f) PU-barbless quill and (g) PU-barbed quill (scale bars: 100 μm); (h) the forces required to penetrate barbed and barbless PU quills into muscle tissue to 4 mm depth; (i) the fabricated quill-inspired needle; (j) the forces required to penetrate barbed and barbless quill-inspired needles into a human skin model; (k) the fabricated quill-inspired patch consisting of seven PU quills; (l) adhesion forces from barbless and barbed PU quill patches; the interacting with muscle tissue of (m) barbless PU quill patch and (n) barbed PU quill patch during retraction [310].

(e.g. needles, vascular tunnelers), but higher pull-out force and work of removal, which is the important property of tissue adhesives (Fig. 78e). Fig. 78f and g shows synthetic replica molded polyurethane (PU)-barbed quill that reproduces the surface topography of the North American porcupine quills and PU-barbless quill, and penetration tests reveal that the barbed quills show 35% less force (Fig. 78h). Prototypic hypodermic needles with barbs were fabricated, and the PU-barbed needle shows 80% less penetration force compared with the PU-barbless needle (Fig. 78i and j). The high tissue adhesion of the quills is also imitated through fabricating prototypic quill-mimatic patches that have replica molded PU-barbed and PU-barbless quills (Fig. 78k). The PU-barbed quill patch shows significantly higher adhesion force and interaction with the tissue than the PU-barbless quill patch (Fig. 78l–n), which is useful for the development of mechanically interlocking tissue adhesives [310].

Whale baleen has inspired a self-cleaning filter system, the Baleen Filter patented by the University of South Australia [311,312], for industrial wastewater filtration. This technology imitates how whales collect organisms through their baleen and how they keep the baleen clean and free from long-term deposits by combining a sweeping action of the tongue and the reversing of water flows. The Baleen Filter utilizes fine sieves, which are made from stainless steel or polymers and use a special woven wire screen-mesh in a planar form, which can separate organic and inorganic matter from waters to less than even 5 μm. The successful trials across industries, such as meat and by-products, food and dairy, mining and municipal, have demonstrated that the Baleen filter can be used in traditionally difficult applications, and reliably and cost efficiently separate matter, whether solid, semi-aqueous or immiscible, from wastewater streams with suspended solids and fat in high or variable concentrations [313].

There are a number of products having similar mechanism as or inspired by the pangolin scales which function as flexible dermal armor. The Dragon Skin® is a type of ballistic vest made by Pinnacle Armor, using the design of circular overlapping discs similar as the pangolin scales. Fig. 79a shows an X-ray of Dragon Skin body armor [314]. The overlapping discs made of silicon carbide create a highly flexible vest and are intended to resist bullet penetration. Another product that imitates the pangolin scales is the Pangolin backpack by Cyclus Manufacture® [315], seen in Fig. 79b. The Pangolin backpack has large, hard overlapping layers made of inner tubes of recycled tire, and each layer closure is retractable due to magnets. It is water resistant, and provides shock absorption through adjustable padded straps and full comfort by airflow back channels, durable and protective with personal style.

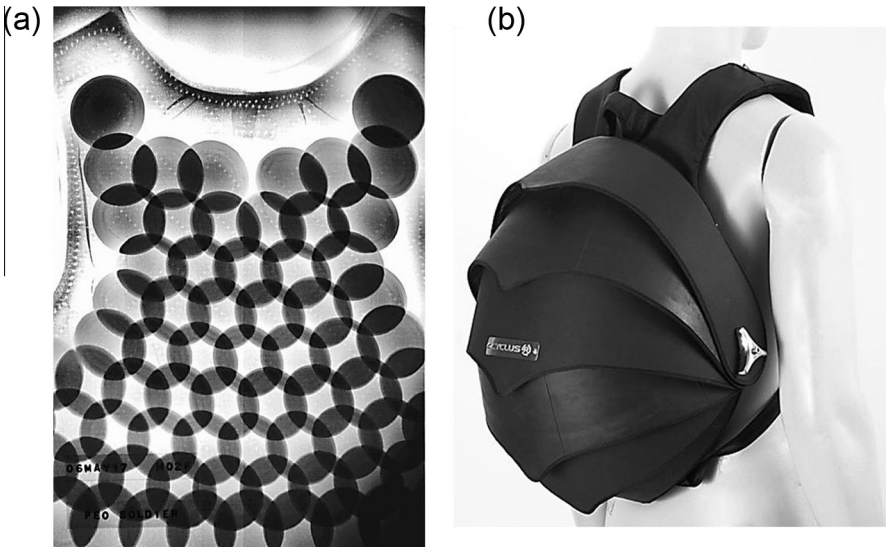

Fig. 79. Examples of applications using concepts similar to nature: (a) X-ray of Dragon Skin body armor [314]; (b) Pangolin backpack showing the overlapping layers connected by magnets resembling an armored pangolin [315].

The deployment of hagfish slime thread skeins is interesting since the unraveling from a 150 μm-long bundle to a 100 times longer thread is completed less than a second, and is therefore inspiring [124]. The deployment process has been attributed (Section 3.1.8) to the mucin strands interacting with unraveled slime threads to yield a complex network capable of the viscous entrainment of seawater [124,216]. It is proposed that the mucin strands are capable of transmitting hydrodynamic forces to and exerting tensile forces on the skeins, and thus unravel the skeins. This is believed to be a unique mechanism in biology and may lead to novel technologies for industrial processes to transmit hydrodynamic forces to microscale particles that would typically be immune to such forces [124].

4.2. Molecular-based bioinspiration

The egg capsules of the oviparous gastropods (*Pugilina cochlidium* and *B. canaliculatus*) are keratin-like biopolymers that display outstanding mechanical properties. This is to a large extent due to the $\alpha \leftrightarrow \beta$ reversible transformation that occurs on tension loading, as explained in Section 3.1.9. There is no synthetic polymer equivalent and therefore Miserez and co-workers [9] have been working at recreating the structure by using advanced biology techniques and biomimetic self-assembly of molecules. Fibrin, myosin II, keratin, and the keratin-like proteins in the egg capsules have intermediate filaments which can undergo the $\alpha \rightarrow \beta$ transformation. Thus, the studies on the egg capsules have direct relevance for keratins because the same methodology can be used.

The initial stages are to self-assemble the peptides into nano-fibrils with excellent control. This was done by Banwell et al. [316] who produced coiled coils synthetically. These short nanofibrils were used to construct hydrogel scaffolds in tissue engineering applications. However, the egg capsule proteins exhibit a Young's modulus of 50–100 MPa, which is orders of magnitude larger than hydrogels. They can undergo reversible strains of up to 170% and this leads to an extraordinary energy absorption capability. The coiled coil domains in the intermediate filaments (IFs) vary in length from 10 to 50 nm and in diameter from 7 to 11 nm. Recent efforts by Fu et al. [317] have yielded much larger coiled coil domains of α protein which can, on extension, transform into beta sheet domains.

5. Conclusions and critical assessment of field

Keratin represents one of the toughest biological materials, serving as an effective protective integument (surface layer), although it is purely composed of proteins. It shows great potential for novel bioinspired designs, in which a thorough understanding of the biochemistry, structure, and mechanical properties is a priority. We have reviewed here the principal studies on keratins and keratinous materials incorporating knowledge from biology, materials science and engineering. The following conclusions can be drawn:

- Keratins are high-sulfur content and filament-forming proteins; keratinous materials are formed by piled keratinized epidermal cells. They can be classified as α-keratin (stratum corneum, wool, hair, nails, hooves, horns, hagfish slime, and whale baleen) and β-keratins (feathers, claws and beak rhamphotheca of birds, and scales and claws of reptiles). Some are based on both α- and β-keratins (reptilian epidermis and pangolin scales).
- Keratin synthesis proceeds by the protein chains remaining attached to the mRNA–polysome complex until completed. In α-keratinous materials, the synthesis of proteins forming the intermediate filaments (IFs) and matrix follows different time courses, while in β-keratinous materials, the proteins increase in a coordinated fashion. The epidermal cells synthesize keratins by moving directionally; they die and organize into specific arrangements filled with keratin, forming keratinous materials.
- Both α- and β-keratinous materials show a fine filament-matrix structure: ~7 nm diameter IFs embedded in matrix for α-keratin, and 3–4 nm diameter β-keratin filaments embedded in matrix for β-keratin. The α-keratin IFs are based on α-helical chain structure while β-keratin filaments based on β-pleated sheets.

- Keratinous materials exhibit complex hierarchical structures progressing in the spatial scale as: (a) polypeptide chain structure at nanoscale; (b) filament-matrix structure at nanoscale; (c) specifically organized keratinized cells and lamellae, fiber or layered structure at microscale; (d) solid, tubular and intertubular material, compact sheath over porous core, sandwich and thread structures at mesoscale or macroscale.
- Mechanical properties of α-keratin have been evaluated via a qualitative two-phase model: crystalline IFs embedded in an amorphous matrix. Under tension the α-helices change into β-pleated sheets. Three regions in tensile stress–strain curve of α-keratin can be distinguished: a linear Hookean where α-helices are stretched, a yield region with little increase in stress, in which the α-coiled coils unravel and refold into β sheets, and a post-yield region with increasing slope. The reversible $\alpha \leftrightarrow \beta$ transition in whelk egg capsules was found to be internal energy-driven and not entropy-induced.
- Keratinous tissues exhibit viscoelastic behavior and show an initial linear region followed by a plastic region. This enables the functions of both sustaining external forces and absorbing energy. The viscoelasticity leads to mechanical properties sensitive to strain rate: higher Young's modulus and strength but lower breaking strain with increasing strain rate. This is important since the tissues need to be stiffer and stronger to sustain rapid loading or impact. The possible changes in fracture mode and fracture toughness are relevant to specific tissues.
- The mechanical responses of α- and β-keratinous materials are highly dependent on water content: increasing humidity decreases the stiffness and strength. This has been attributed largely to the water–protein interactions within matrix proteins which reduce the bonding forces and increase segmental mobility: water may act as a plasticizer between chains, affect and/or replace the hydrogen bonds within matrix protein chains, and form a three-dimensional keratin–water molecule network. The water molecules may also affect the hydrogen bonds within the matrix-free IFs (in the case of the hagfish slime threads).
- The hierarchical structure renders a wide range of mechanical properties, e.g. the Young's modulus ranging from ~10 MPa of stratum corneum to ~2.5 GPa of feathers, fracture toughness ranging 5.6–22.8 kJ/m^2 for hooves and the work to fracture in the range 10–80 kJ/m^2 for horns. They are able to serve a variety of functions including diffusion barrier, buffering external attack, energy-absorption, impact-resistance, piercing opponents, withstanding repeated stress and aerodynamic forces, resisting buckling and penetration.

The diverse hierarchical structures and functions of keratinous materials provide useful insights into the development of new bioinspired structures. Although a significant amount of research has been conducted, our knowledge is far from sufficient for a complete and accurate understanding; some areas still are nebulous and inadequate. The following presents corresponding assessments and outlooks in keratin research:

- How biological components assemble into tough and light-weight structures in nature offers key design ideas for engineering but is often overlooked by materials researchers. Either collaboration with colleagues from biology or enhancing the biological knowledge of materials researchers is required.
- In contrast with α-keratinous materials, β-keratinous materials are poorly studied, including their gene sequence, molecular assembly, biosynthesis, hierarchical structure and mechanical behaviors; there have not been any mechanical models or in-depth studies on mechanism of hydration sensitivity for β-keratin. This represents an interesting field that deserves investigation to explore and discover.
- For the hierarchical structure inherent in keratinous materials, both the structural detail at each level and the connections between different levels are of great importance, and the latter have not received as much attention as the former, e.g. how the filaments and matrix pack in the keratinized cells and how the cells organize to form lamellar/fibrous/layered structures.
- The study of the mechanical response of individual IFs of α-keratins and β-keratin filaments at the nanoscale has not been sufficient, and we do not have a complete picture for the orientation, packing and volume fractions of the ordered filaments in different keratinous materials and of their

mechanical roles. This would require us to make best use of the experimental, analytical and computational tools available to materials researchers.

- There are very few studies on the constitutive behavior of the composites (IFs/β-keratin filaments and the amorphous matrix); it is very important to understand the relation between morphology and configuration of components and functions and to predict material properties.
- It would be highly desirable to establish whether the basic constitutive model developed for keratin-like proteins in gastropod egg capsules can be extended to other keratinous materials undergoing the $\alpha \rightarrow \beta$ transition, such as hair, wool, and whale baleen. The latter have a yield stresses vastly superior to the egg capsule and the applicability of the analysis needs to be verified.
- In comparison with other biological materials (e.g. shell, skin, scales, bones), the evaluation of the fracture behavior and impact resistance of keratinous materials is in an initial stage; a great research effort in this area is forseen since they are among the most fracture-resistant biological materials. More systematic toughness testing and evaluation of the toughening mechanisms for keratinous materials would be highly desirable.
- The application of materials knowledge of keratins to the design of new structures is a vast and ambitious undertaking, in which carbon nanotubes, graphene, and other synthetic fibers can be combined with polymeric matrices. This is an exciting field with many possibilities.
- Using genetic and protein engineering, we are starting to be able to reproduce keratin-like materials at the molecular level. This work is based on coiled-coil recombinant proteins and requires DNA sequencing. Thus, molecular biomimicry of keratin materials is feasible, the goal being to reproduce the outstanding mechanical properties achieved through the $\alpha \rightarrow \beta$ transition.

Acknowledgements

Professors David Parry, John Gosline and Lorenzo Alibardi kindly discussed and offered valuable information on molecular structure of beta-keratin (corneous beta-proteins) and α-keratin. We thank Profs. Ali Miserez, Nanyang Technological U., Singapore, and Po-Yu Chen, National Tsinghua U., Taiwan, for their critical reading and many suggestions to manuscript and gratefully acknowledge financial support from a Multi-University Research Initiative through the Air Force Office of Scientific Research (AFOSR-FA9550-15-1-0009). We sincerely thank the San Diego Natural History Museum for providing pangolin scales for our research. Prof. K.S. Vecchio provided assistance in the dynamic split-Hopkinson bar experiments (providing a strain rate of $4 \times 10^3\ s^{-1}$), and Professor Yu Qiao helped us to perform tensile tests on fingernails.

References

[1] Sarikaya M. An introduction to biomimetics: a structural viewpoint. Microsc Res Tech 1994;27(5):360–75.
[2] Srinivasan AV, Haritos GK, Hedberg FL. Biomimetics: advancing man-made materials through guidance from nature. Appl Mech Rev 1991;44(11):463.
[3] Mayer G, Sarikaya M. Rigid biological composite materials: structural examples for biomimetic design. Exp Mech 2002;42(4):395–403.
[4] Baer E, Hiltner A, Morgan RJ. Biological and synthetic hierarchical composites. Phys Today 1992;45(10):60.
[5] Meyers MA, Chen P-Y, Lin AY-M, Seki Y. Biological materials: structure and mechanical properties. Prog Mater Sci 2008;53(1):1–206.
[6] Meyers MA, McKittrick J, Chen P-Y. Structural biological materials: critical mechanics–materials connections. Science 2013;339(6121):773–9.
[7] Vincent JFV. Structural biomaterials. revised ed. Princeton University Press; 1990.
[8] Meyers MA, Chen P-Y. Biological materials science. Cambridge, UK: Cambridge University Press; 2014.
[9] Miserez A, Weaver C, Chaudhuri O. Biological materials and molecular biomimetics – filling up the empty soft materials space for tissue engineering applications. J Mater Chem B: Mater Biol Med 2015;3(1):13–24.
[10] Ashby MF, Gibson LJ, Wegst U, Olive R. The mechanical properties of natural materials. I. Material property charts. Proc R Soc A: Math Phys Eng Sci 1995;450(1938):123–40.
[11] Coulombe PA, Omary MB. 'Hard' and 'soft' principles defining the structure, function and regulation of keratin intermediate filaments. Curr Opin Cell Biol 2002;14(1):110–22.
[12] McKittrick J, Chen PY, Bodde SG, Yang W, Novitskaya EE, Meyers MA. The structure, functions, and mechanical properties of keratin. JOM 2012;64(4):449–68.
[13] Wegst UGK, Ashby MF. The mechanical efficiency of natural materials. Philos Mag 2004;84(21):2167–86.
[14] Szewciw LJ, de Kerckhove DG, Grime GW, Fudge DS. Calcification provides mechanical reinforcement to whale baleen alpha-keratin. Proc Biol Sci 2010;277(1694):2597–605.

[15] Mercer EH. Keratin and keratinization: an essay in molecular biology. Pergamon; 1961.
[16] Fraser RDB, MacRae TP, Rogers GE. Keratins: their composition, structure and biosynthesis. Charles C Thomas; 1972.
[17] Feughelman M. Mechanical properties and structure of alpha-keratin fibers: wool, human hair and related fibers. University of New South Wales Press; 1997.
[18] Miserez A, Guerette PA. Phase transition-induced elasticity of α-helical bioelastomeric fibres and networks. Chem Soc Rev 2013;42(5):1973–95.
[19] Herrmann H, Aebi U. Intermediate filaments: molecular structure, assembly mechanism, and integration into functionally distinct intracellular scaffolds. Annu Rev Biochem 2004;73:749–89.
[20] Schweizer J, Bowden PE, Coulombe PA, Langbein L, Lane EB, Magin TM, et al. New consensus nomenclature for mammalian keratins. J Cell Biol 2006;174(2):169–74.
[21] Spearman RIC. On the nature of the horny scales of the pangolin. J Linn Soc Zool 1967;46(310):267–73.
[22] Astbury WT, Street A. X-ray studies of the structure of hair, wool, and related fibres. I. General. Philos Trans R Soc Lond A 1932;230(681–693):75–101.
[23] Astbury WT, Woods HJ. X ray studies of the structure of hair, wool, and related fibres. II. The molecular structure and elastic properties of hair keratin. Philos Trans R Soc Lond B 1934;114(788):314–6.
[24] Fraser RDB, MacRae TP, Parry DAD, Suzuki E. The structure of beta-keratin. Polymer 1969;10:810–26.
[25] Fraser RDB, MacRae TP. The structure of α-keratin. Structure 1973;14(September):61–7.
[26] Fraser RDB, Parry DAD. The structural basis of the filament-matrix texture in the avian/reptilian group of hard β-keratins. J Struct Biol 2011;173(2):391–405.
[27] Parry DAD. Personal communications; 2014.
[28] Lodish H, Berk A, Zipursky SL, Matsudaira P, Baltimore D, Darnell J. Molecular cell biology. 4th ed. New York: W.H. Freeman and Company; 2000.
[29] Bear RS, Rugo HJ. The results of X-ray diffraction studies on keratin fibers. Ann N Y Acad Sci 1951;53(3):627–48.
[30] Busson B, Briki F, Doucet J. Side-chains configurations in coiled coils revealed by the 5.15 – a meridional reflection on hard alpha-keratin X-ray diffraction patterns. J Struct Biol 1999;125(1):1–10.
[31] Chen PY, McKittrick J, Meyers MA. Biological materials: functional adaptations and bioinspired designs. Prog Mater Sci 2012;57(8):1492–704.
[32] Giroud A, Leblond CP. The keratinization of epidermis and its derivatives, especially the hair, as shown by X-ray diffraction and histochemical studies. Ann N Y Acad Sci 1951;53(3):613–26.
[33] Alibardi L, Dalla Valle L, Nardi A, Toni M. Evolution of hard proteins in the sauropsid integument in relation to the cornification of skin derivatives in amniotes. J Anat 2009;214(4):560–86.
[34] Strasser B, Mlitz V, Hermann M, Rice RH, Richard A. Evolutionary origin and diversification of epidermal barrier proteins in amniotes; 2014.
[35] Squire J, Vibert PJ, Elliott A. Fibrous protein structure. San Diego, US: Academic Press; 1987.
[36] Gillespie JM. The proteins of hair and other hard α-keratins. In: Goldman RD, Steinert PM, editors. Cellular and molecular biology of intermediate filaments. US: Springer; 1990. p. 95–128.
[37] Alibardi L, Dalla Valle L, Toffolo V, Toni M. Scale keratin in lizard epidermis reveals amino acid regions homologous with avian and mammalian epidermal proteins. Anat Rec – Part A Discov Mol Cell Evol Biol 2006;288(7):734–52.
[38] Jones LN, Simon M, Watts NR, Booy FP, Steven AC, Parry DAD. Intermediate filament structure: hard α-keratin. Biophys Chem 1997;68(1–3):83–93.
[39] Parry DAD. Hard α-keratin intermediate filaments: an alternative interpretation of the low-angle equatorial X-ray diffraction pattern, and the axial disposition of putative disulphide bonds in the intra- and inter-protofilamentous networks. Int J Biol Macromol 1996;19(1):45–50.
[40] Nelson DL, Cox MM. Lehninger principles of biochemistry. 5th ed. New York: W.H. Freeman and Company; 2008.
[41] Crick FHC. Is α-keratin a coiled coil? Nat Publ Gr 1952;170:882–3.
[42] Crick FHC. The packing of α-helices: simple coiled-coils. Acta Crystallogr 1953;6:689–97.
[43] Pauling L, Corey RB, Branson HR. The structure of proteins; two hydrogen-bonded helical configurations of the polypeptide chain. Proc Natl Acad Sci USA 1951;37(4):205–11.
[44] McMurry J, Fay R. Biochemistry. In: Chemistry. Pearson Prentice Hall; 2003.
[45] Voet D, Voet JG, Pratt CW. Biochemistry: life at the molecular level. 3rd ed. New York: John Wiley & Sons; 2008.
[46] Chou C-C, Buehler MJ. Structure and mechanical properties of human trichocyte keratin intermediate filament protein. Biomacromolecules 2012;13(11):3522–32.
[47] Fraser RDB, MacRae TP, Sparrow LG, Parry DAD. Disulphide bonding in α-keratin. Int J Biol Macromol 1988;10(2):106–12.
[48] Lee C-H, Kim M-S, Chung BM, Leahy DJ, Coulombe PA. Structural basis for heteromeric assembly and perinuclear organization of keratin filaments. Nat Struct Mol Biol 2012;19(7):707–15.
[49] Strelkov SV, Herrmann H, Geisler N, Wedig T, Zimbelmann R, Aebi U, et al. Conserved segments 1A and 2B of the intermediate filament dimer: their atomic structures and role in filament assembly. EMBO J 2002;21(6):1255–66.
[50] Chernyatina AA, Nicolet S, Aebi U, Herrmann H, Strelkov SV. Atomic structure of the vimentin central-helical domain and its implications for intermediate filament assembly. Proc Natl Acad Sci 2012;109(34):13620–5.
[51] Moll R, Franke WW, Schiller DL. The catalog of human cytokeratins: patterns of expression in normal epithelia, tumors and cultured cells. Cell 1982;31(November):11–24.
[52] Tseng SC, Jarvinen MJ, Nelson WG, Huang JW, Woodcock-Mitchell J, Sun TT. Correlation of specific keratins with different types of epithelial differentiation: monoclonal antibody studies. Cell 1982;30(2):361–72.
[53] Wu YJ, Parker LM, Binder NE, Beckett MA, Sinard JH, Griffiths CT, et al. The mesothelial keratins: a new family of cytoskeletal proteins identified in cultured mesothelial cells and nonkeratinizing epithelia. Cell 1982;31(3 Pt 2):693–703.
[54] Moll R, Divo M, Langbein L. The human keratins: biology and pathology. Histochem Cell Biol 2008;129(6):705–33.
[55] Dowling LM, Crewther WG, Parry DAD. Secondary structure of component 8c-1 of alpha-keratin. An analysis of the amino acid sequence. Biochem J 1986;236(3):705–12.
[56] Fraser RDB, MacRae TP, Parry DAD, Suzuki E. Intermediate filaments in α-keratins. Proc Natl Acad Sci USA 1986;83(5):1179–83.

[57] Fraser RDB, Parry DAD. Molecular packing in the feather keratin filament. J Struct Biol 2008;162(1):1–13.
[58] Lewis DM, Rippon JA, editors. The coloration of wool and other keratin fibres. John Wiley; 2013.
[59] Steinert PM, Rice RH, Roop DR, Trus BL, Steven AC. Complete amino acid sequence of a mouse epidermal keratin subunit and implications for the structure of intermediate filaments. Nature 1983;302(5911):794–800.
[60] Steinert PM, Parry DAD. Intermediate filaments: conformity and diversity of expression and structure. Annu Rev Cell Biol 1985;1:41–65.
[61] Crewther WG, Dowling LM. 55-Effects of chemical modifications on the physical properties of wool: a model of the wool fiber. J Text Inst Trans 1960;51(12):T775–91.
[62] Harding HW, Rogers GE. ε-(γ-Glutamyl)lysine cross-linkage in citrulline-containing protein fractions from hair. Biochemistry 1971;10(4):624–30.
[63] Milligan B, Holt LA, Caldwell JB. The enzymic hydrolysis of wool for amino acid analysis. Appl Poly Symp 1971;18:113–25.
[64] O'Donnell IJ, Thompson EOP. Studies on oxidized wool VI. Interactions between high and low-sulfur proteins and their significance in the purification of extracted wool proteins. Aust J Biol Sci 1962;15:740–56.
[65] O'Donnell IJ, Thompson EOP. Studies on reduced wool IV. The isolation of a major component. Aust J Biol Sci 1964;17:973–8.
[66] Alexander P, Earland C. Structure of wool fibers. Isolation of an α- and β-protein in wool. Nature 1950;166:396–7.
[67] Swan JM. Thiols, disulphides and thiosulphates: some new reactions and possibilities in peptide and protein chemistry. Nature 1957;180:643–5.
[68] Goddard DR, Michaelis L. A study on keratin. J Biol Chem 1934;106(2):605–14.
[69] Harrap BS, Woods EF. Soluble derivatives of feather keratin. 1. Isolation, fractionation and amino acid composition. Biochem J 1964;92(1):8–18.
[70] Gennadios A. Protein-based films and coatings. CRC Press; 2002.
[71] Holt BLA, Milligan B, Roxburgh CM. Aspartic acid, asparagine, glutamic acid, and glutamine contents of wool and two derived protein fractions. Aust J Biol Sci 1971;24(3):509–14.
[72] Thompson EOP, O'Donnell IJ. Studies on reduced wool I. The extent of reduction of wool with increasing concentrations of thiol, and the extraction of proteins from reduced and alkylated wool. Aust J Biol Sci 1962;15:757.
[73] Harrap BS, Woods EF. Soluble derivatives of feather keratin. 2. Molecular weight and conformation. Biochem J 1964;92(1):19–26.
[74] Gerber PA, Buhren BA, Schrumpf H, Homey B, Zlotnik A, Hevezi P. The top skin-associated genes: a comparative analysis of human and mouse skin transcriptomes. Biol Chem 2014;395(6):577–91.
[75] Greenwold MJ, Sawyer RH. Molecular evolution and expression of archosaurian β-keratins: diversification and expansion of archosaurian β-keratins and the origin of feather β-keratins. J Exp Zool Part B: Mol Dev Evol 2013;320(6):393–405.
[76] Padykula H, editor. Control mechanisms in the expression of cellular phenotypes. In: Symposia of the international society for cell biology, vol. 9. New York and London: Academic Press; 1970.
[77] Rogers GE. The structure and biochemistry of keratin. In: Bittar EE, Bittar N, editors. The biological basis of medicine. New York: Academic Press; 1969. p. 21–57.
[78] Marshall RC, Orwin DF, Gillespie JM. Structure and biochemistry of mammalian hard keratin. Electron Microsc Rev 1991;4(1):47–83.
[79] Kemp DJ, Dyer PY, Rogers GE. Keratin synthesis during development of the embryonic chick feather. J Cell Biol 1974;62(1):114–31.
[80] Gregg K, Rogers GE. Feather keratin: composition, structure and biogenesis. In: Bereiter-Hahn J, Matoltsy AG, Richards KS, editors. Biology of the integument. Berlin, Heidelberg: Springer; 1986. p. 666–94.
[81] Tomlinson DJ, Mülling CH, Fakler TM. Invited review: formation of keratins in the bovine claw: roles of hormones, minerals, and vitamins in functional claw integrity. J Dairy Sci 2004;87(4):797–809.
[82] Mülling CKW. Three-dimensional appearance of bovine epidermal keratinocytes in different stages of differentiation revealed by cell maceration and scanning electron microscopic investigation. Folia Morphol (Warsz) 2000;59(4):239–46.
[83] Mülling C, Lischer CJ. New aspects of etiology and pathogenesis of laminitis in cattle. In: Recent advances in bovine medicine. World buriatrics conf; 2002. p. 2–13.
[84] Brody I. The ultrastructure of the tonofibrils in the keratinization process of normal human epidermis. J Ultrastruct Res 1960;4(3–4):264–97.
[85] Roth S, Clark WH. Ultrastructural evidence related to the mechanism of keratin synthesis. In: Montagna W, Lobitz WC, editors. The epidermis. New York: Academic Press Inc.; 1964. p. 303.
[86] Matoltsy AG, Huszar T. Keratinization of the reptilian epidermis: an ultrastructural study of the turtle skin. J Ultrastruct Res 1972;38(1):87–101.
[87] Matoltsy AG. Keratinization of the avian epidermis: an ultrastructural study of the newborn chick skin. J Ultrastruct Res 1969;29(5–6):438–58.
[88] Maderson PFA, Hillenius WJ, Hiller U, Dove CC. Towards a comprehensive model of feather regeneration. J Morphol 2009;270(10):1166–208.
[89] Alibardi L, Toni M. Cytochemical and molecular characteristics of the process of cornification during feather morphogenesis. Prog Histochem Cytochem 2008;43(1):1–69.
[90] Alibardi L. Ultrastructure of the feather follicle in relation to the formation of the rachis in pennaceous feathers. Anat Sci Int 2010;85(2):79–91.
[91] Filshie BK, Gogers GE. An electron microscope study of the fine structure of feather keratin. J Cell Biol 1962;13(1):1–12.
[92] Baden HP, Maderson PF. Morphological and biophysical identification of fibrous proteins in the amniote epidermis. J Exp Zool 1970;174(2):225–32.
[93] Alibardi L. Immunolocalization of alpha-keratins and feather beta-proteins in feather cells and comparison with the general process of cornification in the skin of mammals. Ann Anat 2013;195(2):189–98.
[94] Matulionis DH. Morphology of the developing down feathers of chick embryos. A descriptive study at the ultrastructural level of differentiation and keratinization. Z Anat Entw Gesch 1970;132(2):107–57.

[95] Alibardi L. Keratinization and lipogenesis in epidermal derivatives of the zebrafinch, *Taeniopygia guttata castanotis* (Aves, Passeriformes, ploecidae) during embryonic development. J Morphol 2002;251(3):294–308.
[96] Schmid E, Tapscott S, Bennett GS, Croop J, Fellini Sa, Holtzer H, et al. Differential location of different types of intermediate-sized filaments in various tissues of the chicken embryo. Differentiation 1979;15(1):27–40.
[97] Meyer W, Baumgärtner G. Embryonal feather growth in the chicken. J Anat 1998;193(Pt 4):611–6.
[98] Alibardi L, Thompson MB. Epidermal differentiation during carapace and plastron formation in the embryonic turtle *Emydura macquarii*. J Anat 1999;194(Pt 4):531–45.
[99] Alibardi L. Immunocytochemical observations on the cornification of soft and hard epidermis in the turtle *Chrysemys picta*. Zoology (Jena) 2002;105(1):31–44.
[100] Fraser RDB, Parry DAD. The molecular structure of reptilian keratin. Int J Biol Macromol 1996;19(3):207–11.
[101] Bendit EG. The α-β transformation in keratin. Nature 1957;179:535.
[102] Cao J. Is the α-β transition of keratin a transition of α-helices to β-pleated sheets. II. Synchrotron investigation for stretched single specimens. J Mol Struct 2002;607(1):69–75.
[103] Kreplak L, Doucet J, Dumas P, Briki F. New aspects of the α-helix to β-sheet transition in stretched hard α-keratin fibers. Biophys J 2004;87(1):640–7.
[104] Pautard FGE. Mineralization of keratin and its comparison with the enamel matrix. Nature 1963;199:9531–5.
[105] Feughelman M. A two-phase structure for keratin fibers. Text Res J 1959;29(3):223–8.
[106] Feughelman M. A model for the mechanical properties of the α-keratin cortex. Text Res J 1994;64(4):236–9.
[107] Wortmann F-J, Zahn H. The stress/strain curve of α-keratin fibers and the structure of the intermediate filament. Text Res J 1994;64(12):737–43.
[108] Chapman BM. A review of mechanical properties of keratin fibres. J Text Inst 1969;60(5):181–207.
[109] Hearle JWS. A critical review of the structural mechanics of wool and hair fibres. Int J Biol Macromol 2000;27(2):123–38.
[110] Chapman BM. A mechanical model for wool and other keratin fibers. Text Res J 1969;39(12):1102–9.
[111] Fraser RDB, MacRae TP. Molecular structure and mechanical properties of keratins. In: Vincent JFV, Currey JD, editors. The mechanical properties of biological materials (proceedings of the symposia of the society for experimental biology). Cambridge, UK: Cambridge University Press; 1980. p. 211–46.
[112] Fudge DS, Gardner KH, Forsyth VT, Riekel C, Gosline JM. The mechanical properties of hydrated intermediate filaments: insights from hagfish slime threads. Biophys J 2003;85(3):2015–27.
[113] Kreplak L, Doucet J, Briki F. Unraveling double stranded α-helical coiled coils: an X-ray diffraction study on hard α-keratin fibers. Biopolymers 2001;58(5):526–33.
[114] Kasapi MA, Gosline JM. Micromechanics of the equine hoof wall: optimizing crack control and material stiffness through modulation of the properties of keratin. J Exp Biol 1999;202(Pt 4):377–91.
[115] Fudge DS, Gosline JM. Molecular design of the alpha-keratin composite: insights from a matrix-free model, hagfish slime threads. Proc Biol Sci 2004;271(1536):291–9.
[116] Miserez A, Wasko SS, Carpenter CF, Waite JH. Non-entropic and reversible long-range deformation of an encapsulating bioelastomer. Nat Mater 2009;8(11):910–6.
[117] Kasapi MA, Gosline JM. Strain-rate-dependent mechanical properties of the equine hoof wall. J Exp Biol 1996;199(Pt 5):1133–46.
[118] Gubernatis JE, Domany E, Krumhansl JA, Huberman M. The Born approximation in the theory of the scattering of elastic waves by flaws. J Appl Phys 1977;48(7):2812–9.
[119] Kjartansson E. Constant Q-wave propagation and attenuation. J Geophys Res 1979;84(B9):4737.
[120] Bonser RHC, Purslow PP. The Young's modulus of feather keratin. J Exp Biol 1995;1033(4):1029–33.
[121] Szabo TL, Wu J. A model for longitudinal and shear wave propagation in viscoelastic media. J Acoust Soc Am 2000;107(5):2437.
[122] Feughelman M, Robinson MS. The relationship between some mechanical properties of single wool fibers and relative humidity. Text Res J 1967;37(6):441–6.
[123] Bertram JE, Gosline JM. Functional design of horse hoof keratin: the modulation of mechanical properties through hydration effects. J Exp Biol 1987;130:121–36.
[124] Winegard TM, Fudge DS. Deployment of hagfish slime thread skeins requires the transmission of mixing forces via mucin strands. J Exp Biol 2010;213(Pt 8):1235–40.
[125] Kitchener A, Vincent JFV. Composite theory and the effect of water on the stiffness of horn keratin. J Mater Sci 1987;22(4):1385–9.
[126] Li SZ. Ben Cao Gang Mu. Changchun, China: The Time Literature & Art Press; 2005.
[127] Rouse JG, Van Dyke ME. A review of keratin-based biomaterials for biomedical applications. Materials (Basel) 2010;3(2):999–1014.
[128] Hofmeier J. Horn-lime plastic masses from keratin substances. Ger pat no 184915; 1905.
[129] Dale HN. Keratin and other coatings for pills. Pharmacol J 1932;129:494–5.
[130] Beyer C. The keratin or horny substance of the hair. Ger pat no 22643; 1907.
[131] Fraser RDB, MacRae TP. Schematic diagram of the wool fibre. Commonwealth Scientific and Industrial Research Organisation. <http://www.csiropedia.csiro.au/display/CSIROpedia/Wool+fibre+structure>.
[132] Rivett D, Ward C, Belkin L, Ramshaw J, Wilshire J. Keratin and wool research. In: The Lennox legacy: the history of the CSIRO Laboratory at 343 Royal Parade Parkville. Collingwood, VIC, Australia: CSIRO Publishing; 1996.
[133] Gillespie JM, Frenkel MJ. The diversity of keratins. Comp Biochem Physiol Part B: Comp Biochem 1974;47(2):339–46.
[134] Kawano Y, Okamoto S. Film and gels of keratin. Kagaku to Seibutsu 1975;13(5):291–2.
[135] van de Locht M. Reconstitution of microfibrils from wool and filaments from epidermis proteins. Melliand Textilberichte 1987;10:780–6.
[136] Ito H, Miyamoto T, Inagaki H, Noishiki Y. Biocompatibility of denatured keratins from wool. Kobunshi Ronbunshu 1982;39(4):249–56.
[137] Schwinger G, Zanger K, Greven H. Structural and mechanical aspects of the skin of *Bufo marinus* (Anura, Amphibia). Tissue Cell 2001;33(5):541–7.

[138] Vincent JFV, Owers P. Mechanical design of hedgehog spines and porcupine quills. J Zool 1986;210(1):55–75.
[139] Yang W, McKittrick J. Separating the influence of the cortex and foam on the mechanical properties of porcupine quills. Acta Biomater 2013;9(11):9065–74.
[140] Farren L, Shayler S, Ennos AR. The fracture properties and mechanical design of human fingernails. J Exp Biol 2004;207(5):735–41.
[141] Kitchener A. Fracture toughness of horns and a reinterpretation of the horning behaviour of bovids. J Zool 1987;213(4):621–39.
[142] Kitchener A. Effect of water on the linear viscoelasticity of horn sheath keratin. J Mater Sci Lett 1987;6(3):321–2.
[143] Bonser RHC. The mechanical performance of meduallary foam from feathers. J Mater Sci Lett 2001;20:941–2. no. c.
[144] Bodde SG, Meyers MA, McKittrick J. Correlation of the mechanical and structural properties of cortical rachis keratin of rectrices of the Toco toucan (*Ramphastos toco*). J Mech Behav Biomed Mater 2011;4(5):723–32.
[145] McKittrick J, Chen PY, Tombolato L, Novitskaya EE, Trim MW, Hirata Ga, et al. Energy absorbent natural materials and bioinspired design strategies: a review. Mater Sci Eng C 2010;30(3):331–42.
[146] Rogers GE. Electron microscope studies of hair and wool. Ann N Y Acad Sci 1959;83(3):378–99.
[147] Rogers GE. Electron microscopy of wool. J Ultrastruct Res 1959;2(3):309–30.
[148] Morton WE, Hearle JW. Physical properties of textile fibres. 3rd ed. Manchester, UK: The Textile Institute; 1993.
[149] Wu KS, Van Osdol WW, Dauskardt RH. Mechanical properties of human stratum corneum: effects of temperature, hydration, and chemical treatment. Biomaterials 2006;27(5):785–95.
[150] Chou SF, Overfelt RA. Tensile deformation and failure of North American porcupine quills. Mater Sci Eng C 2011;31(8):1729–36.
[151] Trim MW, Horstemeyer MF, Rhee H, El Kadiri H, Williams LN, Liao J, et al. The effects of water and microstructure on the mechanical properties of bighorn sheep (*Ovis canadensis*) horn keratin. Acta Biomater 2011;7(3):1228–40.
[152] Taylor AM, Bonser RHC, Farrent JW. The influence of hydration on the tensile and compressive properties of avian keratinous tissues. J Mater Sci 2004;39(3):939–42.
[153] Seki Y, Schneider MS, Meyers MA. Structure and mechanical behavior of a toucan beak. Acta Mater 2005;53(20):5281–96.
[154] Klein MCG, Deuschle JK, Gorb SN. Material properties of the skin of the Kenyan sand boa *Gongylophis colubrinus* (Squamata, Boidae). J Comp Physiol A: Neuroethol Sensory Neural Behav Physiol 2010;196(9):659–68.
[155] Wang B, Yang W, Meyers MA. Unpublished results; 2014.
[156] Coulombe PA, Wong P. Cytoplasmic intermediate filaments revealed as dynamic and multipurpose scaffolds. Nat Cell Biol 2004;6(8):699–706.
[157] Scanning electron micrograph of stratum corneum. <http://feleciaroselabs.com/wp-content/uploads/2012/05/SC.jpg>.
[158] Plewig G, Marples RR. Regional differences of cell sizes in the human stratum corneum. Part I. J Invest Dermatol 1970;54(1):13–8.
[159] Ovaere P, Lippens S, Vandenabeele P, Declercq W. The emerging roles of serine protease cascades in the epidermis. Trends Biochem Sci 2009;34(9):453–63.
[160] Papir YS, Hsu KH, Wildnauer RH. The mechanical properties of stratum corneum: I. The effect of water and ambient temperature on the tensile properties of newborn rat stratum corneum. Biochim Biophys Acta 1975;399:170–80.
[161] Yuan Y, Verma R. Measuring microelastic properties of stratum corneum. Colloids Surf B: Biointerfaces 2006;48(1):6–12.
[162] Wu KS, Stefik MM, Ananthapadmanabhan KP, Dauskardt RH. Graded delamination behavior of human stratum corneum. Biomaterials 2006;27(34):5861–70.
[163] Biniek K, Levi K, Dauskardt RH. Solar UV radiation reduces the barrier function of human skin. Proc Natl Acad Sci 2012;109(42):17111–6.
[164] Feughelman M, Haly aR. The mechanical properties of wool keratin and its molecular configuration. Kolloid-Zeitschrift 1960;168(2):107–15.
[165] Fan J, Yu WD. Fractal analysis of the ortho-cortex and para-cortex of wool fiber. Adv Mater Res 2011;197–198:86–9.
[166] Rogers GE, Filshie BK. Some aspects of the ultrastructure of a-keratin, bacterial flagella, and feather keratin. In: Borasky R, editor. Ultrastructure of protein fibres. New York: Academic Press Inc.; 1963. p. 123–38.
[167] Dobb MG. Electron-diffraction studies of keratin cells. J Text Inst 1970;61(5):232–4.
[168] Crewter WG. The effects of disaggregating agents on the stress–strain relationship for wool fibers. Text Res J 1972;42(2):77–85.
[169] Hearle JWS. The structural mechanics of fibers. J Polym Sci Part C: Polym Symp 1967;20(1):215–51.
[170] Feughelman M. Keratin. Encyclopaedia of polymer science and engineering, 2nd ed., vol. 8. New York: John Wiley and Son Inc.; 1987. p. 566–600.
[171] Bendit EG. A quantitative X-ray diffraction study of the alpha-beta transformation in wool keratin. Text Res J 1960;30(8):547–55.
[172] Treloar LRG. The physics of rubber elasticity. Oxford: Clarendon Press; 1975.
[173] Harrington MJ, Wasko SS, Masic A, Fischer FD, Gupta HS, Fratzl P. Pseudoelastic behaviour of a natural material is achieved via reversible changes in protein backbone conformation. J R Soc Interface 2012;9(76):2911–22.
[174] Woods JL, Harland DP, Vernon JA, Krsinic GL, Walls RJ. Morphology and ultrastructure of antler velvet hair and body hair from red deer (*Cervus elaphus*). J Morphol 2011;272(1):34–49.
[175] Yu Y, Wang B, Meyers MA. Unpublished results; 2015.
[176] Karam GN, Gibson LJ. Biomimicking of animal quills and plant stems: natural cylindrical shells with foam cores. Mater Sci Eng C 1994;2(1–2):113–32.
[177] Karam GN, Gibson LJ. Elastic buckling of cylindrical shells with elastic cores—I. Analysis. Int J Solids Struct 1995;32(8–9):1259–83.
[178] Karam GN, Gibson LJ. Elastic buckling of cylindrical shells with elastic cores—II. Experiments. Int J Solids Struct 1995;32(8–9):1285–306.
[179] Yang W, Chao C, McKittrick J. Axial compression of a hollow cylinder filled with foam: a study of porcupine quills. Acta Biomater 2013;9(2):5297–304.

[180] Busson B, Engström P, Doucet J. Existence of various structural zones in keratinous tissues revealed by X-ray microdiffraction. J Synchrotron Radiat 1999;6(5):1021–30.
[181] Chou SF, Overfelt RA, Miller ME. Anisotropic mechanical behavior of keratin tissue from quill shells of North American porcupine (*Erethizon dorsatum*). Mater Sci Eng A 2012;557:36–44.
[182] Timoshenko S. Theory of elastic stability. New York: McGraw-Hill; 1936.
[183] Gibson LJ, Ashby MF. Cellular solids: structures and properties. New York, Oxford: Pergamon Press; 1988.
[184] Geist V. The evolution of horn-like organs. Behavior 1955;27(1):175–214.
[185] Tombolato L, Novitskaya EE, Chen PY, Sheppard FA, McKittrick J. Microstructure, elastic properties and deformation mechanisms of horn keratin. Acta Biomater 2010;6(2):319–30.
[186] Kitchener AC. Fighting and the mechanical design of horns and antlers. In: Domenici P, Blake RW, editors. Biomechanics in animal behaviour. Oxford: BIOS Scientific Publishers; 2000.
[187] Currey JD. Mechanical properties of bone tissues with greatly differing functions. J Biomech 1979;12(4):313–9.
[188] Gordon JE. Structures or why things don't fall down. London: Penguin Books; 1978.
[189] Li BW, Zhao HP, Feng XQ, Guo WW, Shan SC. Experimental study on the mechanical properties of the horn sheaths from cattle. J Exp Biol 2010;213(3):479–86.
[190] Warburton FL. Determination of the elastic properties of horn keratin. J Text Inst Proc 1948;39(7):297–308.
[191] Kelly A. Strong solids. Oxford: Clarendon Press; 1973.
[192] Feughelman M, Robinson MS. Some mechanical properties of wool fibers in the 'hookean' region from zero to 100% relative humidity. Text Res J 1971;41(6):469–74.
[193] Kasapi MA, Gosline JM. Design complexity and fracture control in the equine hoof wall. J Exp Biol 1997;200(Pt 11):1639–59.
[194] Nickel R. Über den Bau der Hufröhrchen und seine Bedeutung für den Mechanismus des Pferdehufes. Morph Jb 1938;82:119–60.
[195] Ryder ML. Structure of rhinoceros horn. Nature 1962;193:1199–201.
[196] Bertram JE, Gosline JM. Fracture toughness design in horse hoof keratin. J Exp Biol 1986;125:29–47.
[197] Cook J, Gordon JE, Evans CC, Marsh DM. A mechanism for the control of crack propagation in all-brittle systems. Proc R Soc Lond A: Math Phys Eng Sci 1964;282(1391):508–20.
[198] Wright TM, Hayes WC. Fracture mechanics parameters for compact bone-effects of density and specimen thickness. J Biomech 1977;10(7):419–30.
[199] Leach DH. The structure and function of equine hoof wall. University of Saskatchewan; 1980.
[200] Hamrick MW. Functional and adaptive significance of primate pads and claws: evidence from New World anthropoids. Am J Phys Anthropol 1998;106(2):113–27.
[201] Caputo R, Gasparini G, Contini D. A freeze-fracture study of the human nail plate. Arch Dermatol Res 1982;272:117–25.
[202] Garson JC, Baltenneck F, Leroy F, Riekel C, Müller M. Histological structure of human nail as studied by synchrotron X-ray microdiffraction. Cell Mol Biol 2000;46(6):1025–34.
[203] Achten G. Histopathology of the nail. In: Pierre M, editor. The nail. Edinburgh: Churchill Livingstone; 1981. p. 1–14.
[204] Baden HP. The physical properties of nail. J Invest Dermatol 1970;55(2):115–22.
[205] Farran L, Ennos AR, Eichhorn SJ. The effect of humidity on the fracture properties of human fingernails. J Exp Biol 2008;211(Pt 23):3677–81.
[206] Lewis BL. Microscopic studies of fetal and mature nail and surrounding soft tissue. AMA Arch Derm Syphilol 1954;70:733–47.
[207] Ramrakhiani M. Indentation and hardness studies of human nails. Indian J Biochem Biophys 1978;15(4):341–3.
[208] Farran L, Ennos AR, Starkie M, Eichhorn SJ. Tensile and shear properties of fingernails as a function of a changing humidity environment. J Biomech 2009;42(9):1230–5.
[209] Whale baleen picture. <http://en.wikipedia.org/wiki/File:Baleen.jpg>.
[210] Pautard F. Calcification of baleen. In: Calcified tissues. Proc second Europ symp; 1965. p. 347–57.
[211] Fudge DS, Szewciw LJ, Schwalb AN. Morphology and development of blue whale baleen: an annotated translation of Tycho Tullberg's classic 1883 paper. Aquat Mamm 2009;35(2):226–52.
[212] Bardack D. First fossil lamprey: a record from the Pennsylvanian of Illinois. Science 1968;162(3859):1265–7.
[213] Hagfish. <http://www.ryanphotographic.com/myxinidae.htm>.
[214] Zintzen V, Roberts CD, Anderson MJ, Stewart AL, Struthers CD, Harvey ES. Hagfish predatory behaviour and slime defence mechanism. Sci Rep 2011;1:1–6.
[215] Hagfish slime and the threads. <http://bouncingideas.wordpress.com/2011/10/29/hagfish-slime-is-the-new-spiderweb-silk/>.
[216] Fudge DS, Levy N, Chiu S, Gosline JM. Composition, morphology and mechanics of hagfish slime. J Exp Biol 2005;208(Pt 24):4613–25.
[217] Koch EA, Spitzer RH, Pithawalla RB, Castillos FA, Parry DAD. Hagfish biopolymer: a type I/type II homologue of epidermal keratin intermediate filaments. Int J Biol Macromol 1995;17(5):283–92.
[218] Baden HP, Goldsmith LA, Lee L. The importance of understanding the comparative properties of hair and other keratinized tissues in studying disorders of hair. In: Brown AC, editor. The first human hair symposium. New York: Medcom Press; 1974. p. 388–98.
[219] Wasko SS, Tay GZ, Schwaighofer A, Nowak C, Waite JH, Miserez A. Structural proteins from whelk egg capsule with long range elasticity associated with a solid-state phase transition. Biomacromolecules 2014;15(1):30–42.
[220] Rawlings TA. Adaptations to physical stresses in the intertidal zone: the egg capsules of neogastropod molluscs. Am Zool 1999;39(2):230–43.
[221] Denny MW. Biology and the mechanics of the wave-swept environment. Princeton, NJ: Princeton University Press; 1988.
[222] Flower NE, Geddes AJ, Rudall KM. Ultrastructure of the fibrous protein from the egg capsules of the whelk *Buccinum undatum*. J Ultrastruct Res 1969;26(3):262–73.
[223] Gathercole LJ. Studies on the protein of the egg capsule of whelks. UK: University of Leeds; 1969.

[224] Whiteley KJ, Kaplin IJ. The comparative arrangement of microfibrils in orth-, meso-, and paracortical cells of merinowool fibres. J Text Inst 1977;68(11):384–6.
[225] Guerette PA, Tay GZ, Hoon S, Loke JJ, Hermawan AF, Schmitt CNZ, et al. Integrative and comparative analysis of coiled-coil based marine snail egg cases – a model for biomimetic elastomers. Biomater Sci 2014;2(5):710.
[226] Rapoport HS, Shadwick RE. Mechanical characterization of an unusual elastic biomaterial from the egg capsules of marine snails (*Busycon* spp.). Biomacromolecules 2002;3(1):42–50.
[227] Wasko SS. Biochemistry and structure–function relationships in the proteinaceous egg capsules of *Busycotypus canaliculatus*. US: UC Santa Barbara; 2010.
[228] Gregg K, Wilton SD, Parry DAD, Rogers GE. A comparison of genomic coding sequences for feather and scale keratins: structural and evolutionary implications. EMBO J 1984;3(1):175–8.
[229] Astbury WT, Marwick TC. X-ray interpretation of the molecular structure of feather keratin. Nature 1932;130(3278):309–10.
[230] Rudall KM. X-ray studies of the distribution of protein chain types in the vertebrate epidermis. Biochim Biophys Acta 1947;1:549–62.
[231] Leonardo da V. Codex on the flight of birds, held Bibl. R. Turin, Italy, 1505.
[232] Wang KY. The swallows make nests by clay: birds and their breeding. Changchun, China: Changchun Press; 1998.
[233] Bachmann T, Emmerlich J, Baumgartner W, Schneider JM, Wagner H. Flexural stiffness of feather shafts: geometry rules over material properties. J Exp Biol 2012;215(3):405–15.
[234] Ennos A, Hickson JRE, Roberts A. Functional morphology of the vanes of the flight feathers of the pigeon *Columba livia*. J Exp Biol 1995;198(Pt 5):1219–28.
[235] Lucas A, Stettenheim P. Avian anatomy-integument. Washington, DC: US Department of Agriculture; 1972.
[236] Purslow PP, Vincent JFV. Mechanical properties of primary feathers from the pigeon. J Exp Biol 1978;72:251–60.
[237] Gill FB. Ornithology. 2nd ed. New York: W.H. Freeman and Company; 1994.
[238] Crenshaw DG. Design and materials of feather shafts: very light, rigid structures. J Biomech 1980;13(2):199.
[239] Lingham-Soliar T, Bonser RHC, Wesley-Smith J. Selective biodegradation of keratin matrix in feather rachis reveals classic bioengineering. Proc Biol Sci 2010;277(1685):1161–8.
[240] Lingham-Soliar T, Murugan N. A new helical crossed-fibre structure of β-keratin in flight feathers and its biomechanical implications. PLoS ONE 2013;8(6).
[241] Corning W, Biewener A. In vivo strains in pigeon flight feather shafts: implications for structural design. J Exp Biol 1998;201(Pt 22):3057–65.
[242] Usherwood JR, Hedrick TL, McGowan CP, Biewener AA. Dynamic pressure maps for wings and tails of pigeons in slow, flapping flight, and their energetic implications. J Exp Biol 2005;208(Pt 2):355–69.
[243] Hertel H. Structure, form, movement. New York: Reinhold Publishing Corp; 1966.
[244] Macleod GD. Mechanical properties of contour feathers. J Exp Biol 1980;87:65–71.
[245] Brush AH, Wyld JA. Molecular organization of avian epidermal structures. Comp Biochem Physiol B 1982;73(2):313–25.
[246] Earland C, Blakey PR, Stell JGP. Molecular orientation of some keratins. Nature 1962;196:1287–91.
[247] Earland C, Blakey PR, Stell JG. Studies on the structure of keratin. IV. The molecular structure of some morphological components of keratins. Biochim Biophys Acta 1962;6:268–74.
[248] Cameron GJ, Wess TJ, Bonser RHC. Young's modulus varies with differential orientation of keratin in feathers. J Struct Biol 2003;143(2):118–23.
[249] Pabisch S, Puchegger S, Kirchner HOK, Weiss IM, Peterlik H. Keratin homogeneity in the tail feathers of *Pavo cristatus* and *Pavo cristatus* mut. alba. J Struct Biol 2010;172(3):270–5.
[250] Liu ZQ, Jiao D, Meyers MA, Zhang ZF. Structure and mechanical properties of naturally occurring lightweight foam-filled cylinder – the peacock's tail coverts shaft and its components. Acta Biomater 2015;17:137–51.
[251] Bonser RH, Farrent JW. Influence of hydration on the mechanical performance of duck down feathers. Br Poult Sci 2001;42(2):271–3.
[252] Clayton DH, Cotgreave P. Relationship of bill to grooming behavior in birds. Anim Behav 1994;47(1):195–201.
[253] Luester AU. Manual of Pirrot behavior. Wiley Blackwell Publishing; 2006.
[254] Rupley AE. Manual de clínica aviária. São Paulo: Português Brasileiro; 1999.
[255] Seki Y, Kad B, Benson D, Meyers Ma. The toucan beak: structure and mechanical response. Mater Sci Eng C 2006;26(8):1412–20.
[256] Seki Y, Bodde SG, Meyers Ma. Toucan and hornbill beaks: a comparative study. Acta Biomater 2010;6(2):331–43.
[257] Lin A, Meyers MA. Growth and structure in abalone shell. Mater Sci Eng A 2005;390(1–2):27–41.
[258] Chapman RE. Hair, wool, quill, nail, claw, hoof and horn. In: Bereither-Hahn J, Matoltsy GA, Sylvia-Richards K, editors. Biology of the integument, vertebrates, vol. 2. Berlin/Heidelberg/New York: Springer-Verlag; 1986. p. 293–312.
[259] Clark WE. The problem of the claw in primates. Proc Zool Soc Lond 1936;106(1):1–24.
[260] Thorndike EE. A microscopic study of the marmoset claw and nail. Am J Phys Anthropol 1968;28(3):247–61.
[261] Alexander RM, Maloiy GMO, Njau R, Jayes AS. Mechanics of running of the ostrich (*Struthio camelus*). J Zool 2009;187(2):169–78.
[262] Bonser RHC. Hydration sensitivity of ostrich claw keratin. J Mater Sci Lett 2002;21:1563–4.
[263] Bonser RHC. The Young's modulus of ostrich claw keratin. J Mater Sci Lett 2000;19:1039–40.
[264] Leach DH, Zoerb GC. Mechanical properties of equine hoof wall tissue. Am J Vet Res 1983;44(11):2190–4.
[265] Douglas JE, Mittal C, Thomason JJ, Jofriet JC. The modulus of elasticity of equine hoof wall: implications for the mechanical function of the hoof. J Exp Biol 1996;199(Pt 8):1829–36.
[266] Wyld JA, Brush AH. Keratin diversity in the reptilian epidermis. J Exp Zool 1983;225(3):387–96.
[267] Wyld JA, Brush AH. The molecular heterogeneity and diversity of reptilian keratins. J Mol Evol 1979;12(4):331–47.
[268] Maderson PFA. Some developmental problems of the reptilian integument. In: Gans C, Billett F, Maderson PFA, editors. Biology of the reptilia. John Wiley & Sons; 1985. p. 523–98.
[269] Landmann L. The skin of reptiles: epidermis and dermis. In: Bereither-Hahn J, Matoltsy GA, Sylvia-Richards K, editors. Biology of the integument, vertebrates, vol. 2. Berlin/Heidelberg/New York: Springer-Verlag; 1986. p. 150–87.

[270] Sawyer RH, Glenn T, French JO, Mays B, Shames RB, Barnes Jr GL, et al. The expression of beta (β) keratins in the epidermal appendages of reptiles and birds. Am Zool 2000;40(4):530–9.
[271] Alibardi L, Sawyer RH. Immunocytochemical analysis of beta (β) keratins in the epidermis of chelonians, lepidosaurians, and archosaurians. J Exp Zool 2002;293(1):27–38.
[272] Filshie BK, Rogers GE. The fine structure of α-keratin. J Mol Biol 1961;3(6):784–6.
[273] Alexander NJ. Comparison of α and β keratin in reptiles. Z Zellforsch 1970;110(2):153–65.
[274] Alibardi L, Toni M. Cytochemical, biochemical and molecular aspects of the process of keratinization in the epidermis of reptilian scales. Prog Histochem Cytochem 2006;40(2):73–134.
[275] Alexander NJ, Parakkal PF. Formation of α- and β-type keratin in lizard epidermis during the molting cycle. Z Zellforsch 1969;101(1):72–87.
[276] Toni M, Alibardi L. Alpha- and beta-keratins of the snake epidermis. Zoology 2007;110(1):41–7.
[277] Spearman RIC. The epidermis of the gopher tortoise *Testudo polyphemus* (Daudin). Acta Zool 1969;50:1–9.
[278] Bauer AM, Russell AP, Shadwick RE. Mechanical properties and morphological correlates of fragile skin in gekkonid lizards. J Exp Biol 1989;145:79–102.
[279] Klein M-CG, Gorb SN. Epidermis architecture and material properties of the skin of four snake species. J R Soc Interface 2012;9(76):3140–55.
[280] Landmann L. Keratin formation and barrier mechanisms in the epidermis of *Natrix natrix* (Reptilia: Serpentes): an ultrastructural study. J Morphol 1979;162(1):93–126.
[281] Wang RZ, Weiner S. Strain–structure relations in human teeth using Moiré fringes. J Biomech 1998;31(2):135–41.
[282] Fong H, Sarikaya M, White SN, Snead ML. Nano-mechanical properties profiles across dentin–enamel junction of human incisor teeth. Mater Sci Eng C 2000;7(2):119–28.
[283] Zangerl R. The turtle shell. In: Gans C, editor. Biology of the reptilia: morphology A, vol. 1. London, New York: Academic Press; 1969. p. 311–39.
[284] Cherepanov GO. Ontogenetic development of the shell in *Trionix sinensis* (Trionichidae, Testudinata) and some questions on the nomenclature of bony plates. Russ J Herpetol 1995;2(2):129–33.
[285] Gilbert SF, Loredo GA, Brukman A, Burke AC. Morphogenesis of the turtle shell: the development of a novel structure in tetrapod evolution. Evol Dev 2001;3(2):47–58.
[286] Dalla Valle L, Michieli F, Benato F, Skobo T, Alibardi L. Molecular characterization of alpha-keratins in comparison to associated beta-proteins in soft-shelled and hard-shelled turtles produced during the process of epidermal differentiation. J Exp Zool Part B: Mol Dev Evol 2013;320:428–41.
[287] Alibardi L. Ultrastructural immunolocalization of alpha-keratins and associated beta-proteins (beta-keratins) suggests a new interpretation on the process of hard and soft cornification in turtle epidermis. Micron 2013;52–53:8–15.
[288] Achrai B, Bar-On B, Wagner HD. Bending mechanics of the red-eared slider turtle carapace. J Mech Behav Biomed Mater 2014;30:223–33.
[289] Rhee H, Horstemeyer MF, Hwang Y, Lim H, El Kadiri H, Trim W. A study on the structure and mechanical behavior of the *Terrapene carolina* carapace: a pathway to design bio-inspired synthetic composites. Mater Sci Eng C 2009;29(8):2333–9.
[290] Balani K, Patel RR, Keshri AK, Lahiri D, Agarwal A. Multi-scale hierarchy of *Chelydra serpentina*: microstructure and mechanical properties of turtle shell. J Mech Behav Biomed Mater 2011;4(7):1440–51.
[291] Damiens R, Rhee H, Hwang Y, Park SJ, Hammi Y, Lim H, et al. Compressive behavior of a turtle's shell: experiment, modeling, and simulation. J Mech Behav Biomed Mater 2012;6:106–12.
[292] Achrai B, Wagner HD. Micro-structure and mechanical properties of the turtle carapace as a biological composite shield. Acta Biomater 2013;9(4):5890–902.
[293] Zhang W, Wu C, Zhang C, Chen Z. Numerical study of the mechanical response of turtle shell. J Bionic Eng 2012;9(3):330–5.
[294] Zhang W, Wu C, Zhang C, Chen Z. Microstructure and mechanical property of turtle shell. Theor Appl Mech Lett 2012;2(1):014009.
[295] Spearman RIC. The keratinization of epidermal scales, feathers and hairs. Biol Rev 1966;41(1):59–96.
[296] Briggs M, Briggs P. The Encyclopedia of world wildlife. Paragon Books; 2006.
[297] Pangolin, aomor function. <http://www.animal-space.net/2010/12/lion-vs-pangolin.html>.
[298] Pangolin armor coat. <http://commons.wikimedia.org/wiki/File:Coat_of_Pangolin_scales.JPG?uselang=zh-cn>.
[299] African tree pangolin. <http://commons.wikimedia.org/wiki/File:Manis_tricuspis_San_Diego_Zoo_03.2012.jpg>.
[300] Chinese ground pangolin. <http://commons.wikimedia.org/wiki/File:Zoo_Leipzig_-_Tou_Feng.jpg>.
[301] Tong J, Ren L-Q, Chen B-C. Chemical constitution and abrasive wear behaviour of pangolin scales. J Mater Sci Lett 1995;14(20):1468–70.
[302] Heath ME. Manis pentadactyla. Am Soc Mammal 1992;414:1–6.
[303] Tong J, Ma YH, Ren LQ, Li JQ. Tribological characteristics of pangolin scales in dry sliding. J Mater Sci Lett 2000;19(7):569–72.
[304] Vincent JFV, Bogatyreva OA, Bogatyrev NR, Bowyer A, Pahl A-K. Biomimetics: its practice and theory. J R Soc Interface 2006;3(9):471–82.
[305] Web of Science. Increase of publications and citations for 'bioinspired materials' since 1996. Web of Science; 2015. <http://apps.webofknowledge.com/CitationReport.do?product=UA&search_mode=CitationReport&SID=3Btq3MDi5Rv8JF5oBG8&page=1&cr_pqid=1&viewType=summary>.
[306] Yang W, Chen IH, Gludovatz B, Zimmermann EA, Ritchie RO, Meyers MA. Natural flexible dermal armor. Adv Mater 2013;25(1):31–48.
[307] Banhart J. Aluminum foams: on the road to real applications. MRS Bull 2003;28(4):290–5.
[308] Veedu VP, Cao A, Li X, Ma K, Soldano C, Kar S, et al. Multifunctional composites using reinforced laminae with carbon-nanotube forests. Nat Mater 2006;5(6):457–62.
[309] Drakonakis VM, Velisaris CN, Seferis JC, Doumanidis CC. Feather-inspired carbon fiber reinforced polymers with nanofibrous fractal interlayer. Polym Compos 2014.

[310] Cho WK, Ankrum JA, Guo D, Chester SA, Yang SY, Kashyap A, et al. Microstructured barbs on the North American porcupine quill enable easy tissue penetration and difficult removal. Proc Natl Acad Sci USA 2012;109(52):21289–94.
[311] Industrial wastewater filter technology inspired by nature. Filtrat Sep 2003; 40(1): 18–21.
[312] Whalebone inspires filter technology. Filtrat Sep 2007; 44(2): 10.
[313] Baleen Filters Pty Ltd. Baleen filters. <http://www.baleenfilters.com/>.
[314] Pinnacle Armor. The dragon skin bodyarmor. <https://en.wikipedia.org/wiki/Dragon_Skin#/media/File:PEO_soldier_Dragonskin.jpg>.
[315] Cyclus Manufacture. Pangolin backpack. <http://www.pangolin.com.co/collections/main-collection>.
[316] Banwell EF, Abelardo ES, Adams DJ, Birchall MA, Corrigan A, Donald AM, et al. Rational design and application of responsive alpha-helical peptide hydrogels. Nat Mater 2009;8(7):596–600.
[317] Fu T, Guerette PA, Tan RY, Zhao H, Schefer L, Mezzenga R, et al. Biomimetic self-assembly of recombinant marine snail egg capsule proteins into structural coiled-coil units. J Mater Chem B 2015.